Università degli studi di Padova

Facoltà di Scienze MM.FF.NN.

Dipartimento di Fisica “G. Galilei”

SCUOLA DI DOTTORATO DI RICERCA IN FISICA

CICLO XXV

Wide energy range trigger and development of new electronics for ICARUS LAr-TPC

Coordinatore: Ch.mo Prof. ANDREA VITTURI

Supervisore: Ch.mo Prof. SANDRO CENTRO

Co-Supervisore: Dott. ALBERTO GUGLIELMI

Dottorando: Dott. DANIELE DEQUAL

Abstract

The ICARUS-T600 detector, with its 470 tons of active mass, is the largest Liquid Argon TPC (LAr-TPC) ever built, and is now currently operating in the LNGS underground laboratory, detecting cosmic rays events after 3 years of data taking with the CERN Neutrinos to Gran Sasso beam. Its excellent calorimetric resolution and topology reconstruction capabilities permit a wide physics program, which goes from nucleon decay to the study of the oscillation of the neutrinos from the CNGS beam. The events collected differ both for energy deposition (ranging from tens of MeV to tens of GeV) and for topology. To get a fully-efficient detection of the interesting events it is thus necessary to exploit all available sources in the trigger system: the scintillation light, the charge signal on wires and timing information (for beam-related events).

For the 2010-2013 data taking a primary trigger, based on the signal from the photomultipliers placed inside the detector, has been set up. To enhance the efficiency of this setup for CNGS neutrino events, a particular effort has been addressed to the development of a time synchronization with the spill extraction, which allowed to reduce the trigger threshold in coincidence with the neutrino arrival time. To check the PMT efficiency for the CNGS events, an alternative minimum biasing trigger has been also developed, which is based on the time synchronization as well as on the analysis of the charge deposition on the TPC wires. A full efficiency and a rejection of more than 10^3 have been reached with this trigger.

To further increase the PMT trigger efficiency on non beam related events, an hit finding algorithm has been implemented in a hardware device, and is now taking data in steady condition. First results of this recently installed system, have shown an increase of the overall trigger efficiency on the sub-GeV region, which is of particular interest in view of the study of nucleon decay as well as on the low energy tail of the atmospheric neutrons.

Finally ICARUS solved the anomaly reported by the OPERA collaborations on the superluminar neutrino velocity, by performing a high precision measurement of the neutrino time of flight from CERN to LNGS, resulting in perfectly agreement, within the experimental resolution, with the light velocity.

Sommario

Il rivelatore ICARUS T-600, con una massa attiva complessiva di 470 tonnellate, rappresenta la più grande camera a proiezione temporale ad argon liquido (LAr-TPC) mai costruita, ed è attualmente in presa dati ai LNGS, rilevando raggi cosmici dopo i tre anni dedicati alla misura degli eventi dal fascio di neutrini CNGS. La sua eccellente risoluzione calorimetrica, unita alla possibilità di ricostruzione topologica degli eventi, permette un ampio programma di fisica, che spazia dallo studio del decadimento dei nucleoni all'osservazione delle oscillazioni sul fascio CNGS. Gli eventi raccolti differiscono sia per energia depositata nel rivelatore (la quale varia da decine di MeV a decine di GeV) sia per topologia degli eventi. Per ottenere una piena efficienza sugli eventi di interesse è necessario dunque sfruttare tutte le sorgenti di trigger in un unico sistema: la luce di scintillazione, il segnale di carica raccolto dai fili della TPC e la sincronizzazione temporale (per eventi di fascio).

Per la presa dati 2010-13 è stato sviluppato un trigger primario, basato sul segnale raccolto dai fotomoltiplicatori installati all'interno del rivelatore. Per aumentare l'efficienza di questo sistema per gli eventi CNGS, un particolare sforzo è stato rivolto allo sviluppo di un sistema di sincronizzazione con l'estrazione del fascio, che ha permesso di ridurre le soglie di rivelazione in coincidenza col tempo di arrivo dei neutrini. La conferma dell'efficienza di questo sistema è stata ottenuta da un trigger alternativo, basato sull'analisi della carica depositata sui fili delle TPC. Una piena efficienza e una reiezione dei fondi superiore a 10^3 è stata raggiunta con questo sistema.

Per migliorare ulteriormente l'efficienza del trigger da PMT per eventi non di fascio, un algoritmo di identificazione delle hit è stato implementato in un dispositivo hardware, ed è ora stabilmente in presa dati. I primi risultati di questo sistema installato di recente, hanno dimostrato un aumento di efficienza nella regione sub-GeV, la quale è di particolare interesse in vista degli studi sul decadimento del nucleone, così come sulla coda a bassa energia dello spettro dei neutrini atmosferici.

Infine ICARUS ha risolto l'anomalia riportata dalla collaborazione OPERA riguardo alla velocità superluminare del neutrino, misurano con alta precisione il tempo di volo del neutrino dal CERN ai LNGS, concludendo con un perfetto accordo, entro la risoluzione sperimentale, con la velocità della luce.

Contents

Chapter 1

LAr TPC in the present physics scenario

Almost one century after their introduction in the description of Nature, and more than 50 years from their experimental discovery, neutrinos are still at the center of intense experimental and theoretical searches, since their behavior is still far to be completely understood.

A series of exciting experimental results have been following one another in the last 15 years, which have at first definitively proved the oscillatory behavior of neutrinos, and subsequently have given precise measurement of many oscillation parameters. However, several questions remain open, and a wide research program is foreseen for the next decades to clarify all the remaining details of neutrinos nature.

In this scenario, the development of new detectors, which can counterbalance the neutrino tiny cross section with a large detecting volume, as well as a good background rejection, became a crucial point in the evolution of this field. The Liquid Argon Time Projection Chamber (LAr-TPC) technique, which underwent a long R&D process since their conceiving in 1977 by C. Rubbia [1], represents today one of the most suitable solutions to address the main neutrino searches, and a series of proposals based on this technique have already been submitted by several collaborations [2], [3], [4] .

The successful operation of the ICARUS T600 detector represents a milestone in the development of massive LAr TPC detectors, and must be considered not only for its physics capability, but also as a intermediate step toward the construction of much larger detectors, on the kton scale.

1.1 Historical introduction

Neutrinos have been hypothesized for the first time in 1929 by W. Pauli, in a famous letter addressed to the "radioactive ladies and gentlemen" [5], as a possible solution to the problem of the β decay spectrum. The continuous energy distribution of the electron emitted in the decay of ^{210}Bi was in strong disagreement with the two body decay hypothesized at that time, which predicted a spectrum peaked at the Q-value of the reaction; on the other hand it would be naturally explained in a three body decay, in which a part of the energy is carried by a neutral, light, undetected fermion emitted together with the electron.

Few years later, in 1936, E. Fermi named this particle "neutrino" and included it in his theory of weak interaction, proposing a possible measurement of its mass by a precise study of the end-point of the β decay spectrum, measurement which today gives the low limit value on the mass of electron neutrino of 2.05 eV at 95% of C.L [6].

Due to the extremely small neutrino cross section, their detection had to wait until a powerful source, such as nuclear reactors, was available. The first observation of anti-neutrinos from nuclear power plants was performed in 1956 by F. Reines and C. L. Cowan [7] by detecting the inverse beta decay on 200 liters of water target by means of three scintillator tanks, with a total volume of 4200 liters.

The first "anomaly" arisen from the experimental results on neutrino detection came from the observation of a deficit of the solar electron neutrino flux, firstly performed by the Homestake experiment, which observed almost 1/3 of the event rate expected. This anomaly were confirmed few years later by other radiochemical experiments, such as GALLEX/GNO and SAGE, and by the directional real-time experiment Kamiokande (and later Super Kamiokande). Even if the measurement of the neutrino direction ensures that the events detected were actually solar neutrinos, the fact that only ν_e CC interactions were observed made it impossible to disentangle the neutrino physics from the physics behind the generation of solar models. The experiment which definitively clarified the so called "Solar Neutrino Problem" was SNO, which in 2001 published a result [8] in which the ν_e CC and $\nu_{e,\mu,\tau}$ NC were separately measured by means of different interactions. The observation that the NC interactions (equally sensitive to all neutrino flavors) where in good agreement with the expectation, while for

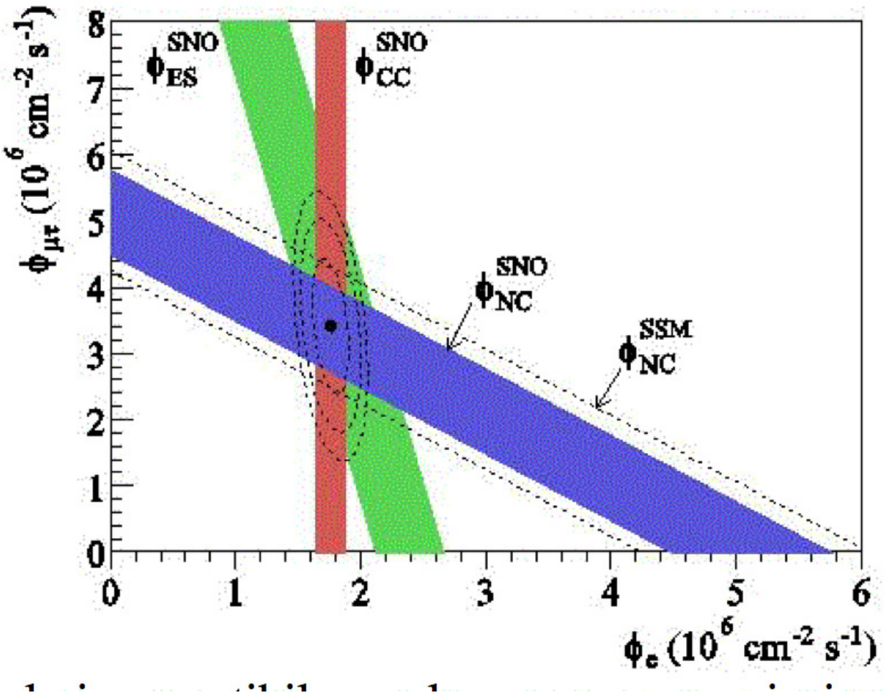

Figure 1.1: SNO results on the measurements solar neutrino flux for the three channels measured. The lines represent the 1σ C.L. for the three measurements, CC, NC and ES

the ν_e CC a deficit of almost 1/3 were observed, finally solve the solar neutrino problem, proving the neutrino flavor oscillation. The Elastic Scattering (ES) on electrons, which happens for all the neutrino flavors, but with a cross which is 6.5 times higher for electron neutrinos, has been also independently measured resulting in a redundant check of the result (fig.1.1).

1.2 Neutrino oscillations

The first idea that neutrino might oscillate from one to another specie was proposed in 1958 by B. Pontecorvo, which hypothesized a possible oscillation between neutrino and antineutrino (at that time only one neutrino family was known). In 1962 Maki, Nakagawa and Sakata drew on this idea, including it in the neutrino three flavor description. According to their explanation, the three neutrino flavors (ν_e, ν_μ, ν_τ) are a quantum superposition of three mass eigenstates (ν_1, ν_2, ν_3), where the decomposition is given by the Pontecorvo-Maki- Nakagawa-Sakata unitary matrix U_{PMNS}:

$$\begin{pmatrix} \nu_e, & \nu_\mu, & \nu_\tau, \end{pmatrix} = U_{PMNS} \begin{pmatrix} \nu_1 \\ \nu_2 \\ \nu_3 \end{pmatrix} \tag{1.1}$$

When neutrinos travel in vacuum, the evolution of their wave function depends on the mass eigenstates decomposition, giving for the evolution of the flavor state at a certain time t:

$$|\nu(t)>= e^{i\mathbf{p}\cdot\mathbf{r}} \sum_{k=1}^{3} U_{\alpha k} e^{-iE_k t} |\nu_k> \tag{1.2}$$

where $E_k = \sqrt{p^2 + m_k^2} \simeq |p| + \frac{m^2}{2|p|} \simeq E + \frac{m^2}{2E}$ and $|\nu(0)>= |\alpha>= \sum_{k=1}^{3} U_{\alpha k} |\nu_k>$.

In case of a difference in the mass values for the three eigenstates, the exponential factor generates a different phase shift proportional to $e^{-it\frac{m_k^2}{2E}}$ in the three components of the sum in 1.2. This turns into a non null probability of observing a flavor state $|\beta>$ generated from the oscillation of an initial state $|\alpha>$ with a probability given by:

$$P_{\nu_\alpha \to \nu_\beta} = | < \nu_\beta | \nu_\alpha > |^2 = \sum_{k,j=1}^{3} U_{\alpha j} U_{\beta j}^* U_{\alpha k}^* U_{\beta k} e^{-it\frac{\Delta m_{jk}^2}{2E}} \tag{1.3}$$

where $\Delta m_{jk}^2 = m_j^2 - m_k^2$.

The same probability can be expressed in a more convenient way in term of the neutrino energy (E) and the distance between the neutrino source and the detector (L) as:

$$P_{\nu_\alpha \to \nu_\beta}(L, E) = -4 \sum_{k>j} Re[W_{\alpha\beta}^{jk}] \sin^2 \frac{\Delta m_{jk}^2 L}{4E} \pm 2 \sum_{k>j} Im[W_{\alpha\beta}^{jk}] \sin^2 \frac{\Delta m_{jk}^2 L}{2E} \tag{1.4}$$

were $W_{\alpha\beta}^{jk} \equiv U_{\alpha j} U_{\beta j}^* U_{\alpha k}^* U_{\beta k}$. In this form the oscillatory behavior clearly emerges from the factor $\sin^2 \frac{\Delta m_{jk}^2 L}{2E}$.

A useful, and quite common, decomposition of the U_{PMNS} matrix is given by the introduction of three mixing angles $(\theta_{12}, \theta_{23}, \theta_{13})$ plus a complex phase δ_{CP} which describes a possible CP violation in the leptonic sector:

$$U_{PMNS} = \begin{pmatrix} 1 & 0 & 0 \\ 0 & c_{23} & s_{23} \\ 0 & -s_{23} & c_{23} \end{pmatrix} \begin{pmatrix} c_{13} & 0 & s_{13}e^{-i\delta} \\ 0 & 1 & 0 \\ -s_{13}e^{-i\delta} & 0 & c_{13} \end{pmatrix} \begin{pmatrix} c_{12} & s_{12} & 0 \\ -s_{12} & c_{12} & 0 \\ 0 & 0 & 0 \end{pmatrix}. \tag{1.5}$$

In this decomposition, where $c_{ij} = \cos(\theta_{ij})$ and $s_{ij} = \sin(\theta_{ij})$, the 3 flavor oscillation is described by three oscillation regimes which involve each only two flavors, i and j, related to the corresponding mass difference Δm^2_{ij}. Since the experimental results on solar and neutrino oscillation have shown that the two Δm^2 differ by a factor ~ 30 it is possible to threat, in good approximation, each oscillation separately. In other words, when an experiment sets the the L/E value, the oscillatory behavior can be expressed as a two flavor i-j mixing where the Δm^2_{ij} is such that $1/\Delta m^2_{ij} = L/E$ giving a simplified oscillation probability:

$$P_{\nu_\alpha \to \nu_\beta} = \sin^2 \theta_{\alpha\beta} \sin^2(\Delta m^2_{ij} \frac{L}{4E}) \tag{1.6}$$

The phenomenon of the neutrino oscillation gives rise to effects which are in contrast with the Standard Model (SM) of electro-weak interactions, i.e. the violation of the leptonic flavor number, and the presence of a no null mass for at least two of the three neutrinos. In this sense neutrino oscillations are one of the most compelling observation of a new physics beyond the SM.

1.3 Present status of the research

The experiments studying the oscillatory behavior of neutrinos can be divided on the basis of the L/E parameter and on the basis of the neutrino (or antineutrino) source studied. The former division brings to the definition of the so called “atmospheric sector”, which studies a $\Delta m^2_{atm} \sim 2.5 \times 10^{-3} eV^2$, and of the “solar sector”, which instead focuses on a smaller value of $\Delta m^2_{sol} \sim 7.5 \times 10^{-5} eV^2$.

For the atmospheric sector, the main information comes from the study of the neutrinos emitted in the interaction of cosmic rays with the atmosphere as a function of the incident direction, which reflects the neutrino baseline. The latest results on these studies comes from Super-Kamiokande, which has set $1.9(1.7) \times 10^{-3} < \Delta m^2_{atm} < 2.6(2.7) \times 10^{-3} eV^2$ and $0.407 \leq \sin^2 \theta_{23} \leq 0.583$ at 90% of C.L[9].

A second source of neutrino which can be use to determine Δm^2_{atm} with high precision is given by muon neutrino fluxes produced at particle accelerators. These experiments study the ν_μ ($\overline{\nu}_\mu$) disappearance from a primary neutrino beam in which the contamination from other flavors is kept under control. One of the latest results on the oscillation parameters has been the measurement performed by the MINOS collabo-

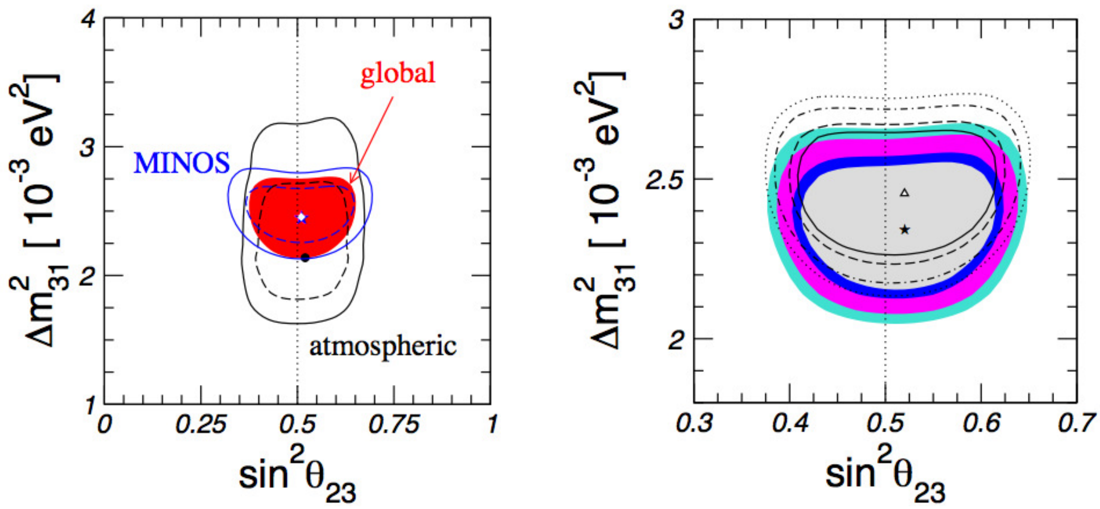

Figure 1.2: Left: 2 and 3 σ contours resulting from the atmospheric (black) and MINOS (red) results. Right: combined fit for normal (black) and inverted (colored) hierarchy at 90%, 95%, 99% and 99.73% of C.L.

ration, studying the behavior of the NuMI beam-line from Fermilab. The L/E range is $\sim$ 500 km/Gev, which is well suited for the atmospheric sector. The experiment is composed by two similar magnetized tracking calorimeters, placed at a distance of 1 km and 735 km from the neutrino source. The choice of a dual detector helps reducing the systematics, in particular those related to the beam composition and intensity, and on the neutrino cross section uncertainties. The result obtained from the two runs, with an exposure of num. 7.25×10^{20} proton on target (p.o.t.) on neutrino focussing [10] and 2.95×10^{20} p.o.t. for the antineutrino focussing[11] reduced the uncertainties on the measurement of the oscillation parameters, which at combined best fit with those from atmospheric searches turns in $\Delta m^2_{atm} = 2.45 \pm 0.09 \times 10^{-3} eV^2$ for normal hierarchy and $\Delta m^2_{atm} = 2.34^{+0.10}_{-0.09} \times 10^{-3} eV^2$ for inverted hierarchy (fig. 1.2 taken from [12]).

A second fundamental observation comes from the the full compatibility between ν_μ and $\overline{\nu}_\mu$ disappearance within the atmospheric sector (fig. 1.3), as foreseen by the CPT conservation.

Regarding the “solar sector” two observations can be done to estimate the oscillation parameters, the measurement of the ν_e disappearance from the solar neutrino flux, and the measurement of the $\overline{\nu}_e$ disappearance from the neutrino flux produced

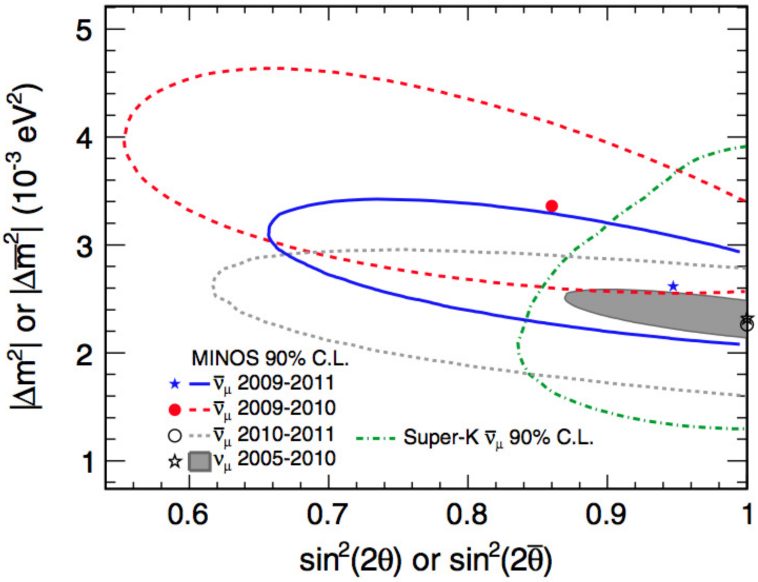

Figure 1.3: 90% C.L. region for the two phases of the $\overline{\nu}_\mu$ MINOS data taking, compared with the results for the ν_μ beam focussing. As a reference also the results from S-Kamiokande $\overline{\nu}_\mu$ are shown.

at reactors. Also in this case the consistency of the two measurements is predicted by the CPT conservation.

For the solar spectrum measurements, different detecting techniques have been used, such as the radiochemical experiment Chlorine, Gallex/GNO and SAGE, the S-kamiokande water Cherenkov measuring the energy-zenith spectrum of the electron scattering, the the SNO experiment, which as already described measured separately NC, CC and ES, and finally the Borexino experiment, which measured for the first time the neutrinos from the ^7Be electron capture.

The Δm^2 range related to the solar fluxes studies, of the order of $\sim 7.5 \times 10^{-5} eV^2$, can be studied by performing a disappearance measurement of the antineutrino flux coming from reactors. In particular, the KamLAND experiment has published in 2008 the observed spectrum of the neutrinos coming from Japanese reactors, with a mean baseline of ~ 150 km. The oscillatory behavior of the ratio of observed over expected interaction for no oscillations as a function of L/E (fig.1.4) permits a clear definition of the $\Delta m^2_{12} = 7.59 \pm 0.21 \times 10^{-5}$ and $\tan^2\theta_{12} = 0.47^{+0.06}_{-0.05}$ when combined with the results on the above mentioned solar experiments (fig. 1.5).

Finally, the second term in eq. 1.5, which regards the oscillation driven by θ_{13}, has

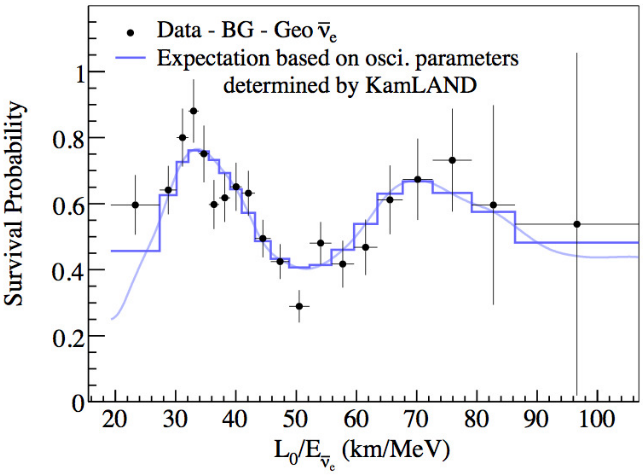

Figure 1.4: Oscillatory behavior of the reactor anti-neutrino flux observed by KamLAND (after background subtraction) over the expected flux for no-oscillation as a function of the L/E_ν parameter.

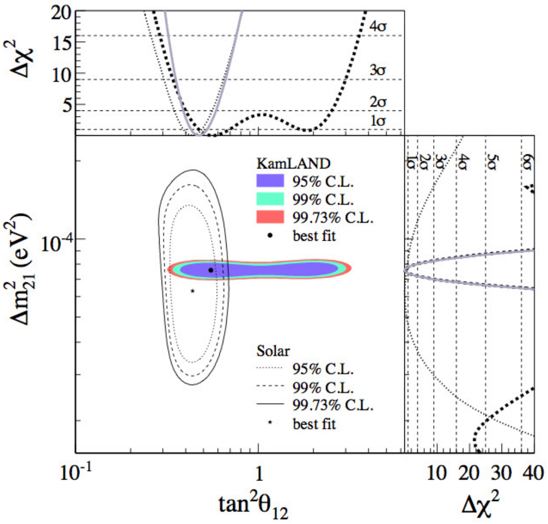

Figure 1.5: Different confident level region for both the combined solar experiment fit, and the KamLAND results. Results are clearly compatible within 1σ.

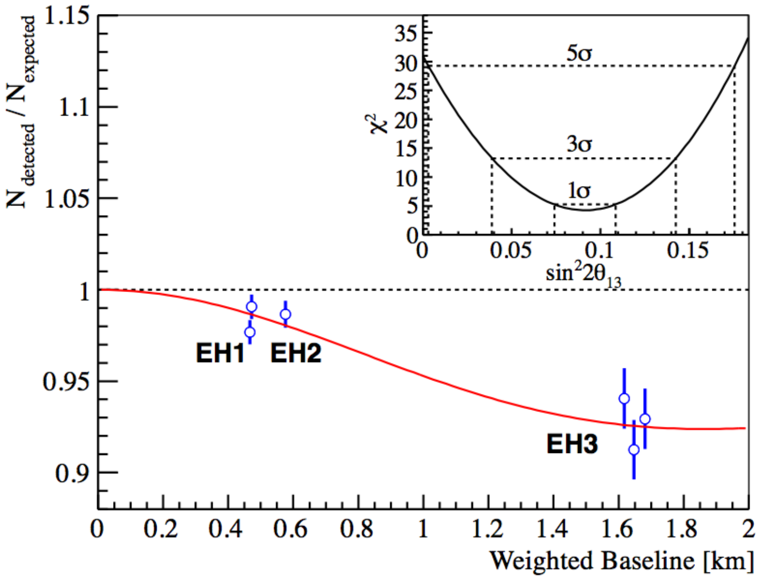

Figure 1.6: Ratio of the events detected by Daya Bay over the number of events expected in case of no-oscillation for the three sites. The best fit curve is shown in red.

been the subject of a thrilling series of experimental results in the last two years, which have definitively confirmed a non zero value for this mixing angle. The first indication of a non-null θ_{13} value has been reported in 2011 by the T2K collaboration[13], which measured a ν_e excess in a ν_μ primary beam, at 2.5σ above the expected background from beam contamination. The beam, produced at J-PARC, is detected at the Kamioka site by S-Kamiokande, after an oscillation path L=295 km and with a 2.5° off-axis inclination to reduce the neutrino beam contamination at high energy, peaking $E_\nu \simeq 0.6$ GeV. The results obtained for a overall statistic of 1.43×10^{20} p.o.t. has been the detection of 6 ν_e events over a estimated background of 1.5 ± 0.3.

In 2012 two others experiments have confirmed the results of T2K, both observing the reactor anti-neutrino disappearance from nuclear power plants. In the Daya bay experiment, the neutrino flux is produced by six 2.9 GW reactors, grouped in three couples, and is detected in three positions (EH1, EH2 and EH3) by six liquid scintillator detectors, placed at different weighted distances (470 m, 576 m and 1648 m respectively). The oscillation path measured excludes the non oscillation hypothesis at 5.1σ of C.L. and sets the best fit for the mixing angle of $\sin^2 2\theta_{13} = 0.092 \pm 0.017$ [14].

Soon after, a second experiment, RENO, have confirmed the the Daya-Bay discovery, with a similar significance of 4.9 standard deviations on the exclusion of the non-oscillation hypothesis. The RENO experimental setup is composed by two liquid scintillator detectors, placed at a weighted distance of 408 m and 1443 m respectively from six reactors, each with maximum thermal power ranging from 2.66 GW to 2.8 GW. The ratio of the measured over expected rate for no oscillation in the far detector has been $R = 0.920 \pm 0.017$ which turns into a value for the mixing angle of $\sin^2 2\theta_{13} = 0.113 \pm 0.023$ which excludes the no-oscillation hypothesis at 4.9σ [15].

The results obtained by SBL reactor experiments not only have measured the value of θ_{13}, but have also opened the way to a possible measurement of the δ_{CP} phase, which may lead to an observable phenomenology only in the case in which all the mixing parameters are non vanishing.

The possibility of a measurement of the CP violation in the leptonic sector opens a new phase of physics searches, addressed to define the ultimate nature of the neutrinos, which is still the object of fundamental questions. In this context the development of high mass, high performance detector is a required step towards the detailed study of the complex neutrino phenomenology. The ICARUS experience, proving the scalability of the LAr TPC technique to large mass, is a fundamental intermediate step towards future detectors in the kton range.

Chapter 2

ICARUS T-600 physic potential

As described in the previous chapter, the LAr TPC technique is a powerful tool to investigate neutrino's properties, thanks to its bubble chamber-like image reconstruction capabilities and to its calorimetric measurement's resolution.

After few months of commissioning phase, started in May 2010, the ICARUS T-600 detector has been running steadily on the CERN Neutrinos to Gran Sasso (CNGS) beam since October 2010, recording up to now more than 8,6 10^{19} proton on target (p.o.t). In the same period the detector has been active for the detection of non-beam related events, such as cosmic rays and atmospheric neutrinos.

In the following sub-chapters the physic potential of the T600 detector at the Gran Sasso National Laboratory (LNGS) will be presented. For each topic a brief description of the present status of the research will precede the detailed description of the results achievable with an exposure of 3 years, and a total amount of 8,6 10^{19} p.o.t. collected on the CNGS beam. For the present status of the analysis of the T600 data, the reader is referred to chapters 4 and 5.

2.1 $\nu_\mu \rightarrow \nu_\tau$ oscillation

From the first detection of electron neutrino [7] to the latest result obtained by the reactor experiments [14] [15], a clear scenario has emerged for what concerns the nature and the behavior of neutrinos. At the present status, all the results of oscillation experiments (with the exception of few anomalous results that will be addressed in chapter 7) are consistent with a three neutrino framework, where each neutrino flavor $(\nu_e, \nu_\mu, \nu_\tau\ )$ is a quantum superposition of mass eigenstates (ν_1, ν_2, ν_3), the mixing being given by a 3x3 unitary matrix, which can be divided in 3 successive rotation in the 3D space, of angle θ_{12}, θ_{23}, θ_{13}, plus an imaginary CP-violating phase $e^{-i\delta}$.

The latest results obtained by the T2K experiments, probing the $\nu_\mu \rightarrow \nu_e$ in appearance, and the conclusive observations of the reactor experiments, probing the $\overline{\nu_e} \rightarrow \overline{\nu_e}$ in disappearance, have set $\theta_{13} > 0$ at 5σ confidence level, with a combined best fit of $sin^2(\theta_{13}) = 0,021 \div 0,025$ with a 1σ error of 0,007[16], thus outlining a scenario of complete mixing among the three flavors.

Even though great results have been achieved in the study of neutrino's oscillations, a direct observation of $\nu_\mu \rightarrow \nu_\tau$ in appearance would definitively confirm the oscillation ruled by θ_{23}. This observation is extremely challenging, and needed several years of effort to be reached. For the accelerators experiments, this fact is basically due to the high energy threshold needed by the ν_τ to create a τ lepton in a CC interaction, not accessible to low energy neutrino beams, such as K2K, T2K and NuMI. From the atmospheric side, the observation of the ν_τ CC interaction is complicated by the high multiplicity of the final state of a multi-GeV ν_τ interaction, very difficult to reconstruct in water Cherenkov detectors. Despite these difficulties, recently the Super-Kampiokande (Super-K) collaboration has excluded the no-τ-appearance hypothesis at $>3\sigma$ of confidence level[17]. The Super-K analysis relies on statistical separation of ν_μ and ν_e CC and NC background from ν_τ CC based on the pion production in the hadronic τ decay. A further separation between signal and background is based on the calorimetric and topological information, as well as the particle identification, which is merged with the information on the direction of the incoming particle. The difference between down-going particles, whose spectrum is basically unaffected by oscillation, and up-going tracks, which undergoes $\nu_\mu \rightarrow \nu_\tau$ oscillation, permitted to exclude the non-oscillation hypothesis with a significance level of 3,8σ.

The CNGS project is devoted to the observation of ν_τ CC interactions in a background free ν_μ beam (the level of ν_τ contamination being kept below 10^{-7}), thus probing the $\nu_\mu \rightarrow \nu_\tau$ oscillation in appearance. The beam's composition, shown in fig. 2.1, has a dominant ν_μ component, peaked at 20 GeV, with $\overline{\nu}_\mu, \nu_e, \overline{\nu}_e$, contamination of the order of 2%, 0,8%, 0,3%, respectively. The event rates for the different interactions type is shown in tab.2.1.

Considering a baseline of 732 km, and the oscillation parameters summarized in table 2.2, the average $\nu_\mu \rightarrow \nu_\tau$ oscillation probability, convoluted with the whole ν_μ

	$E_\nu < 30$ GeV	$E_\nu < 100$ GeV	$E_\nu < 400$ GeV
ν_μ CC	537	626	651
ν_μ NC	174	203	211
ν_e CC	2.2	5.0	5.4
$\overline{\nu_\mu}$ CC	6.6	14	15
$\overline{\nu_e}$ CC	0.13	0.34	0.38

Table 2.1: Number of CNGS neutrino interactions expected for 10^{19} p.o.t. and 1 kton mass.

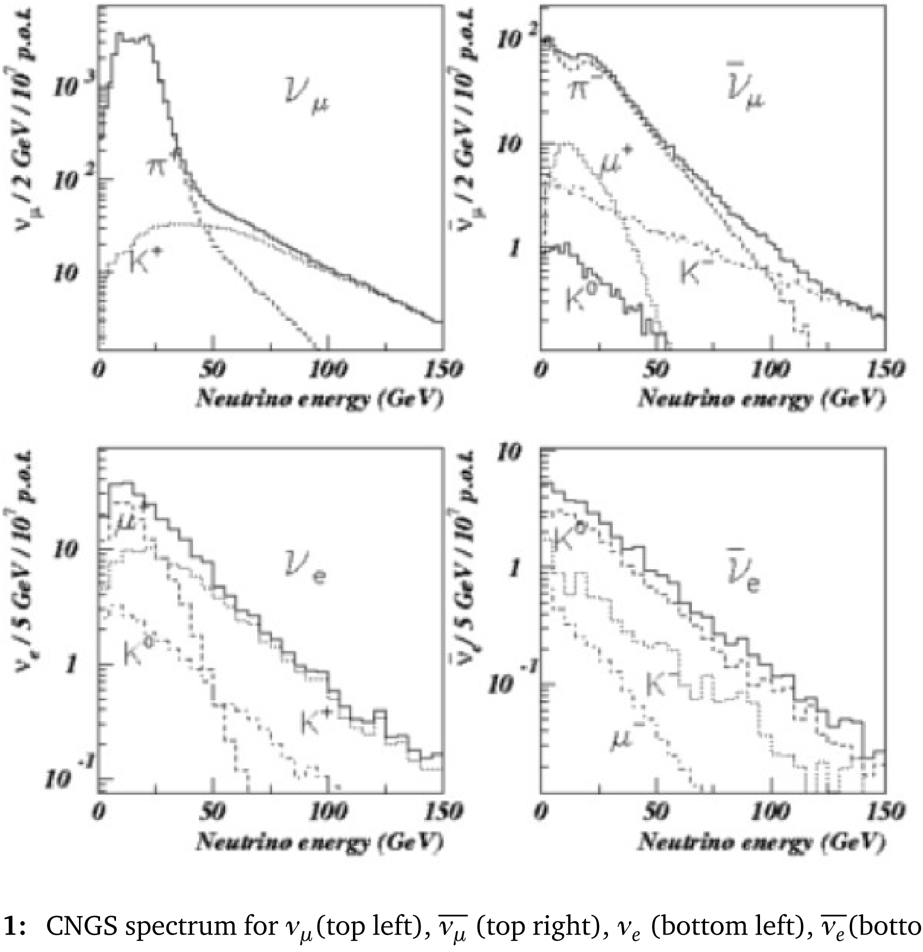

Figure 2.1: CNGS spectrum for ν_μ(top left), $\overline{\nu_\mu}$ (top right), ν_e (bottom left), $\overline{\nu_e}$(bottom right). The contribution of different parent particles is also indicated.

Parameter	Value
θ_{12}	35.0°
θ_{13}	9.22°
θ_{23}	45.0°
Δm^2_{12}	$6.0 \times 10^{-5}\ eV^2$
Δm^2_{23}	$2.5 \times 10^{-3}\ eV^2$
δ_{CP}	0

Table 2.2: Parameters used for the simulation of the CNGS neutrino oscillations

spectrum, is:

$$P_{\nu_\mu \to \nu_\tau} \approx sin^2(2\theta_{23}) < sin^2(1,27\Delta m^2 732/E[GeV]) >= 1,2\% \qquad (2.1)$$

Once convoluted the ν_τ flux at LNGS with the ν_τ cross section, considering a fiducial volume of 470 ton of LAr, the number of ν_τ CC-interactions, for a 10^{20} p.o.t. statistic, results:

$$N_{\nu_\tau CC} = \int dE \phi^{GS} \sin^2(2\theta_{23}) \sin^2(\frac{1.27\Delta m^2 723}{E}) \sigma_\tau^{CC} \epsilon \text{Expo} = 17 \qquad (2.2)$$

where ϕ^{GS} is the unoscillated flux at Gran Sasso site, σ_τ^{CC} is the ν_τ cross section for CC interaction, ϵ is the detection efficiency and Expo is the total exposure, expressed in kton x year. Due to the precise electron reconstruction capability of ICARUS, the golden channel for the detection of ν_τ appearance is the decay of tau into electron plus two neutrinos, with a branching ratio of B($\tau \to e$)=0,18, resulting in 3 ν_τ CC with tau lepton decaying into electron during the whole data-taking. This channel gives the fundamental advantage of an intrinsically small background source, which comes mainly from CC interaction of the ν_e intrinsic beam's contamination and to θ_{13} oscillation. To discriminate between these kinds of events two kind of cuts are applied to data:

Energy cut : in the $\tau \to e$ decay, part of the tau energy is carried by the two neutrinos emitted in the process. This fact reduces the energy of the emitted electron and thus the total visible energy ($E_{visible}$) w.r.t. ν_e CC interaction. A second contribution which enhance the difference of the $E_{visible}$ in the two cases comes from the shape of the ν_μ energy spectrum, which is peaked at lower energy w.r.t. ν_e CC spectrum.

Kinematical cut : the two neutrinos coming from tau decay carry a part of its momentum. The reduction of the total momentum of the event becomes clear in the transverse plane, producing events with a higher missing transverse momentum (PT_{miss}). Tau neutrino events will consequently result unbalanced for what concerns the transverse momentum. A second cut, based on the analysis of the transverse momentum of the different components of the event, can be applied on the basis of the fraction of the leptonic transverse momentum, which turns out to be smaller for ν_τ CC with$\tau \rightarrow$ e due to both a higher value of the transverse missing momentum (PT_{miss}) and a lower value of of the leptonic transverse momentum (PT_{lep}).

A multivariate likelihood function has been used to maximize the τ appearance sensitivity, by taking into account the correlation between the following three variables:

- $E_{visible}$
- $\rho_l = PT_{lep}/(PT_{miss} + PT_{lep} + PT_{had})$
- PT_{miss}

Applying the likelihood function to MC simulations for the signal and background it has been possible to define the kinematical cuts that maximize the sensitivity, resulting in 1÷2 event with less than 0,1 background, with the above-mentioned exposure of 10^{20} p.o.t. on a 470 ton of active volume. A looser kinematical cut will allow increasing the efficiency on signal selection, at the expenses of signal over background ratio.

Another source of background comes from NC interaction, or ν_μ CC interaction in which the muon is misidentified, with the production of a π^0 at the interaction vertex, wrongly identified as an electron. The main π^0 decay channel is into two photons (Br=98,8%), which, in turn, create an e+e- pair, and in Dalitz mode (Br=1,2%) in which a single photon plus a e+e- pair is generated. The e+e- pair from the photon conversion can mimic an electromagnetic shower created by a single electron generated at the interaction vertex, and can be distinguished by two distinctive features:

Topology : in the case of $\pi^0 \rightarrow \gamma\gamma$ the mm spatial resolution of the T600 permits a clear separation of the point of photon conversion into e+e- pair from the neutrino interaction vertex.

dE/dx : at the beginning of the e.m. shower in the case of the e+e- pairs the ionization is double w.r.t the case of a single electron. It is thus possible to distinguish the two cases by observing the ionization of the first centimeters of the shower development, which is close to one m.i.p. for a cascade generated by a single e- and to two m.i,p. in the case of a e+e- pair.

π^0 **mass** : in the case of a π^0 decay, it is possible to reconstruct the π^0 invariant mass, by correlating the energy of the two e+e- pairs and the angle created by the two e.m. shower w.r.t. the neutrino interaction vertex.

Combining these three characteristics, an e-/π^0 rejection factor of $\sim 10^3$ has been demonstrated to be possible in LAr TPC [18], thus reducing the NC+π^0 background to a negligible value.

Even if the statistics expected at the LNGS site is low for what concerns the $\overline{\nu}_\tau$ appearance, the CNGS data taking with the ICARUS detector represent a fundamental step towards future experiments based on LAr TPCs, proving capabilities of this kind of detectors, in particularly the energy resolution and the e/π^0 discrimination. For this reason the CNGS data taking represented the top priority during the 2010, 2011 and 2012 runs.

2.2 Nucleon decay

The Grand Unification (GU) of the electro-weak and strong interaction into a single gauge represent an appealing perspective, reinforced by the apparent convergence of the three coupling constant at large energy scale.

One of the most unique predictions of Grand Unified Theories (GUTs) is the violation of the baryon number, with a hadron decaying into an anti-lepton plus one or more meson (being B-L conserved in all these theories). It results clear that a powerful experimental tool for probing GUTs is represented by the searches of proton or bound neutron decay. In fact, the results obtained in this field by Super-K, setting a lower limit for the decaying of the proton $\tau/B(p \rightarrow e + \pi^0) > 8,2 \times 10^{33}$ years [19], have

Decay mode	Partial lifetime lower limit (years)
$p \to e^+ + \pi^0$	8.2×10^{33} [19]
$p \to \mu^+ + \pi^0$	6.6×10^{33} [19]
$p \to \overline{\nu} + K^+$	2.3×10^{33}[20]
$p \to e^+ + K^0$	8.2×10^{33} [20]
$n \to \overline{\nu} + K^0$	1.3×10^{32} [20]
$p \to \mu^+ + K^0$	1.6×10^{33} [21]

Table 2.3: Super-K lower limit on proton decay partial lifetime, for the main decay channels at 90% C.L.

already ruled out the minimal SU(5) model, which predicts a lifetime of the proton $< 10^{32}$ in this channel. A possible theoretical explanation of such a high $p \to e + \pi^0$ lifetime could be given by super symmetric (SUSY) theories: in these theories the transition of a quark into a quark of the same family is strongly suppressed, thus resulting in a$p \to e + \pi^0$ lifetime 4 orders of magnitude higher w.r.t. SU(5); the value predicted ($>10^{35}$) is therefore still compatible with the experimental limits. On the other hand, the only other quark family kinematically allowed in the proton or neutron decay is the strange quark; therefore for these theories the favorite decay channels are proton or neutron going into a kaon, i.e. $p \to \overline{\nu} + K^+$, $p \to \mu^+ + K^0$, $p \to e^+ + K^0$, $n \to \overline{\nu} + K^0$. All these channels have been studied by Super-K, setting limits that are still compatible with super-symmetric models (tab. 2.3).

Although the water Cherenkov experiment has a great advantage in term of exposure, both for the huge mass and for the long running period, the impossibility to look directly at K^+ meson, whose momentum is below the Cherenkov threshold, but only to its decay products, forces to relies on the statistical suppression of a strong background for the observation of the proton decay, thus resulting in a low detection efficiency. One of the great advantages of LAr is the imaging capability of all the charged particles, including the K^+ meson; the efficiency on these decay channels results much higher, and the discovery of the proton decaying into K^+ may be done on the base of single event detection. In fact the tag based on the presence of a kaon or a pion, accompanied by a charge lepton, with total measured energy equal to the proton mass, are powerful enough to completely suppress the background. In addition, a clear understanding of the phenomenon of the proton decay would require a precise measurement of all possible branching ratios, which could be with LAr-TPCs, thanks to their powerful background rejection and redundancy of measurements. For any proton decay experiment, the lower limits on partial lifetime τ/B can be derived from the formula:

$$(\tau/B)_p > 2,69/S \times \text{Expo} \times \epsilon \times 10^{32} yrs \tag{2.3}$$

$$(\tau/B)_n > 3,29/S \times \text{Expo} \times \epsilon \times 10^{32} yrs \tag{2.4}$$

where Expo is the full detector exposure in kilotons per year, ϵ is the signal selection efficiency and S is the 90% C.L. upper limit on the number of observed signal events, which can be found solving the equation:

$$\frac{\sum_{n=0}^{n_0} P(n, b+S)}{\sum_{n=0}^{n_0} P(n, b)} = \alpha \tag{2.5}$$

where P(n,μ) is the Poisson probability for n events given an average of μ, b is the expected background, α is 0.1 for a 90% C.L. interval and n_0 is the nearest integer to b.

To determine the value of background and the detection efficiency expected for the ICARUS T600 detector, a detailed MC simulation has been carried out, generating a sample of atmospheric neutrinos (the dominant background for nucleon decay searches) expected for an exposure of 1Mton/year, and 2000 events for each decay channel of interest [22]. The results of this analysis are reported in tab.2.4. The evident loss of efficiency present in case of π production is due to the high absorption cross section of the π in the Ar nucleus. This results in a 40% of unbalanced events, with total visible energy lower than expected. For these events, an inclusive analysis can still be done, but the S/B ratio drops significantly.

In fig. 2.2 are reported the limits achievable by the T600 detector as a function of the exposure; it is worth noting that in few channels it is possible to improve the present experimental sensitivities with a short exposure.

2.3 Atmospheric neutrinos

The outstanding results obtained by S-Kamiokande on the atmospheric neutrino studies, have been not only the first incontrovertible proof of neutrino oscillations, but

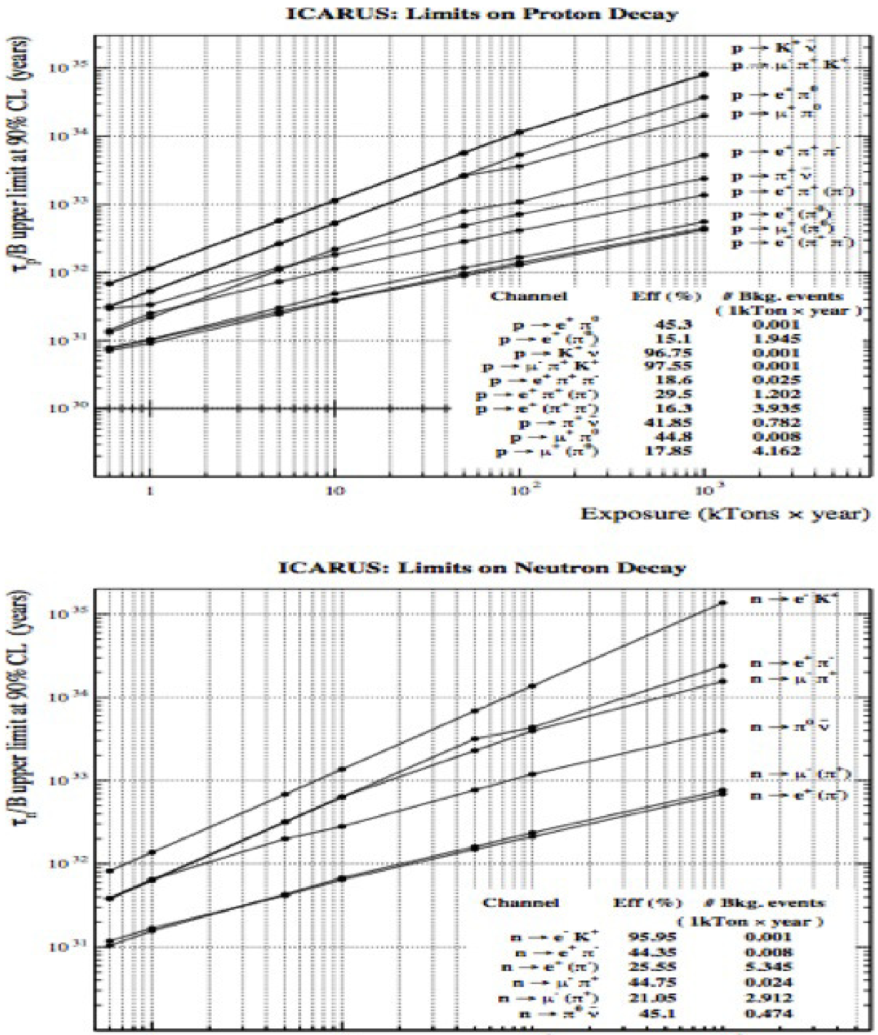

Channel	Eff (%)	# Bkg. events (1kTon × year)
$p \to e^+ \pi^0$	45.3	0.001
$p \to e^+ (\pi^0)$	15.1	1.945
$p \to K^+ \nu$	96.75	0.001
$p \to \mu^- \pi^+ K^+$	97.55	0.001
$p \to e^+ \pi^+ \pi^-$	18.6	0.025
$p \to e^+ \pi^+ (\pi^-)$	29.5	1.202
$p \to e^+ (\pi^+ \pi^-)$	16.3	3.935
$p \to \pi^+ \nu$	41.85	0.782
$p \to \mu^+ \pi^0$	44.8	0.008
$p \to \mu^+ (\pi^0)$	17.85	4.162

Channel	Eff (%)	# Bkg. events (1kTon × year)
$n \to e^- K^+$	95.95	0.001
$n \to e^+ \pi^-$	44.35	0.008
$n \to e^+ (\pi^-)$	25.55	5.345
$n \to \mu^- \pi^+$	44.75	0.024
$n \to \mu^- (\pi^+)$	21.05	2.912
$n \to \pi^0 \bar{\nu}$	45.1	0.474

Figure 2.2: Sensitivity of proton (top) and neutron (bottom) decay searches as a function of the exposure, for different decay channels.

Channel	**Efficiency (%)**	**Background (1 kTon×year)**	**τ/B Limit ×10^{30} yrs (1 kTon×year)**	**PDG limit ×10^{30} yrs**	**Needed Exposure to reach PDG (kTon×year)**
$p \to K^+\overline{\nu}$	96.75	0.001	113	2300	20.36
$p \to \mu^-\pi^+K^+$	97.55	0.001	114	245	2.15
$p \to e^+\pi^+\pi^-$	18.6	0.025	22	82	3.78
$p \to \pi^+\overline{\nu}$	41.85	0.782	23	25	0.52
$n \to e^-K^+$	95.95	0.000	137	32	0.24
$n \to e^+\pi^-$	44.35	0.008	62	158	2.50
$n \to \mu^+\pi^-$	44.75	0.024	64	100	1.57
$n \to \pi^0\overline{\nu}$	45.10	0.474	40	112	2.43

Table 2.4: Summary of the main nucleon decay channel analysis. The fifth and sixth columns shows respectively the PDG-2012 limit at 90% C.L[23], and the exposure needed by Icarus T600 to improve the PDG results.

have also set tight constraints on the mixing parameters of the atmospheric sector. At the present status, however, systematic experimental errors represent the limiting factor for a better determination of the mixing parameters.

LAr technology could give an important contribution in understanding systematics of water Cherenkov detectors, thanks to the capability of observing both neutral current (NC) and charged current (CC) interactions for all neutrino flavors, and to its reconstruction capability of complex multi-prong events. Moreover, LAr TPC could investigate the spectrum at lower energy, reaching an energy threshold as low as 10 MeV.

The low energy region of the spectrum is of particular interest in view of the argument [24]that a precise measurement of the oscillations effects in the Sub-GeV range would be the best possible tool to measure θ_{23} and its octant. By exploiting the interference of the θ_{23} term in the 1-2 mixing sector, the fraction of oscillated ν_e can be expressed as:

$$\frac{(\nu_e)_{osc}}{(\nu_e)_0} = 1 + < P^{12}_{2flav} > (r_{\mu e}\cos^2\theta_{23} - 1) \tag{2.6}$$

where $r_{\mu e}$ is the ν_μ/ν_e unoscillated flux ratio, and $< P^{12}_{2flav} >$ is the 2-flavor oscillation expression in the 1-2 sector, $\nu_e \to \nu_{\mu/\tau}$.

It is worth noticing that, from a global fit of data, if in normal hierarchy (NH) the

	Sub-GeV	Multi GeV	Total
Electron-like	33	8	41
Muon-like	30	1	31

Table 2.5: Atmospheric contained events in ICARUS T600 for an exposure of 1 kTon x year

possibility of $sin^2(\theta_{23}) > 0,5$ is disfavored at almost 3σ, for inverted hierarchy (IH) this possibility is still within the 2σ limit [16]. A precise measurement, based on an alternative technique with different systematic biases, would be extremely valuable in defining the 2-3 mixing parameters with high accuracy.

Even though the huge statistic required for such an high precision measurement is well beyond the possibility of ICARUS T-600, the observation of atmospheric neutrinos represents a fundamental step in view of a more detailed study, which could only be performed by much more massive LAr detectors. For the ICARUS detector, for which an exposure of 1kton x year is a reasonable assumption, the atmospheric neutrino's event rate has been carefully studied, both in the Sub-GeV and Multi-GeV range[25]. The total number of muon-like interaction, in which a $\mu/\overline{\mu}$ is identified, is 68 for an exposure of 1 kton x year. For electron-like interaction, with the identification of an e+/e-, 78 events are expected. These numbers reduce to 31 and 41 respectively after the containment cut, i.e. requiring that 95% of the available energy of all leptons above 10 MeV and all charged hadrons and π^0 above 50 MeV has to be deposited in the sensitive volume, no requirements being given for neutral hadrons. The containment cut defines a golden sample for which the energy and momentum could be both accurately measured. However, even for partially contained events the muon momentum could be estimated via multiple scattering. The contained sample can be divided for energy range and particle productions, the predictions being summarized in tab. 2.5.

2.4 Supernovae Neutrinos

After the observation of the SN1987 [26],[27] , it became clear that neutrino detectors could play a crucial role in understanding the physics of supernovae explosion. LAr TPCs in particular are well suited for these studies, thanks to their calorimetric resolution, directional information and the capability to study both NC and CC. In fact, supernovae neutrinos can be detected in LAr via four processes: elastic scattering

Reaction	SN at 10 kpc	SN at 50 kpc
elastic	8 (8)	0 (0)
CC	153 (200)	6 (8)
NC	182 (182)	7 (7)
total	343 (390)	13 (15)

Table 2.6: Supernovae events expected in Icarus T600 for a distance of 10 and 50 kpc in normal (inverted) hierarchy

on electrons for all flavors, absorption of ν_e on Argon nuclei with the production of excited K nucleus, absorption of $\overline{\nu_e}$ on Argon nuclei with the production of excited Cl nuclei and NC interaction on Argon nuclei for all flavors. The possibility to disentangle NC and CC interaction is fundamental to decouple the supernova physics from the neutrino oscillation physics. The scattering process is of particular interest, since it has the potential to determine the supernova source through the direction of the electron, which keeps traces of the direction of the incoming neutrino. Supernovae neutrinos are expected to be background free in LAr-TPC, since the neutrino burst has a typical duration of tens of seconds and the radioactive background is expected to be negligible in this short period, as well as the background coming from the atmospheric neutrinos and the high energy tail of solar neutrinos.

The number of events foreseen for ICARUS T600 in case of a Supernova explosion strongly depends on the distance and the Supernova and on its type; as a reference in table 2.6 the number of interaction is computed starting from the flux measured by Kamiokande II, for SN1987A in Magellan cloud (50 kpc distance) and at 10 kpc of distance.

Even if the ICARUS run at LNGS will not provide a sufficient statistics for SuperNovae studies, both in terms of yeas of data taking and in terms of active detector mass, it will provide useful informations on the background and the capabilities of LAr detectors in triggering low energy events.

Chapter 3

The ICARUS T600 Trigger setup

Liquid argon TPCs have been firstly proposed by C.Rubbia in 1977 [1] and can be seen as the electronic evolution of bubble chambers: in fact these novel detectors maintain good calorimetric and spatial resolution, while constituting a self-triggered, always active detecting volume. Moreover, being the signal acquired in digital form, it can be treated with the tools of digital signal processing.

These kind of detector are conceived to exploit the two main processes which occur as a charged particle pass through a volume of liquid argon: emission of scintillation light and creation of electron-ion pairs. While the scintillation light gives a prompt signal, corresponding to the time of interaction, the ionization charge is collected by a segmented anode, which gives a 2D image of the ionizing event. By merging the time of arrival of electrons with the fixed drift velocity and the time of interaction, a complete 3D image of the event is made possible. Calorimetric measurements are based on the ionization density, which is proportional to the charge signal collected by the anode.

In this section a brief overview of the ICARUS T600 detector will be given, a more detailed description could be found e.g. in [28].

3.1 The ICARUS T-600 detector

The ICARUS T-600 detector is composed by two identical cryostats, which contain the two modules, the western numbered I, the eastern II. Each module is in turn divided into two drift chambers (Left and Right) by a common cathode plane, placed at the center of the cryostat. The inner dimension of each module is 19,6 m along the beam direction, 3,9 m in height and 3,6 along the drift direction.

Three planes of wires compose each drift chamber; the first one, named Induction 1, faces the cathode and is constituted by horizontal wires, while the other two, Induction 2 and Collection, are inclined by 60° w.r.t. the first plane. The distance between the planes, 3mm, is identical to the wires spacing. The electric field inside the active volume is kept fixed at a nominal value of 500 V/cm by polarizing the cathode at 75 kV. This electric field guarantees a homogeneous drift velocity of $1,56mm/\mu s$, corresponding to a maximum drift time of 1 ms, being the drift path 1,5 m. The electric field between the wire planes is set according to the "transparency rule", which guarantees that the charge is not collected by the first two planes of wires, but is let free to travel toward the last plane:

$$\frac{E_2}{E_1} > 1 + \frac{\rho}{1-\rho} \tag{3.1}$$

where $\rho = 2\pi \times \frac{r}{p}$ is an a-dimensional parameter given by the plane geometry, being p the wire pitch and r their radius, and E_1 and E_2 the electric fields before and after the wire plane respectively.

A total of 2112 wires composes the Induction 1 plane, while the number of wires in both Induction 2 and Collection is 5600. The waveform of the signal induced (collected) on each wire is recorded by a complete read-out chain, with an acquisition window slightly larger than a complete drift period. The waveform outside the physical drift is used to monitor the electronic noise level.

The read-out chain has a modularity of 32 wires, and it's composed by 3 boards: the decoupling board, the analog board and the digital board(fig.3.1).

The decoupling board is used to distribute the HV to the wires, and to decouple it form the front-end amplifier via a 4,7 nF capacitor. It also houses 32 capacitors of 1 pF for calibration purpose.

The analog board , which follows the decoupling board, houses a low noise front-end amplifier, implementing a Radeka folded cascode architecture. The input stage is constituted by a couple of j-fet transistor in parallel, which guarantees low noise and high transconductance, followed by a custom BiCMOS chip, which implements the rest of the amplifying architecture, the signal shaping and a final stage to restore the baseline to a fixed value. This setup has shown an excellent noise behavior, showing an equivalent noise charge (E.N.C.) of 1’000 e^- over a input capacitance $C_D \simeq 400pF$. This value permits a clear signal definition, being the number of electrons recorded in case of a horizontal minimum ionizing particle (m.i.p.) of the order of 10’000 electrons. The amplifying stage is followed by an analog to digital conversion, performed by four 10 bit ADC, sampling at 20 MHz. The signal coming form 8 consecutive wires is multiplexed before entering the ADC, thus resulting in an effective sampling rate of 2,5 MHz per wire, corresponding to a sampling period of 400ns. After the digitization, signals are sent to the digital board via a 40 MHz serial link.

The digital board is addressed to handle the data-flow, storing the incoming data in multi event circular buffers (MEB). As a trigger occurs, the writing process is redirected to the next free buffer, leaving the data written before the trigger to be read by the data acquisition. Being the system based on a stop-trigger architecture, the trigger actually tag the end of the physical event. This MEB structure permits the detector to be continuously sensitive, avoiding any dead time correlated with the DAQ process, until the trigger rate overwhelms the DAQ maximum bandwidth. Another important feature implemented in the digital board is a loss-less data compression, which reduces the data size by a factor

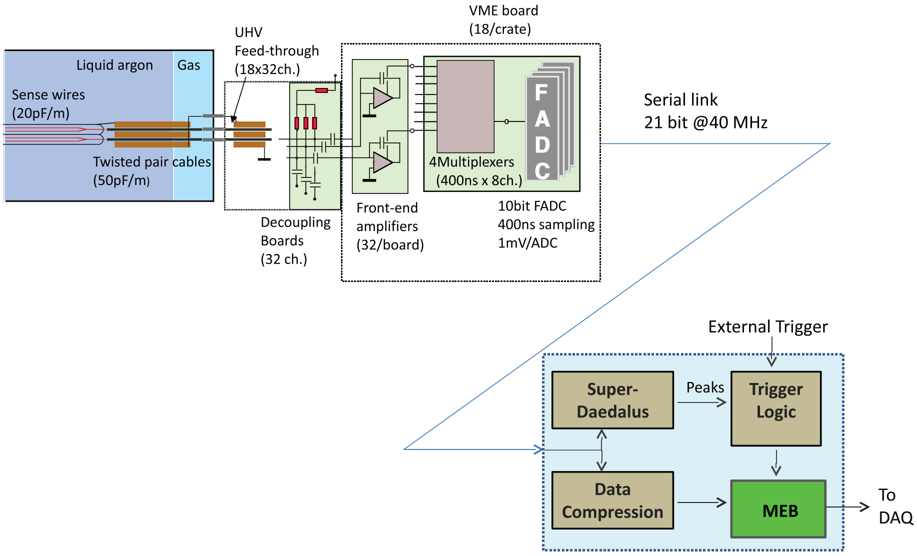

Figure 3.1: Schematic of the ICARUS T600 read-out electronics.

four. Finally, the digital board houses a controller, which handles external trigger as well as local trigger, generated by a hit finding chip that will be described in chapter 4.

Read-out electronics is housed in 96 racks: 80 racks containing each 18 read-out chains, 9 for Collection wires and 9 for Induction 2 wires, for a total of 576 wires, while the remaining 16 racks contain the electronic for Induction 1 and for the Collection and Induction 2 wires placed at the extremity of the detector. For each rack, a CPU collects the data buffered on the digital board by mean of a VME bus, and sends them over a fast Ethernet connection to the central DAQ. The bandwidth of the VME bus and of the Ethernet connection sets an upper limit to the DAQ build time of 1sec per full drift event. In addiction to the charge signal collected by the TPC wires, ICARUS records also the scintillation light, by mean of 74 8” Ltd 9357FLA photomultiplier tubes (PMT) dipped in Liquid Argon, behind the wire planes. The number and the position of PMT’s changes from chamber to chamber, and is summarized in fig.(3.2).

The signal from each amplifier is integrated with a time constant of $10\mu s$ by a costume module, which has two outputs. An electronic chain similar to that used for the wire signal, except for the higher sampling rate of 20MHz, records one output. The other output is used for the generation of a trigger signal: all the PMT signals coming from the same chamber are summed and integrated again, with a time constant of $30\mu s$, to add up both the slow and the fast component of scintillation light. Two copies of this sum signal are generated, one is recorded together with the individual PMT signals, while the second, discriminated with a fixed threshold, is used to generate a trigger signal for each chamber.

3.2 Trigger resources

The physics programe of the ICARUS T-600 detector spans over several orders of magnitude for what concerns the event energy, ranging from few tens of MeV for the low energy tail of the atmospheric neutrino spectrum, to several GeV for CNGS related events. The topology of the events varies as well, and so does the expected event rate of each kind of events, which can vary from a ten of CNGS events per day, to a burst of some tens of events in few seconds in case of a Supernova collapse.

To build a flexible trigger, which must be efficient detecting relevant events, while keeping as low as possible the rate of misidentification, it is necessary to mix together all the trigger resources available: scintillation light collected by PMTs, timing synchronization to the CNGS extractions and charge signal collected on wires. The former two elements, which have been the basis of the trigger system for 2010 and 2011 run, will be described in this section, while the exploitation of wire signal, which has been introduced in 2011 for CNGS events and in 2012 for atmospheric, will be described in detail in the next chapter.

3.2.1 PMT trigger

The basic trigger of the ICARUS detector relies on the prompt signal generated by PMTs, which collect scintillation light. The importance of the PMT signal is not limited to the trigger system, as it is the only tool to define the precise time of interaction, thus

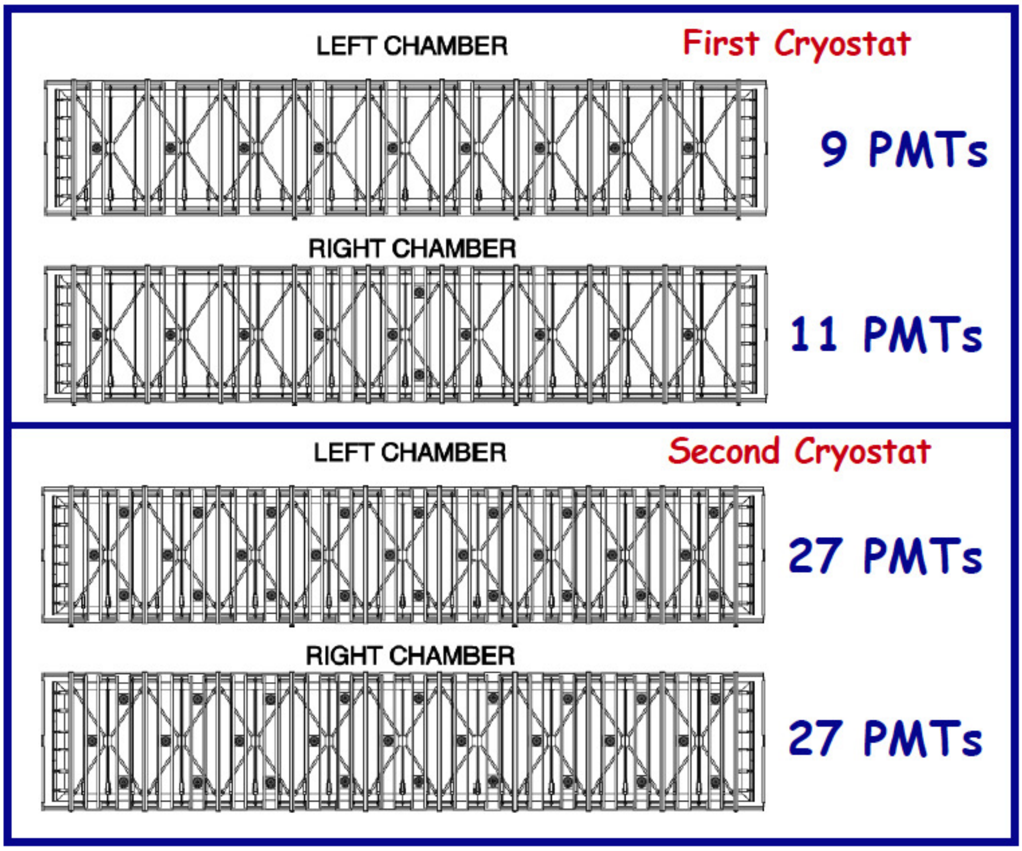

Figure 3.2: Disposition of the PMTs on the four chambers.

permitting a complete 3D reconstruction of events.

Scintillation light emission in Liquid Argon has been widely studied [29], and can be described by two steps of de-excitation, with different time constant. In fact, as a charged particle crosses the detector, it creates a trail of excited Ar atoms, *Ar, and of ionized Ar atoms, Ar+. The *Ar binds to other not-excited Ar atoms, thus creating a *Ar2 dimer. The *Ar2 dimer is unstable and decays to two single Ar atoms, with a time constant of $\sim 6ns$ emitting a 128nm photon. The Ar+ instead creates an Ar+2 molecule that recombines with an electron and de-excites to a *Ar2 dimer, which undergoes the same de-excitation described above. The time constant of this second process ranges from 1 to 1,7 μs. Both de-excitations produce a photon with a wavelength of 128 nm. A thin film of tetraphenyl-butadiene (TPB) has been applied to the surfaces of PMTs, acting as a wavelength shifter, from the VUV region of the emitted photons, to the PMT-sensitive region.

The equalization of the PMT gain, carried out with several calibration campaign during the 2010-2012 run, has permitted to set a threshold corresponding to $\sim 200phe^-$ for the module I, and $\sim 150phe^-$ for the module II on the sum signal coming from each chamber. This relatively low value of phe^- has the drawback of increasing the trigger rate of a single chamber to more than 20 Hz, much above the maximum trigger rate that can be handled by the DAQ. In order to exploit those signals two separate triggers have been set up.

The trigger on cosmic rays, atmospherics and other non-beam related events relies on the transparency of the cathode, which let almost 50% of the light passing through. For this reason, even when an event is localized only in one chamber, a fraction of light is collected by the PMTs of the other chamber of the same Module. By requiring the coincidence of the PMT signal in both the chambers of the same Module (fig.3.3) it is possible to keep the overall trigger rate to acceptable level (<200mHz), but at the cost of increasing the trigger energy threshold, reducing the efficiency for events with $E_{dep} \leq\sim 1GeV$.

To study the efficiency of the PMT trigger setup an automatic program, named Cosmic Event Filter (C.E.F.), which measures the deposited energy of each event, has been developed. It relies on the detection of clusters of at least 10 hits on 10 consecutive wires, and calculates the deposited energy as the sum of the hit areas (A_i), multiplied by the following factors:

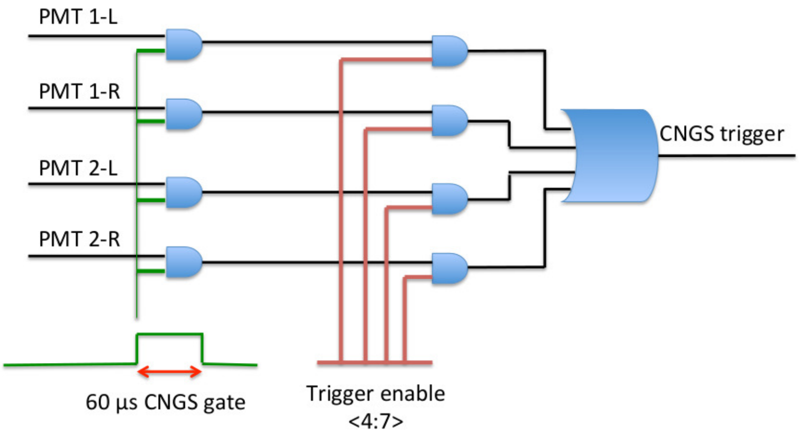

Figure 3.3: Schematics of the PMT trigger setup for atmospheric events.

$$\Delta E_i \equiv \frac{CW}{R} \exp^{\frac{(t_i - t_0)}{\tau_e}} A_i \tag{3.2}$$

- **C** that is the electronic calibration factor, and is used for the conversion from ADC counts to charge in femto Coulombs.
- **W**= $(23.6^{+0.5}_{-0.3})$ eV that is the energy needed to create an electron-ion pair, i.e. the work function for liquid Argon
- **R** that is the factor used for correcting for the electron-ion recombination, a process that depends upon the Electric drift field and the ionization density dE/dx according to the Birks law:

  $$R = \frac{a}{1 + k_B \frac{\Delta E}{\Delta x}} \tag{3.3}$$

  being a a parameter ranging from 0 to 1, and k_B the Birks factor. For a m.i.p the factor R=0.65, while for the CNGS events an average value over the expected events is R=0.73.
- the exponential factor $\exp^{\frac{(t_i - t_0)}{\tau_e}}$ that corrects for the the attenuation of the signal due to the argon impurities, quantified by the electron mean lifetime τ_e

To remove as much as possible the fake hits, a cut is applied to the wires that shows a high noise level or a problematic behavior. The cut is based on the RMS of the wire signal, calculated on the samples outside the physical drift: if a wire exhibits an RMS higher than 3ADC count it is removed from the analysis. The RMS cut must be compared to a mean of 1,5 ADC counts for the whole detector. This automatic filtering process has been qualified over a set of 428 atmospheric events from real data collected during the 2010 run, 3540 Montecarlo events and on 1196 empty event, showing an efficiency of 99.4% on events with $E_{dep} \geq 50 MeV$ for the Montecarlo dataset, 98.9 % for the real dataset, combined with a fraction of empty misidentification of 10^{-3}.

A first analysis has been carried out on a data sample corresponding to $\sim$ 67 hours of data-taking in August 2011. The spectral distribution of the events acquired in this period, and analyzed by the C.E.F. has been compared to the result of a Montecarlo simulation for the flux expected at the Gran Sasso site. The result of the comparison, shown in fig. 3.4, points out a lack of the efficiency of the PMT setup with respect to the expectation.

This inefficiency, which begins at an energy of 1GeV, is present in both the modules, but is more evident in the second. After a detailed analysis of the PMT behavior, it has emerged that the problem is related with the layout of PMT HV distribution circuit, which is dipped into the liquid argon and cannot be modified. The effect of this layout is the generation of a negative after pulse that follows each PMT signal. When the PMT signals are summed together, since their response is not perfectly on-time, the after pulse of the first PMT annihilate the signal of the following.

To overcome to this problem, recovering as much as possible all the signal from the PMTs, a new biasing electronic has been developed. In the new layout (fig. 3.5) a first integration circuit is introduced right into the biasing loop of each PMT. With this new architecture, the after pulse of each signal is integrated with the positive part, resulting in a much smoother signal from the single PMTs. After this first integration, the PMTs are summed together and integrated a second time, to add up the fast and the slow components of the scintillation light.

The new PMT electronics has been installed between the end of 2011 and the beginning of 2012, and a second run of $\sim$ 129 hours has been analyzed to check the results of the electronic upgrades. The comparison of the spectrum acquired with the one obtained from a complete Montecarlo simulation, show that the improvements have increased the efficiency on the eastern module (tab.3.1), but didn't recover completely, and the overall trigger rate is still 10% below the expectations (fig. 3.6).

A second trigger based on the PMT activity has been developed for CNGS events, for which the trigger requires only the PMT signal coming from a single chamber in coincidence with a 60 μs gate, enabled at the expected CNGS beam arrival time (fig. 3.7). This time synchronization not only allows reducing the trigger threshold for

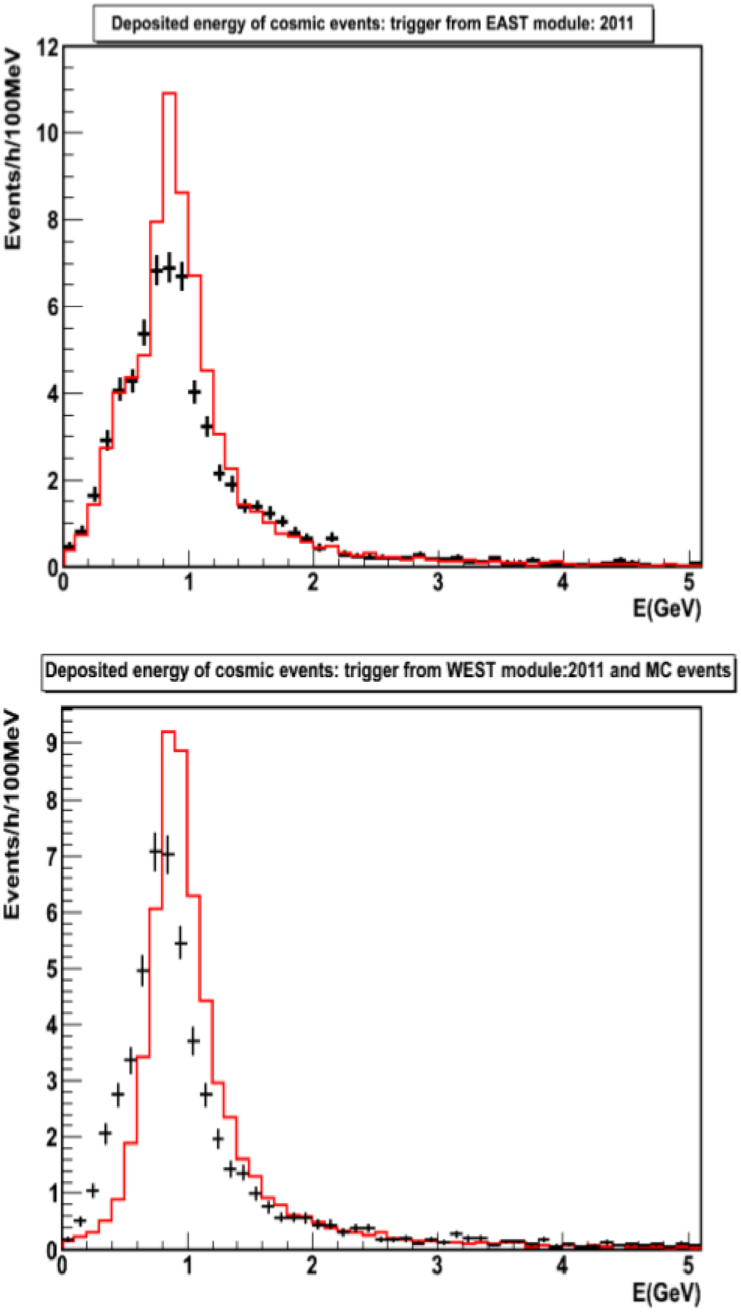

Figure 3.4: The results of the C.E.F. applied to a 2011data sample (black dot) compared with the expectation from a dedicated Montecarlo simulation (red line) for the eastern module (top) and the western module (bottom).

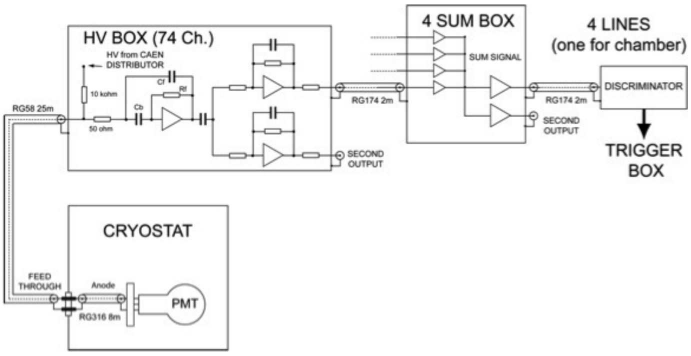

Figure 3.5: New layout of the PMT biasing electronics

	2011		2012	
	East	West	East	West
Measured Trigger rate [mHz]	17.2	15.3	21.1	14.7
Expected Trigger rate [mHz]	20.0	15.8	23.9	16.1

Table 3.1: Trigger rates for both modules, for the 2011 (left) and 2012 (right) data taking w.r.t. the Montecarlo expectation

CNGS events, but also permits to have a tag on beam-related candidates events. The possibility to trigger on the activity of the PMTs coming from a single chamber greatly reduces the inefficiency which affects the trigger for the atmospheric events.

3.2.2 Time synchronization

The time synchronization with the CNGS beam extraction is based on the reception of an “early warning” (EW) message sent from CERN, and the time synchronization with the external lab clock, through a time link established between the external lab and the underground experimental hall. This time synchronization permits the opening of a 60 μs width CNGS-gate, containing the extraction, which lasts 10,5 μs. The EW message is a UDP packet which is sent ∼80 ms before each CNGS extraction and encodes the time predicted for the following spill; being these packets sent over a non-deterministic, and non-reliable, network, it is possible that some EW message got lost due to the Ethernet packet-loss, or that some packets arrives too late to permits to arm the trigger properly. This behavior has been monitored for more than two months during 2011 run, by comparing the EW messages received on time at LNGS with the CERN database, where the precise time and the intensity of all the effective extraction are recorded. The mean packet loss, for the period going from 8^{th} July to

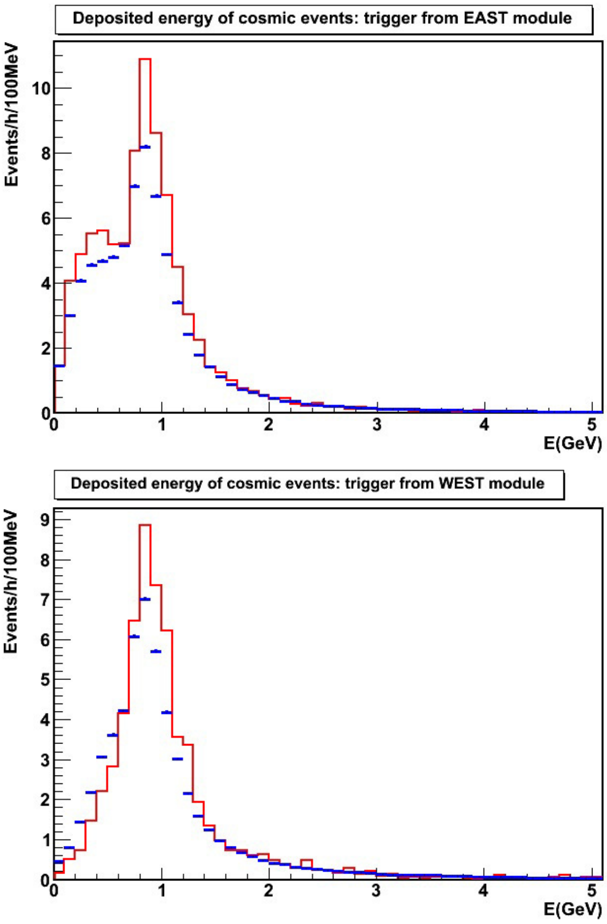

Figure 3.6: The results of the C.E.F. applied to a 2011data sample (blue dot) compared with the expectation from a dedicated Montecarlo simulation (red line) for the eastern module (upper) and the western module (bottom).

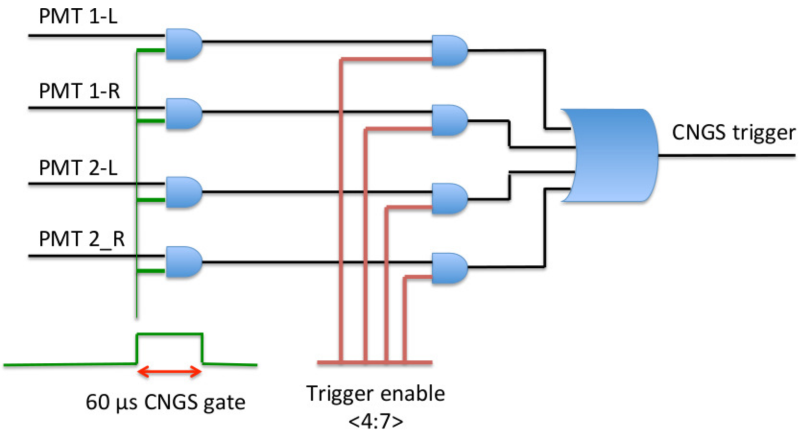

Figure 3.7: Schematics of the PMT trigger setup for CNGS events.

16th September, has been found to be 1,8%; this value is incredibly large if compared to the standard packet-loss commonly quoted for a UDP connection, which is typically below 10^{-4}. To investigate this anomalous behavior, a run per run analysis of the packet loss has been done (fig. 3.8). As evident from the trend, the packet loss affects only few runs, in which the connection is interrupted for defined amounts of time, and is reestablished after a time that varies from a few minutes to several hours.

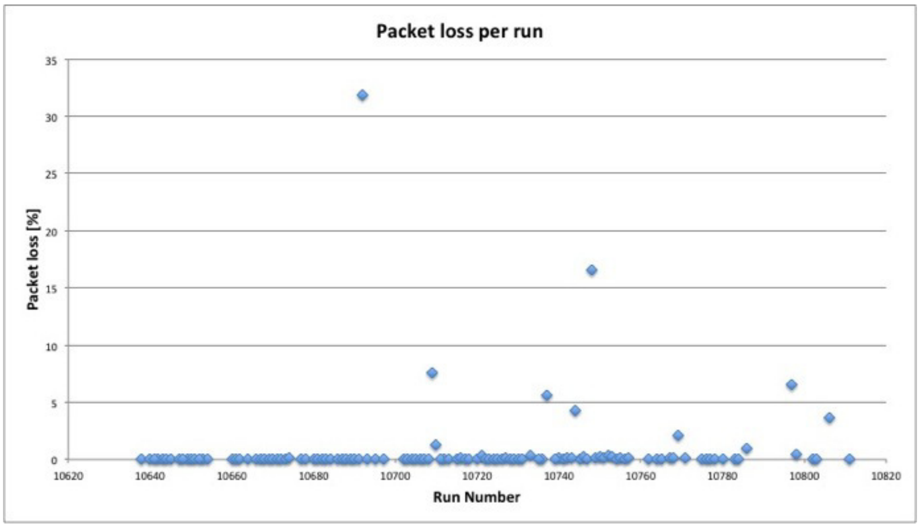

Figure 3.8: Trend of the Early Warning percentage packet loss during a subset of the 2011 CNGS data taking.

To have a clearer understanding of this phenomenon for the 2012 run a database has been created, and has been running from the 4th of May 2012 to the end of the CNGS run, on the 2nd December 2012, recording all the EW messages. The analysis of the 2012 packets (fig. 3.9) shows a mean value of the packet loss of 3,8%, significantly higher than the value found for the 2011 dataset. However, the behavior of the missed packet follows the one found for the 2011 analysis, showing some period in which the inefficiencies are concentrated. Since the program that receives the packets and keeps track of their contents has been changed form 2011 to 2012, without showing any improvement on the reliability of the setup, the packet loss is likely to be attributed to the connection from CERN to Gran Sasso laboratories, or to a failure on the CERN side.

Another aspect to be considered for what concerns the EW analysis is the precision of the time predicted for the extraction. This analysis has been made on the same 2011 period quoted above, comparing the time predicted and encoded in the EW packet, with the actual time of extraction, recorded into the CERN database (fig. 3.10). As evident from the plot, the bulk of the event remains within 20 μs from the mean value, while a small fraction (∼0,1%) of the packets has a predicted time that differs from the mean of about 120 μs.

The same analysis has been performed with 2012 data, showing a similar distribution, and a fraction of 0,1% of events which differs from the bulk of ∼120 μs (fig. 3.11).

While the bulk of the distribution remains inside the CNGS-gate (indicated in fig.3.10 and fig.3.11 by two green vertical lines), the tail at 120 μs escapes the 60 μs

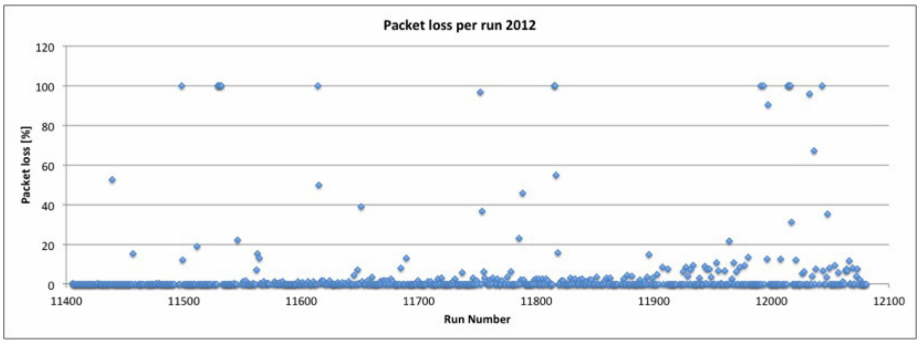

Figure 3.9: Trend of the Early Warning percentage packet loss during a subset of the 2012 CNGS data taking.

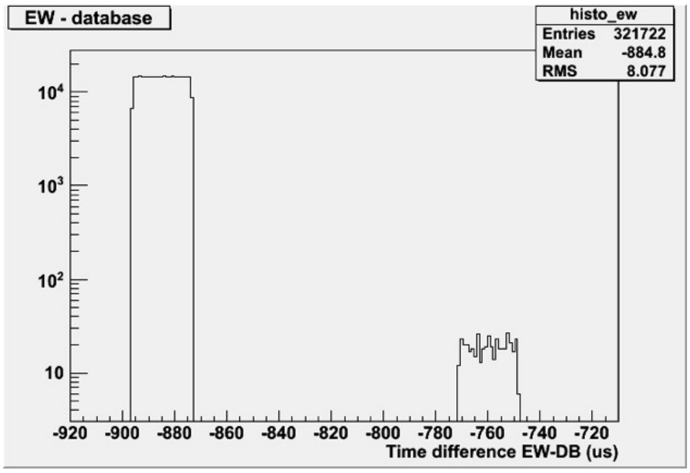

Figure 3.10: Time difference (in μs) of the time predicted and sent through the Early Warning packets, and the actual time of extraction for the 2011 data set. The green lines represent the CNGS-gate interval.

gate. In this case, as in the case packet loss, any eventual neutrino interaction would not be tagged as CNGS event, but may still be triggered with the atmospheric trigger, i.e. the coincidence of the PMT signals from two adjacent chambers. For this reason, a dedicated scan of all 2011 and 2012 atmospheric events has been done, checking if the time of interaction is compatible with the time of any extraction recorded at CERN. The events recovered with this “off-line tag” are affected both by the same dead time of the atmospheric PMT trigger , with an average value of 3.9% for the 2011 data taking and 5.1%for the 2012. Moreover, to have the overall inefficiency due to the EW packet loss these results must be corrected by the different efficiency of the two trigger requirements (single threshold vs. coincidence of adjacent modules). To have an estimate of the efficiency of the atmospheric trigger with respect to the CNGS trigger a set of 1022 CNGS neutrinos and 3474 muons from neutrino interactions in the surrounding rock have been analyzed,resulting in a total of 17 neutrinos and 286 “rock-muons” that have been triggered only by a single threshold, and not with the coincidence. This analysis shows an efficiency of the atmospheric trigger of 98% for the neutrinos and 91% for the “rock-muons” (tab.3.2.2). The 17 neutrino events triggered only by the single threshold were 5 ν_μ CC, 5 NC and 7 to be defined. Their energy spectrum is given in fig.3.12.

After this recovery, considering also the different trigger efficiency and detector

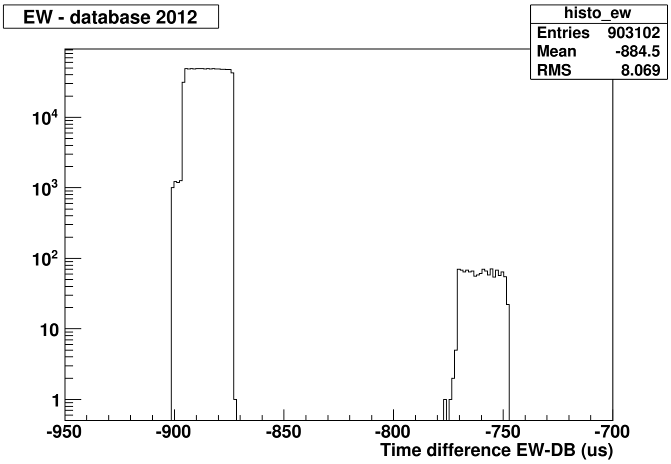

Figure 3.11: Time difference (in μs) of the time predicted and sent through the Early Warning packets, and the actual time of extraction for the 2012 data set. The green lines represent the CNGS-gate interval.

Event type	Single threshold	Coincidence	Atm. trigger eff. [%]
ν interactions	1020	1003	98%
Rock μ	3474	3188	91%

Table 3.2: Comparison of the number of events acquired requiring a single PMT threshold, w.r.t. the coincidence of the PMT signals on adjacent chambers

live time for CNGS and atmospheric, the CNGS inefficiency due to the lack of synchronization results to be negligible ($\leq 10^{-4}$).

The second key element of the synchronization is the time link between external and underground laboratory at the Gran Sasso site. The link is based on a master clock module(ESAT 2000), placed in the “router room” of external labs, which connects to a GPS receiver, and to a rubidium oscillator ensuring clock stability. The time information is sent to the underground experimental hall via ~8 km of single-mode optical fiber. The signal is composed by a precise 1kHz edge, which is used to lock the clock in the underground site, followed by a stream of 64 bits in which the time tag corresponding to the rising edge, is encoded (fig. 3.13).

An FPGA board, running at 40 MHz, reads and decodes the data stream, and resets a local counter at each rising edge of the kHz signal. The value of the local counter is added to the stream tag to produce two 32 bit words, one containing the time epoch in seconds, as defined by the UNIX standard, the other containing the fraction of second,

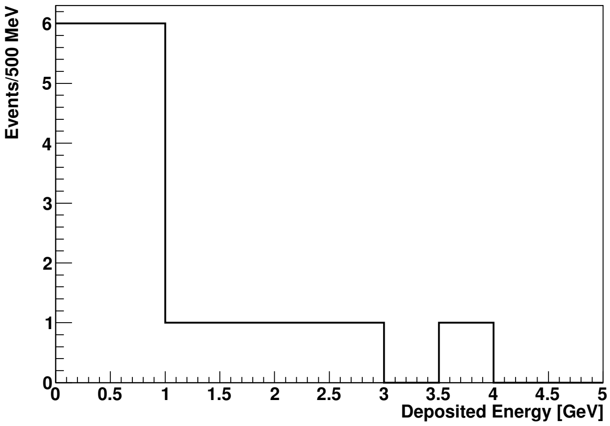

Figure 3.12: Energy distribution of the events triggered only with a single PMT signal, which wouldn’t have been triggered by the atmospheric trigger (coincidence of the two threshold)

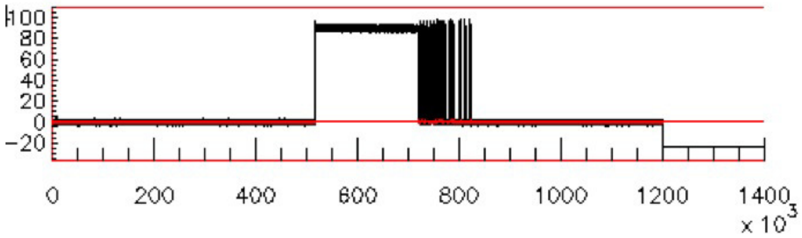

Figure 3.13: Example of the synchronization signal sent from the external to the underground laboratories. The first leading edge carries the precise timing information for clock re-synchronization, while the following bit pattern encodes the timestamp.

with a resolution of 25 ns. The stability of the local counter, based on the FPGA clock, has been monitored to check for any drift in time. At every resynchronization with the kHz edge the value of the counter is stored and compared with the expected value. The difference between the expected value and the recorded value reaches a maximum of 1 clock cycle, i.e. 25 ns, after every resynchronization, reflecting a $\sim 10^{-5}$ difference of the FPGA clock from a precise 40MHz oscillator locked with the kHz signal. This frequency difference turns out to be completely negligible when considering the opening of the CNGS-gate, since the 60 μs width of the gate greatly include any clock-related jitter.

The delay associated with the transit from the "router room", to the top of the ICARUS detector, in hall B of underground laboratory, has been measured via a two-way time difference with a LeCroy WavePro 735Zi digital scope (40 Gs/s, 3.5 GHz bandwidth). For this procedure, a second spare optical fiber, connecting the same two end points, has been set. For the first measurement the two fibers have been connected together in the underground hall, and the sum of the delay on two paths have been measured in the external "router room". A second measurement have been done by using a common signal as input to to both the fibers in the "router room", and measuring the difference between the delays on the two paths underground. This procedure has been repeated few times in different periods, to check the stability of the delay. All the measurements have been found to be in good agreement, giving a mean value of $42036,6 \pm 1,3 ns$ [30].

3.3 Trigger manager

A dedicated device has been installed in order to handle the different trigger sources, monitoring the trigger rates and the synchronization, and finally communicating all the relevant information to the acquisition system. The commercial National Instrument PXI system has been chosen to implement these features; it consists on a Real Time (RT) controller (PXIe-8130) for Trigger-DAQ (T-DAQ) communication, and an FPGA board (PXI-7813R), for signal handling.

The code running on the FPGA, which has been developed with the virtual instrument (vi) graphical programming language, implements the time critical processes, like the synchronization with the LNGS time-link, the opening of CNGS-gate and the time stamping of each trigger. It also keeps record of the trigger source, i.e. the first signal that triggered the acquisition of an event, and the trigger mask, i.e. the trigger pattern during the 1 ms drift period. The trigger frequency of each source is also calculated continuously, for controlling the stability of the system.

The RT controller instead implements all the features that foresee a communication with external devices, such as the DAQ process or the EW reception. The CNGS relates UDP packets for time synchronization are forwarded from a computer that has a public IP address directly to the RT controller, which is on the private ICARUS network. As soon as a packet is received, the controller check if it is of CNGS-EW type and in this case it warns the FPGA of the forthcoming extraction. For what concerns the T-DAQ communication, a handshake between the DAQ main process and the trigger manager has been developed. It is based on the exchange of Ethernet UDP packets; since this kind of Ethernet communication is not reliable the reception of each packet must be confirmed to the sender, handshaking each message.

The T-DAQ process is divided into 3 periods. In the initialization phase the DAQ sets the trigger parameter, enabling the relevant trigger sources, communicate the run number to the RT controller and declares the number of buffers available on the digital boards for the run.

The second phase is the running phase. As a trigger is recognized, a hardware signal is sent to the digital board to store the waveform in the local buffer, and a software message is sent to the DAQ to start the acquisition process. After the acquisition of the event the buffers on the digital boards are released, and the trigger manager is informed of this action. The RT controller thus monitors continuously the number of buffers available, and prevents the generation of new triggers in case that all the 8 buffers are full. To further improve the system efficiency for CNGS events, a multi level veto has been developed.

This new systems uses the first 5 acquisition buffers to record evens from any trigger source. If more than 5 buffers are occupied at the same time, a situation that occurs when the trigger rate is temporarily higher than the DAQ building rate, any trigger outside the CNGS gate is disabled. When also the next 2 buffers are occupied, and only one buffer remains free, the only trigger enabled is the PMT signal from any chamber in coincidence with the CNGS beam. The multi level veto system, introduced with the 2011 CNGS run, has permitted to have an almost dead-time free data acquisition for CNGS events triggered by PMT.

In final phase of the T-DAQ communication all trigger sources are disabled and the system is reset to its initial state.

In order to monitor the detector activity, i.e. trigger frequency, dead time and DAQ building time, a dedicated database has been introduced. The database records, for each event the trigger source and mask, the timestamp, the CNGS tag and other information regarding the status of the acquisition, such as the number of occupied buffer. An automated script queries the database and display the results in a public web page, which can be accessed anywhere. This became a handy tool to monitor the state of the run, visualizing any anomalous behavior, and preventing the run from remaining stuck for a long time when some problem occurs (fig. 3.14).

3.4 Data taking with PMT trigger

Since October 2010 the detector has been running in steady condition, acquiring data with the atmospheric PMT trigger, defined as coincidence of the two PMT signal on adjacent chambers, and with the trigger dedicated to CNGS events, defined as the PMT signal of a single chamber in coincidence with the 60 μs width CNGS-gate. A detailed analysis of the dead time, and the number of active crates, which defines the active volume, must be considered in order to define a correct value of exposure on both kinds of events.

For what concerns the 2010 data taking with the CNGS trigger, the first issue to

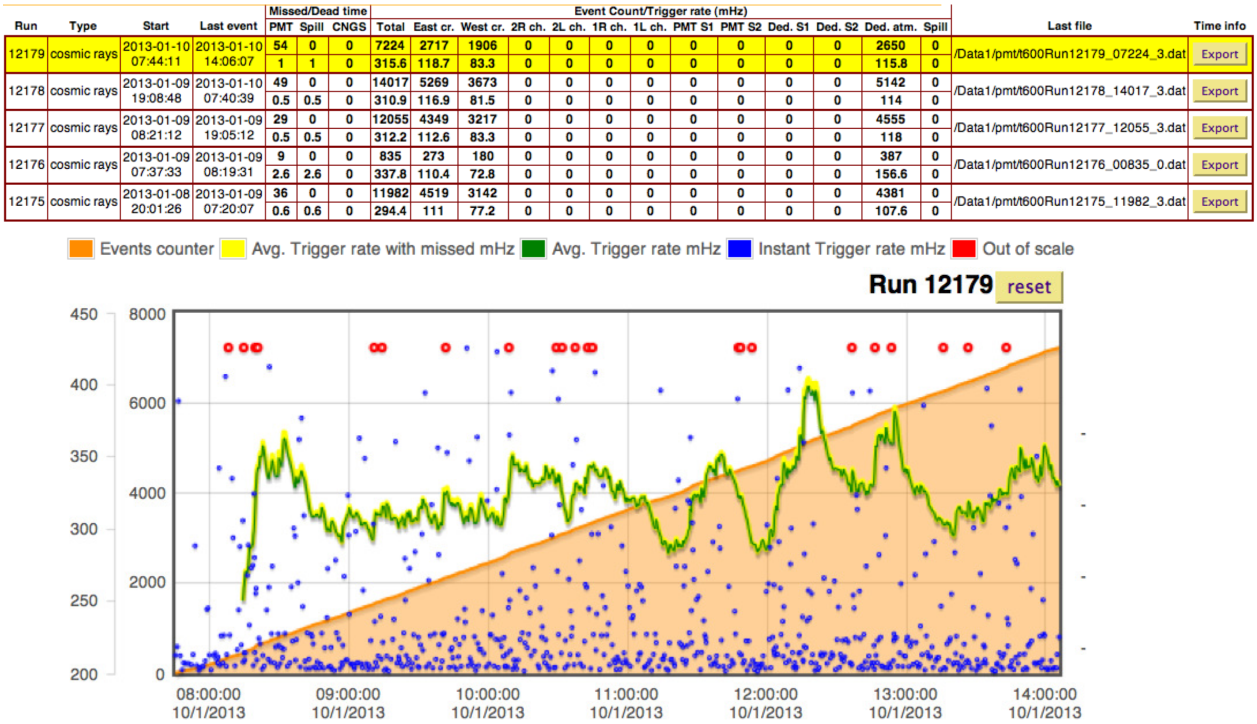

				Missed/Dead time			Event Count/Trigger rate (mHz)														
Run	Type	Start	Last event	PMT	Spill	CNGS	Total	East cr.	West cr.	2R ch.	2L ch.	1R ch.	1L ch.	PMT S1	PMT S2	Ded. S1	Ded. S2	Ded. atm.	Spill	Last file	Time info
12179	cosmic rays	2013-01-10 07:44:11	2013-01-10 14:06:07	54	0	0	7224	2717	1906	0	0	0	0	0	0	0	0	2650	0	/Data1/pmt/t600Run12179_07224_3.dat	Export
				1	1	0	315.6	118.7	83.3	0	0	0	0	0	0	0	0	115.8	0		
12178	cosmic rays	2013-01-09 19:08:48	2013-01-10 07:40:39	49	0	0	14017	5269	3673	0	0	0	0	0	0	0	0	5142	0	/Data1/pmt/t600Run12178_14017_3.dat	Export
				0.5	0.5	0	310.9	116.9	81.5	0	0	0	0	0	0	0	0	114	0		
12177	cosmic rays	2013-01-09 08:21:12	2013-01-09 19:05:12	29	0	0	12055	4349	3217	0	0	0	0	0	0	0	0	4555	0	/Data1/pmt/t600Run12177_12055_3.dat	Export
				0.5	0.5	0	312.2	112.6	83.3	0	0	0	0	0	0	0	0	118	0		
12176	cosmic rays	2013-01-09 07:37:33	2013-01-09 08:19:31	9	0	0	835	273	180	0	0	0	0	0	0	0	0	387	0	/Data1/pmt/t600Run12176_00835_0.dat	Export
				2.6	2.6	0	337.8	110.4	72.8	0	0	0	0	0	0	0	0	156.6	0		
12175	cosmic rays	2013-01-08 20:01:26	2013-01-09 07:20:07	36	0	0	11982	4519	3142	0	0	0	0	0	0	0	0	4381	0	/Data1/pmt/t600Run12175_11982_3.dat	Export
				0.6	0.6	0	294.4	111	77.2	0	0	0	0	0	0	0	0	107.6	0		

Figure 3.14: Example of the display of the Icarus trigger web-page. The list of the runs acquired (top) is shown together with the main DAQ information, such as dead time and lost triggers. An example of the trend of the rate of the primary trigger (yellow line), the rate of acquired events (green line) and of the integral number of acquired events (orange box) is also shown (bottom).

be considered is the acquisition dead time. During the first days of data taking (from October 1st to October 27th) the T-DAQ communication was not yet implemented. For this reason, to avoid any misalignment between the event numbering of the trigger system and the one given by the DAQ, which appears when a trigger is given to the detector while the DAQ is still busy, a fixed automatic veto of 3 s has been set after every trigger, inhibiting the generation of new triggers. This first running phase, which has been done with the MEB feature enables, has shown a dead time of 11%, measured as the percentage of the CNGS trigger requests that have not been fulfilled due to the fixed veto.

During second period of the 2010 CNGS run, from October 27th to the end of the 2010 run on November 22nd, the T-DAQ handshake has been running steadily, without the necessity of any fixed veto after the triggers. As a precaution, and to check the correct operation of the new setup, the MEB feature has been disabled during this running, forcing the trigger to wait for the complete acquisition of one event before re-arming the trigger for the next event. For this reason the dead time during this period raised to 20%.

The performance of the detector has been definitively improved for the 2011 and 2012 run with the adoption of the the multi level veto structure, which guaranteed that an acquisition buffer on the digital board has been always free for recording any CNGS trigger. The only dead time associated with these events is produced by an automatic veto set during the reset procedure of the FPGA state machine, which occurs after every trigger and lasts $\sim 2ms$ .To check the consistency of the effects of the automatic veto, the total number of CNGS trigger missed has been compared with the total number of CNGS triggers, resulting in a mean fraction of CNGS events missed of 0,1%. This value is consistent with the mean trigger rate, which is $\sim$ 200 mHz.

The detector live-time for the CNGS data taking has been monitored since the first CNGS run after the commissioning phase, from October 1^{st}. The overall mean uptime for the three years of data taking has been measured as the time elapsed from the first to the last event acquired run by run, dividing for the time elapsed between the first event of the first run, to the last event of the last run. The values obtained has been 88.8% for the 2010 run[1], 89.6% for the 2011 and 88.1% for the 2012. To have a better estimate of the fraction of p.o.t. lost when the run were not active a second analysis has been done, integrating all the p.o.t. collected from the first to the last event of each run, and dividing the result for the p.o.t. delivered between the last event and the last event of the previous run. The percentage value of p.o.t. recorded, when the dead time is taken into account, has been 65% for the 2010 data taking, 93% for the 2011 and 93% for the 2012 (fig.3.15). The average CNGS trigger rate for the period going from October 27^{th} to November 22^{nd} 2010, and for the whole 2011 and 2012 periods has been 0,3 mHz, 1,7mHz and 2,9mHz respectively. The fluctuation of the trigger rate reflects the different intensities of the CNGS beams, as well as a different percentage of empty events, related with the PMT trigger upgrade.

A completely different situation regards the atmospheric triggers, for which, after the introduction of the multi level veto, the number of buffers available is reduced to 5, and which has a trigger rate almost two orders of magnitude higher than the one for CNGS events. This two factors contribute to raise the acquisition dead time, which

---

[1] From October 27^{th} to November 22^{nd}

Data taking	First run	Last run	Start	End
2010	9751	9962	October 1st	November 22nd
2011	10216	10987	Mach 19th	November 15th
2012	11237	12084	March 23rd	December 3rd

Table 3.3: Summary of the three CNGS running periods.

Data taking	Dead time [%]	Mean uptime [%]	p.o.t del. $\times10^{19}$	p.o.t. coll. $\times10^{19}$	# CNGS triggers	CNGS trigger rate [mHz]
2010	15.5	88.8*	0.80	0.59	628*	0.3*
2011	0.3	89.6	4.78	4.45	31482	1.7
2012	<0.1	88.1	3.83	3.58	57351	2.9

Table 3.4: Summary of the data taking performances for the three years of CNGS run. *For the 2010 run the mean uptime, the number of triggers and the mean trigger rate have been obtained for the period going from October 27th to November 22nd

must be accurately measured to give the effective exposure of the atmospheric trigger. The analysis must be divided in two periods, For these events a similar analysis has been carried out, monitoring the uptime and the average dead time.

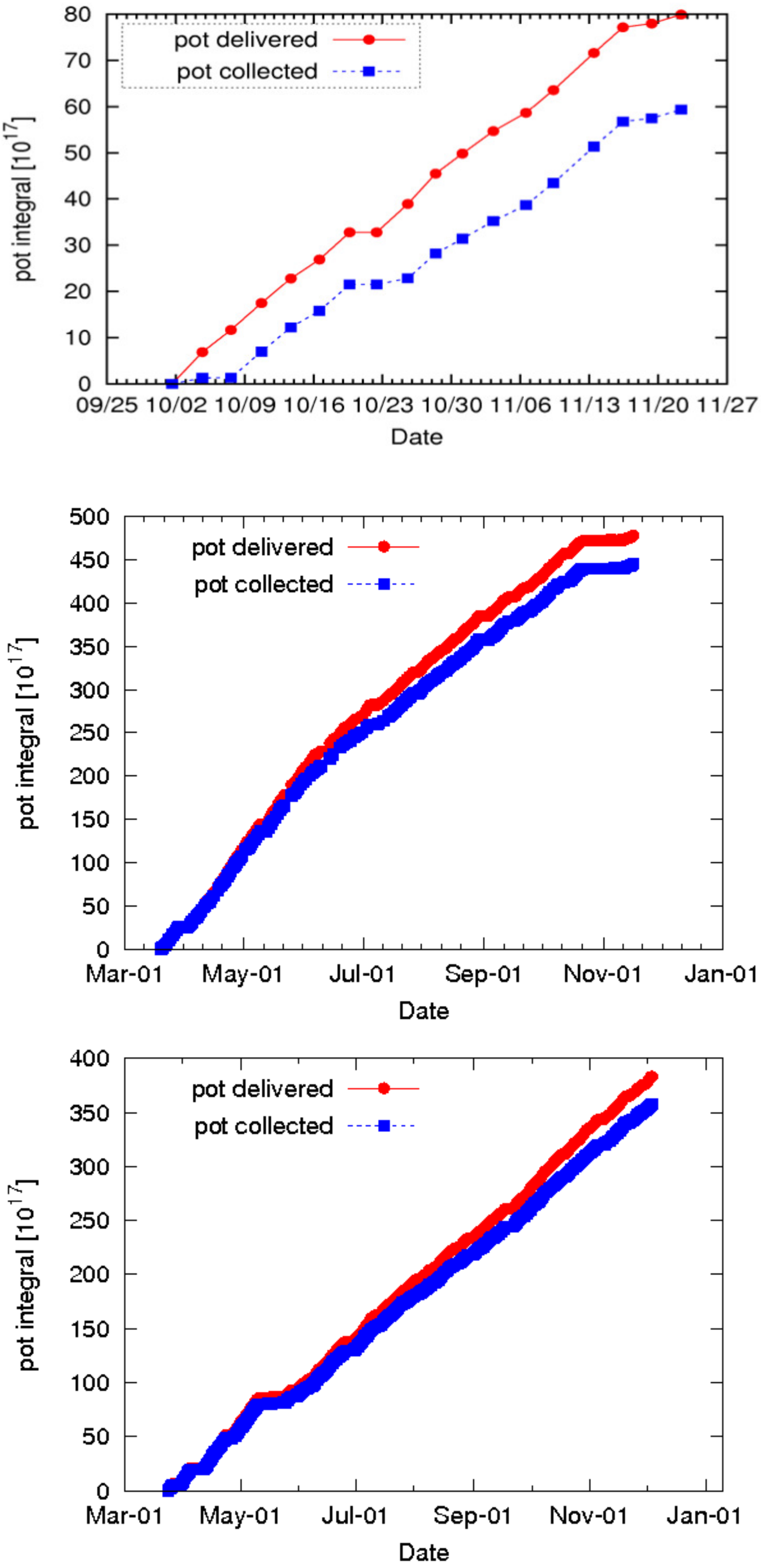

Figure 3.15: Integral proton on target statistic delivered to CNGS (red) and recorded by ICARUS T600 (blue) during the 2010 (top), 2011 (middle) and 2012 (bottom) data taking

Chapter 4

Triggering on the charge signal: the DR-slw algorithm

One of the most unique features of LAr TPC when compared with bubble chambers, which show similar characteristics such as spatial resolution, density and specific energy loss, is that the signal itself can provide a trigger to the whole system. This feature appears particularly appealing when considering the energy tail of the atmospheric neutrino spectrum below ∼1 GeV, which is the same energy region in which the proton decay searches are addressed. As it has been shown in ch.3 the trigger setup based on PMTs begins to be inefficient at these energy, since their spatial inhomogeneity start affecting the distribution of the events acquired. To increase the effective exposure of the ICARUS T600 detector in this energy region, and to overcome the PMT inhomogeneity, a second trigger that exploits the charge signal collected on wires has been developed and implemented, both in a software and hardware layout. In this new setup any charge deposition detected on the wires can be used to trigger the acquisition of an event, while the PMT waveforms are recorded in any case to extract a posteriori the information regarding the time of interaction of the event, which may be correlated to any PMT activity below threshold.

4.1 Description of the algorithm

The analysis carried out on data from the technical run held in Pavia in 2001, has shown a peculiar noise pattern on the wire signal, which is the sum of a low frequency and a high frequency noise component (fig. 4.1). The low frequency component, which behaves as a baseline oscillation, is due to the mechanical movement of each wire w.r.t. the other wire planes. The amplitude of this oscillation is ∼ 10 ADC counts, thus preventing the use of a fixed threshold for hit detection. The high frequency noise has a period of few t-samples, and amplitude of ±2 ADC counts.

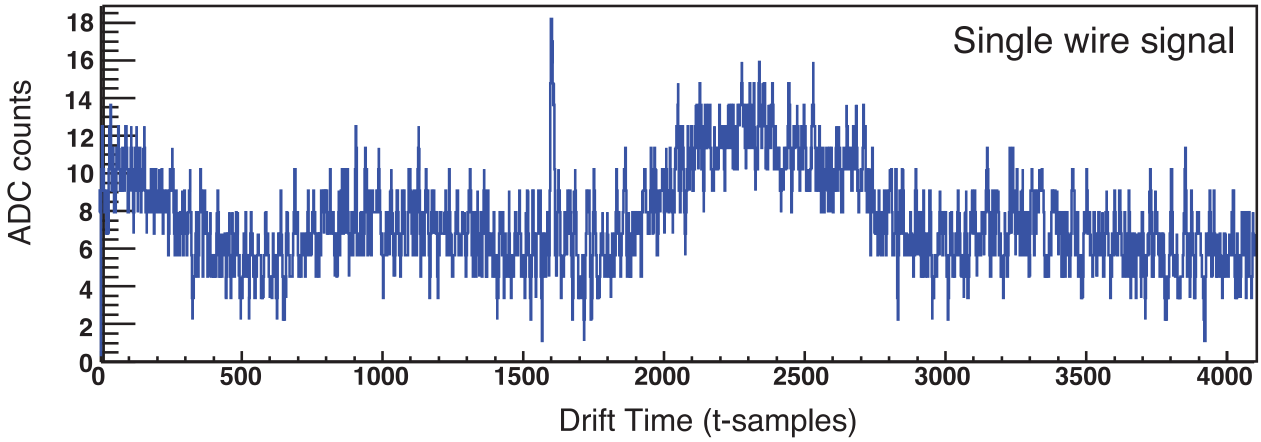

Figure 4.1: Typical wire signal collected during the 2001 data-taking

In order to filter out the two components of the electronic noise, a novel filter, named Double Rebinning sliding windows, DR-slw, has been developed [31], [32] It is based on a double running average, performed on 128 (long bin) and 8 (short bin) t-samples.

$$Q_{short}(t_j) = \sum_{i=j-7}^{j} Q(t_i)/8 \tag{4.1a}$$

$$Q_{long}(t_j) = \sum_{i=j-127}^{j} Q(t_i)/128 \tag{4.1b}$$

$$S(t) = Q_{short}(t) - Q_{long}(t) \geq Q_{thr} \tag{4.1c}$$

As shown in fig. 4.2 the long bin follows the baseline, without being perturbed by the hit signal, while the short bin attenuates the high frequency noise, without lowering the signal, whose duration is longer than the integration period, typically 30 t-samples for a m.i.p. parallel to the wires. By subtracting the long bin from the short bin a clear signal emerges, and a fixed threshold can be now applied for hit detection: if the signal stays above a fixed threshold for at least 3 consecutive samples a peak signal is generated. This filtering technique has proven to be very effective, resulting

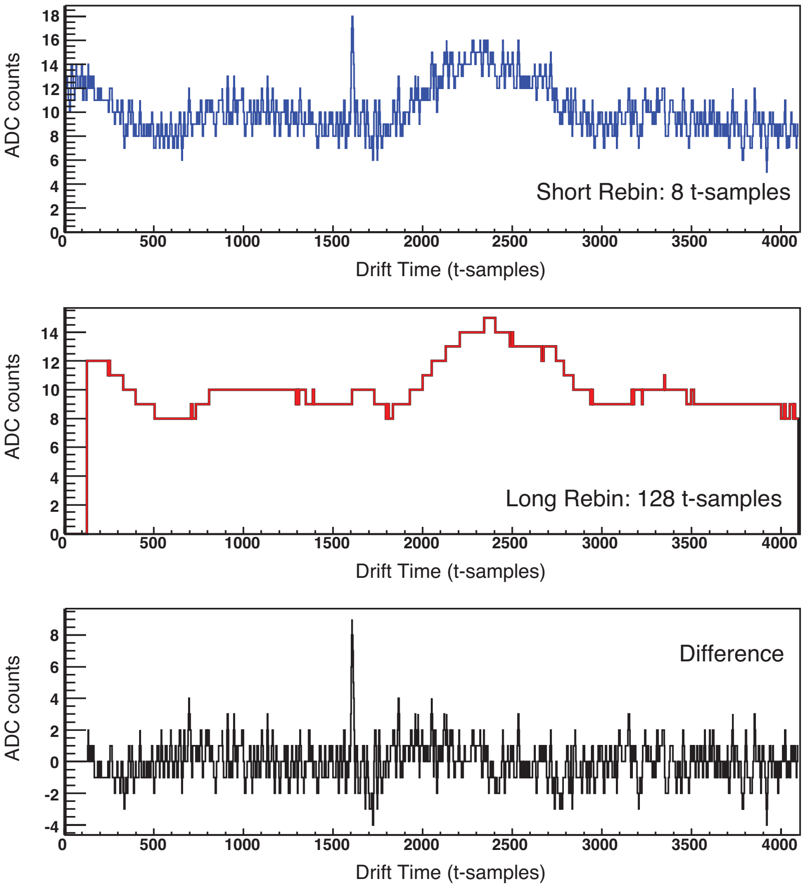

Figure 4.2: The short bin (upper) reduces the high frequency, while the long bin (middle) follows the baseline oscillation. Their difference (bottom) results in a clear signal to which a single threshold can be applied

in an efficiency exceeding 99% with a background misidentification of 10^{-3} on single hit detection on the Pavia data sample (fig. 4.3).

To extract a trigger from the peak signals a majority stage has been included after the DR-slw filter. In view of a hardware implementation, and for isolating the noisy or problematic boards, the same read-out modularity of 32 wires has been chosen for implementing the majority stage. To keep a high efficiency also on the smaller tracks, and to comply with the digital board modularity, each set of 32 wires has been further divided into two subsets. In the complete algorithm, if the number of peaks contemporary active on 16 consecutive wires exceeds a determinate value a trigger signal is output. The two triggers generated this way, named Left and Right Trigger Out, LTO and RTO respectively, are merged together to produce a Global Trigger Out (GTO) signal for each digital board, defined as the logical OR of LTO and RTO signals.

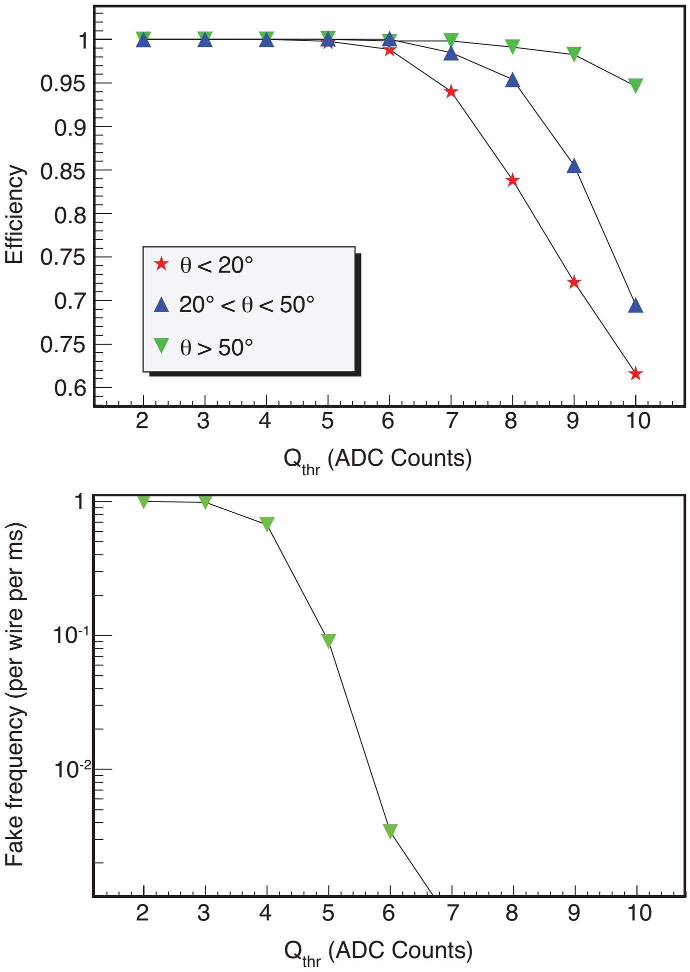

Figure 4.3: Hit identification efficiency for three different track inclination (top) and fake frequency per wire and ms drift time (bottom) of the DR-slw algorithm (software) as a function of the discrimination threshold in data collected in Pavia with a semi-module of T600.

A variable stretching, ranging from $25\mu s$ to $125\mu s$, is also foreseen for the peak signal, preventing any loss of efficiency correlated to the non-synchronization of the peaks signals in case of inclined tracks.

After the introduction of the majority stage, the complete algorithm has been tested on a set of crossing muons acquired with the 2001 test run, confirming the performances reached with the single wire analysis.

4.2 A software implementation of the DR-slw algorithm for CNGS events

4.2.1 A two level trigger based on DR-slw

In 2011 a new trigger for CNGS events, alternative to the PMT trigger in coincidence with the CNGS-gate, and based on the DR-slw has been studied and developed to check the efficiency of the PMT trigger and to prevent any possible failure of the PMT system. The new system is structured in two levels of trigger. The first level is based on the time coincidence with the CNGS beam. If no activity is recorded from the PMT system, the CNGS-gate signal is used as a primary trigger, acquiring a full drift volume after the time predicted for the neutrino interaction. In the second level, a software script analyzes the event thus acquired with the DR-slw algorithm. The software analyzes only the Collection view, where the signal to noise ratio is more favorable, searching for any charge deposition. The algorithm and has been tested both on 2010 real data and on MC events, to get an estimate of the efficiency for any class of events.

It is worth noting that the primary trigger rate is given by the SPS extraction period, which delivers up to two extractions every 6 seconds, resulting in a primary trigger rate of 0,3 Hz at maximum intensity. The software filter must not only be fast enough to analyze the incoming data at the primary trigger frequency, but must keep the misidentification of empty events below 10^{-3} in order to reduce the huge amount of events ($\sim$ 25’000 events/day) which are collected every day to a small number of events to be recorded for a further analysis.

For what concerns the test on real data, the dataset consists of 109 neutrino interactions, classified after a visual scanning as 78 ν_μ CC, 18 ν NC and 13 ν X interactions to be studied, and 389 muons coming from a neutrino interaction in the rock. These events are the result of a visual scanning of all the 2010 events tagged with CNGS-gate. For each event the maximum number of GTO, chamber by chamber, was studied, varying the threshold for peak identification and the majority level. The peak stretching was fixed to the minimum value of 25 μs, since the CNGS events are expected to be close to horizontal.

Results are shown in fig. 4.4 for a threshold of 7 ADC counts for single hit detection, and requiring a majority of 12 over 16 peak signals. The columns show, for each interaction type, the number of events that would have been lost requiring a certain number of GTO. All neutrino interaction events are selected by requiring at least 9 GTO, corresponding to an event occupation of 86 cm in Collection view. Similarly all muons coming from neutrino interaction with the rock are recorded with a threshold of 8 GTO.

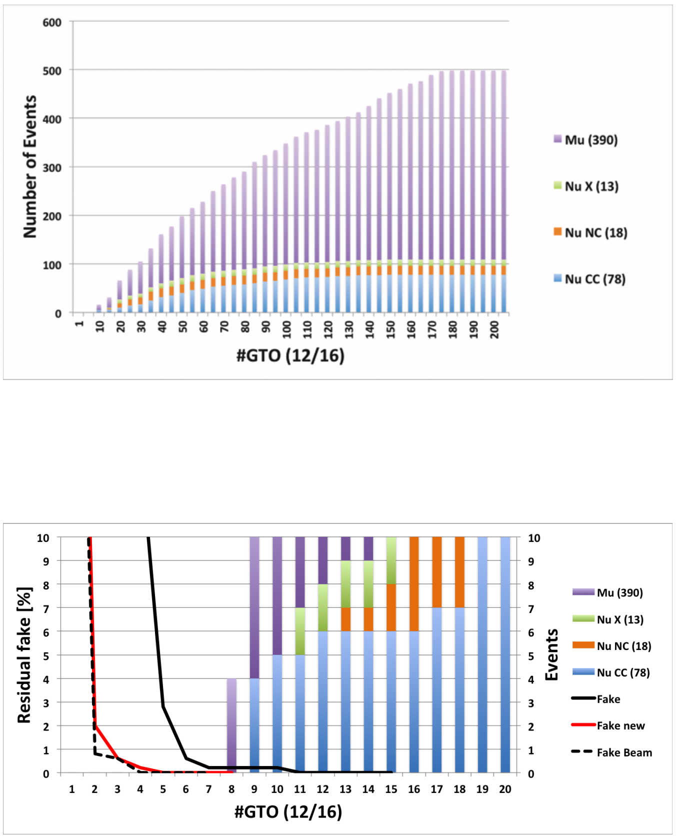

Figure 4.4: Results of the DR-slw algorithm applied to the 2010 dataset. The upper distribution show the number of events that would have been lost as a function of the maximum number of GTO required. A close up of the distribution is compare with the fraction of empty events misidentified (bottom).

A parallel analysis, with the same filtering parameters, has been performed on empty events, acquired with random periodic triggers in three periods, with different running condition, both during 2010 and 2011 run. These sets of events have been used to qualify the algorithm on the current noise condition, and represent an ideal dataset free from any bias correlated to the PMT activity. The results of this analysis are shown in fig. 4.4 bottom, on the left, where the number of fake is plotted as a function of the number of GTO required for a trigger. The solid black line represents the fraction of empty events misidentified as good in the run with random triggers acquired in 2010. It is possible to notice the reduction of noise level w.r.t. the two 2011 datasets, where the red line represent the set of data acquired just before the beam start, in February 2011, and the dotted line represent the set of data taken in March when the CNGS beam was active. This reduction in fake detection is due to an important campaign of electronic upgrade and maintenance held from December 2010 to January 2011 with the aim of reducing the noise level. After this intervention a requirement of at least 5 GTO signals firing in the same chamber results to be enough to reduce the noise to a negligible level (i.e. below 10^{-3}). With this set of parameters, which resulted to be the most favorable, it is possible to achieve a rejection factor of the order of 10^3 on empty events, while keeping full efficiency on the whole dataset. It is worth noticing that the GTO threshold can ranges over few values, while remaining fully efficient on the dataset and maintaining a good empty rejection. This fact is important in view of a possible degradation of the noise, which may occur during the data taking.

To confirm the results obtained on the 2010 data sample, the DR-slw filter has been run over a set of Monte Carlo events, generated with the FLUKA package [33]. This software simulates the propagation and the interactions of the primary particle through the medium, recording all the information about secondary particles emitted, the deposited energy per chamber, and the attenuation due to the electron-ion recombination (quenching). The complete sample is composed by 10’000 ν_eCC interactions, 10’000 ν_μNC interactions, and 1’000 ν_μCC interactions, whose spectrum and direction reproduce the ones foreseen for the CNGS beam at the Gran Sasso site.

The analysis has been focused on the events that are contained inside a “scanning fiducial volume”, which has been defined for the first phase of the visual scanning to exclude all the events too close to the detector’s wall to be identified. The cut introduced at this level represents a minimum reduction of the fiducial volume of the primary interaction vertex, outside which it is extremely difficult to distinguish a muon or an electron track form other particles. To take into account the beam direction a cut of 1,5 cm has been applied to each side of the drift chamber along the drift direction and along the vertical direction, while along the beam direction the cut has been set to 5 cm upstream and 14 cm downstream.

After applying the cut on the vertex position, each event has been processed with the DR-slw filter, searching for the maximum number of GTO on the four collection views. The analysis has been repeated varying the threshold for peak detection from 6 to 8 ADC counts, and for a majority level ranging from 10 to 14 over 16 consecutive wires. A second requirement has been introduced on the maximum number of GTO found per chamber, ranging from 1 to 6.

In fig. 4.5 it is shown the distortion to the ν_eCC deposited energy (solid black line) obtained applying the DR-slw filter with a threshold of 7 ADC counts for the hit detection and a majority of 12 wires over 16, requiring at least 1 GTO (blue line) and 6 GTO (red line) per chamber.The neutrino energy spectrum is also shown in dashed black line. The spectral distribution shows how the inefficiencies are concentrated on the low energy tail of the spectrum, while the portion of the spectrum above 1GeV remains unperturbed. A more complete overview of the overall efficiency as a function of the majority level and of the maximum number of GTO required per chamber is reported in tab. 4.1.

The same analysis has been performed on ν_μNC (fig. 4.6, tab. 4.2) showing an higher degradation of the efficiency w.r.t. the ν_eCC data sample. This is mainly a consequence of the NC energy spectrum, which is peaked at lower energies, where the filter is less efficient.

Finally the results for the same analysis applied to ν_μCC events are shown in fig. 4.7, tab. 4.3. Here, thanks to the longitudinal evolution of the event, due to the presence of long muon tracks, the efficiency increase w.r.t. the case of the NC interaction, even if the neutrino energy spectrum is identical at first approximation.

The efficiency of the DR-slw applied to the MC dataset shows an almost full efficiency for a single GTO requirement, an produces an almost unbiased spectrum in the case of CC interactions for $E_{dep} > 500$ MeV, also for the requirement of 5 GTO contemporarily active on the same chamber. On the basis of these encouraging results the filter has been chosen both as an additional trigger for the CNGS events, parallel to the PMT that remains active as the principal trigger, and for an off-line event selection, as described in the following paragraphs.

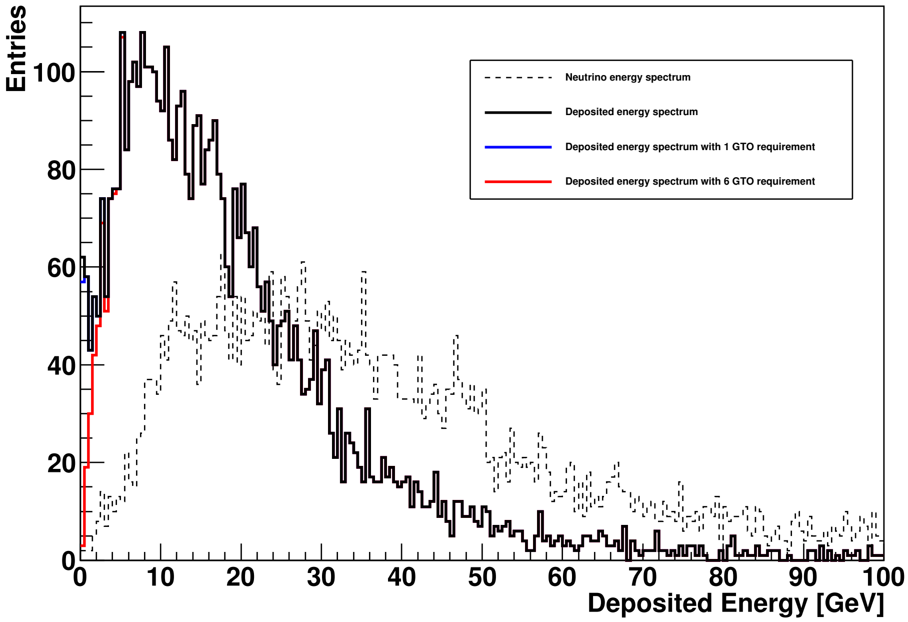

Figure 4.5: Neutrino energy spectrum of the ν_eCC Montecarlo sample (dashed line). The distortion of the deposited energy spectrum (in black) is shown for two values of GTO required per chamber GTO≥1 (blue line) and GTO≥6 (red line)

Threshold=6							
	GTO > 0	GTO > 1	GTO >2	GTO > 3	GTO > 4	GTO > 5	GTO > 6
maj=10	99.9	99.7	99.2	98.9	98.3	97.7	97.1
maj=12	99.9	99.6	99.1	98.7	98.1	97.5	96.8
maj=14	99.8	99.5	98.9	98.5	97.9	97.2	96.5

Threshold=7							
	GTO > 0	GTO > 1	GTO >2	GTO > 3	GTO > 4	GTO > 5	GTO > 6
maj=10	99.9	99.7	99.2	98.9	98.3	97.6	97.0
maj=12	99.9	99.6	99.1	98.7	98.1	97.4	96.7
maj=14	99.8	99.4	98.9	98.4	97.7	97.2	96.3

Threshold=8							
	GTO > 0	GTO > 1	GTO >2	GTO > 3	GTO > 4	GTO > 5	GTO > 6
maj=10	99.9	99.6	99.2	98.8	98.3	97.5	96.8
maj=12	99.9	99.5	99.0	98.6	98.0	97.2	96.6
maj=14	99.7	99.3	98.8	98.3	97.6	97.0	96.1

Table 4.1: Percentage efficiency of the DR-slw filter on ν_eCC events as a function of the threshold, majority level and number of GTO required per chamber

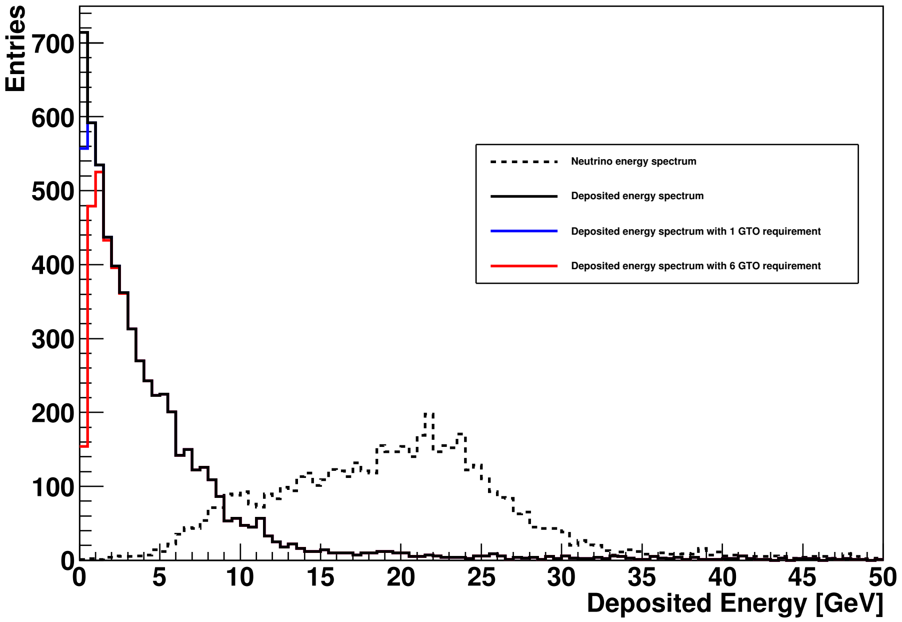

Figure 4.6: Neutrino energy spectrum of the ν_μNC Montecarlo sample (dashed line). The distortion of the deposited energy spectrum (in black) is shown for two values of GTO required per chamber GTO≥1 (blue line) and GTO≥6 (red line)

Threshold=6							
	GTO > 0	GTO > 1	GTO >2	GTO > 3	GTO > 4	GTO > 5	GTO > 6
maj=10	97.7	96.5	94.8	93.1	91.3	89.5	87.4
maj=12	97.4	96.0	94.5	92.5	90.7	88.7	86.5
maj=14	97.2	95.6	93.7	92.0	89.6	87.6	85.5

Threshold=7							
	GTO > 0	GTO > 1	GTO >2	GTO > 3	GTO > 4	GTO > 5	GTO > 6
maj=10	97.7	96.5	94.8	93.0	91.2	88.9	86.7
maj=12	97.4	96.0	94.4	92.4	90.5	87.6	85.2
maj=14	97.2	95.5	93.5	91.4	89.1	85.7	82.8

Threshold=8							
	GTO > 0	GTO > 1	GTO >2	GTO > 3	GTO > 4	GTO > 5	GTO > 6
maj=10	97.6	96.4	94.7	92.8	91.0	88.9	96.7
maj=12	97.3	95.9	94.2	91.8	89.8	87.6	95.2
maj=14	97.1	95.2	92.9	90.5	88.0	85.7	92.8

Table 4.2: Percentage efficiency of the DR-slw filter on ν_μNC events as a function of the threshold, majority level and number of GTO required per chamber

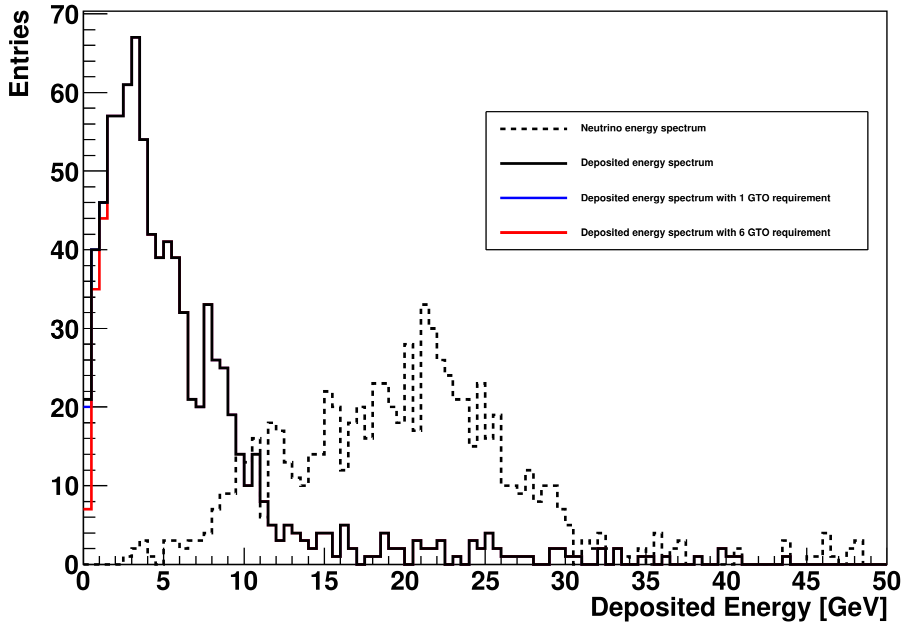

Figure 4.7: Neutrino energy spectrum of the ν_μCC Montecarlo sample (dashed line). The distortion of the deposited energy spectrum (in black) is shown for two values of GTO required per chamber GTO≥1 (blue line) and GTO≥6 (red line)

Threshold=6

	GTO > 0	GTO > 1	GTO >2	GTO > 3	GTO > 4	GTO > 5	GTO > 6
maj=10	99.9	99.8	99.2	98.8	98.4	97.7	97.4
maj=12	99.9	99.8	99.2	98.8	98.4	97.7	97.2
maj=14	99.9	99.7	99.0	98.7	98.2	97.3	97.1

Threshold=7

	GTO > 0	GTO > 1	GTO >2	GTO > 3	GTO > 4	GTO > 5	GTO > 6
maj=10	99.9	99.8	99.2	98.8	98.4	97.7	97.4
maj=12	99.9	99.8	99.2	98.7	98.4	97.6	97.2
maj=14	99.9	99.7	99.0	98.6	97.8	97.3	96.9

Threshold=8

	GTO > 0	GTO > 1	GTO >2	GTO > 3	GTO > 4	GTO > 5	GTO > 6
maj=10	99.9	99.8	99.1	98.6	98.4	97.5	97.4
maj=12	99.9	99.8	99.0	98.6	98.3	97.4	96.7
maj=14	99.9	99.5	98.9	98.2	97.4	96.7	95.9

Table 4.3: Percentage efficiency of the DR-slw filter on ν_μCC events as a function of the threshold, majority level and number of GTO required per chamber

4.2.2 2011 Data taking with the two level trigger

The commissioning phase of the two level trigger, started on 19th March 2011 with the first beam acquisition and ended on the end of April, has been addressed to prove the feasibility of such a filter, and to study the DAQ overload on a real data taking. The first issue has been to reach a filtering time of $\sim 1s$, necessary to keep on with the data taking, and to analyze any arrears which may arise from a filter crash. For this purpose, the filtering code has been optimized for processing speed and the analysis of one event has been parallelized over 4 different streams, one for each collection chamber. By running these processes on an 8-cores machine it was possible to reduce the processing time below one-second, as required. The DAQ processes have also been divided in 4 streams, one per chamber, resulting in a building time $<$ 2 sec.

To reduce the dead time for CNGS events (both triggered by PMT and by the software trigger) 3 out of 8 acquisition buffers have been dedicated to the CNGS events, 2 for any event tagged with the CNGS-gate, while the last buffer was reserved for CNGS events triggered by PMT. The trend of the dead time for each level of veto have been monitored during the whole 2011 data taking, and is reported in fig. 4.8.

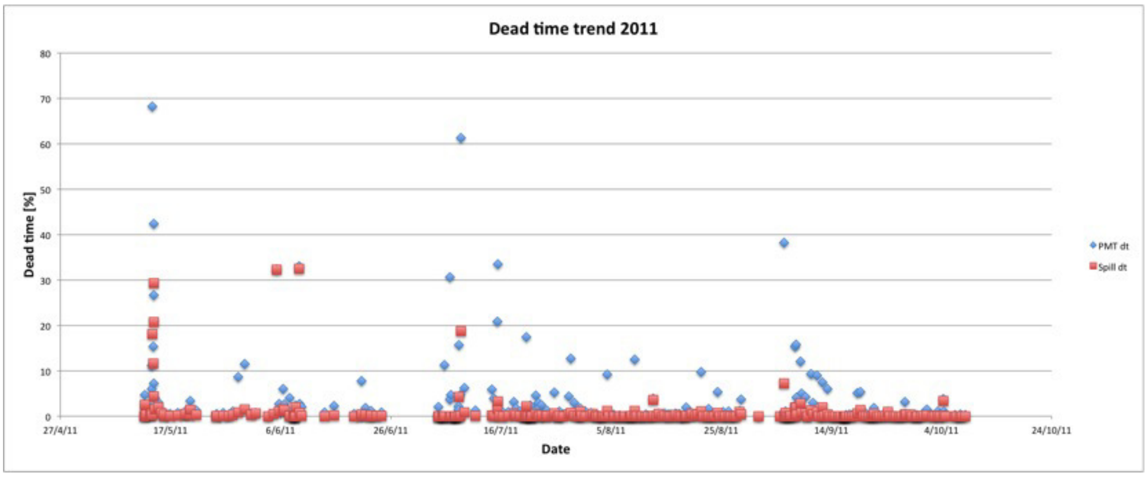

Figure 4.8: Dead time trend for the PMT cosmic trigger (in blue) and for the two level spill trigger (in red).

The continuous acquisition with the two level trigger started on the 3rd of May 2011 and ended on the 14th of November, with the beam stop. Although the data taking has been up for more than 6 months, as a consequence of a disk crash only a fraction corresponding to 94 day was completely recovered and analyzed. The data sample analyzed started from 12^{th} of May and ended on 8^{th} of October corresponding to a global delivery of 1,7 10^{19} p.o.t. The mean dead time for the two level trigger within this period has been 0,81% , but by weighting the live time run per run with the p.o.t. delivery, this number reduces to to 0,24%. During this period events have been filtered with the software trigger requiring a threshold of 7 ADC counts for a peak detection, a majority of 12 over 16 peaks, and a minimum of 6 GTO. The main problem observed arose from correlated noise over all the wires contained in few racks(fig. 4.9).

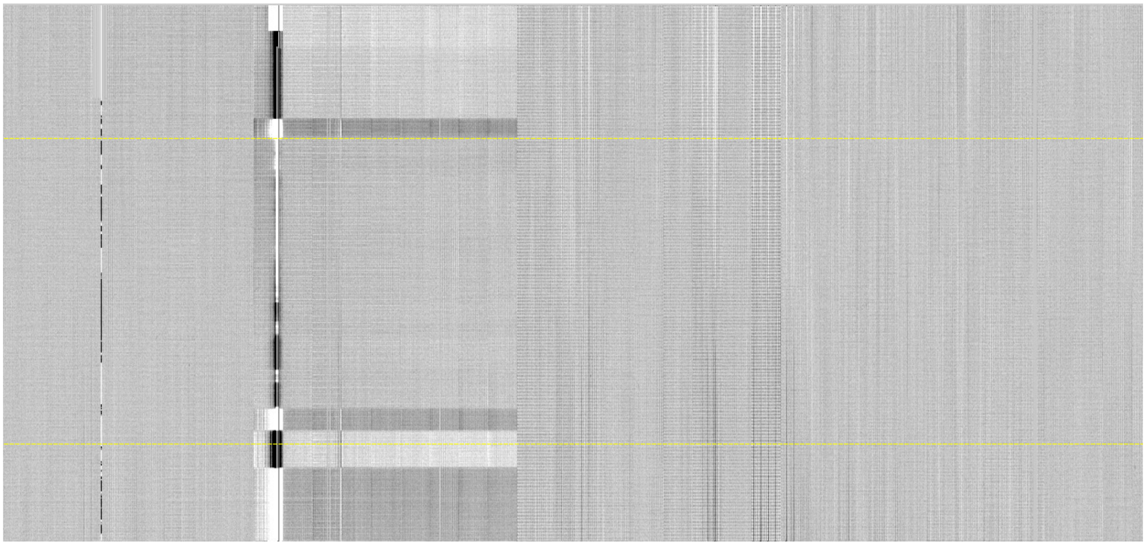

Figure 4.9: Example of the correlated noise affecting the events acquired with the 2-level trigger. The borders of the noisy region corresponds to an acquisition crate. The region between the yellow lines represent the physical drift following the CNGS extraction.

Since the noise is highly correlated, and affects all the wires in the same crate (corresponding to 9 consecutive GTO signals) it wasn't possible to reduce it acting on the majority level nor on the peak stretching. The only effective approach required the exclusion of the noisy rack from the trigger analysis, at the price of reducing the active volume for trigger. An average of the active volume weighted over the number of p.o.t. delivered run by run gave an overall reduction of the active volume of 2,9%. A total of 1,13 10^6 spills have been generated, out of which 6987 have passed the software requirement, proving a fraction of misidentification of 6×10^{-3}. Out of these events, only 16 resulted to be non-empty. All these events are muons coming from an external interaction of neutrinos with the external rock (fig.4.10).

This number must be compared with the total number of interactions recorded by the PMT system. In the same running period in fact the PMT trigger has been active, with a dead time of 2×10^{-3} and without cuts on the active volume related to the noise condition of the detector. The total number of muons from external interactions for the same run has been defined after a visual scanning of the CNGS-tagged events, resulting in 1979 muon events. This result shows how the PMT system is a reliable trigger, with an efficiency of 99,2% for muons from external interactions, and without any inefficiency w.r.t. the 2-level trigger for internal neutrino interactions over 587 neutrino interactions recorded in the period analyzed.

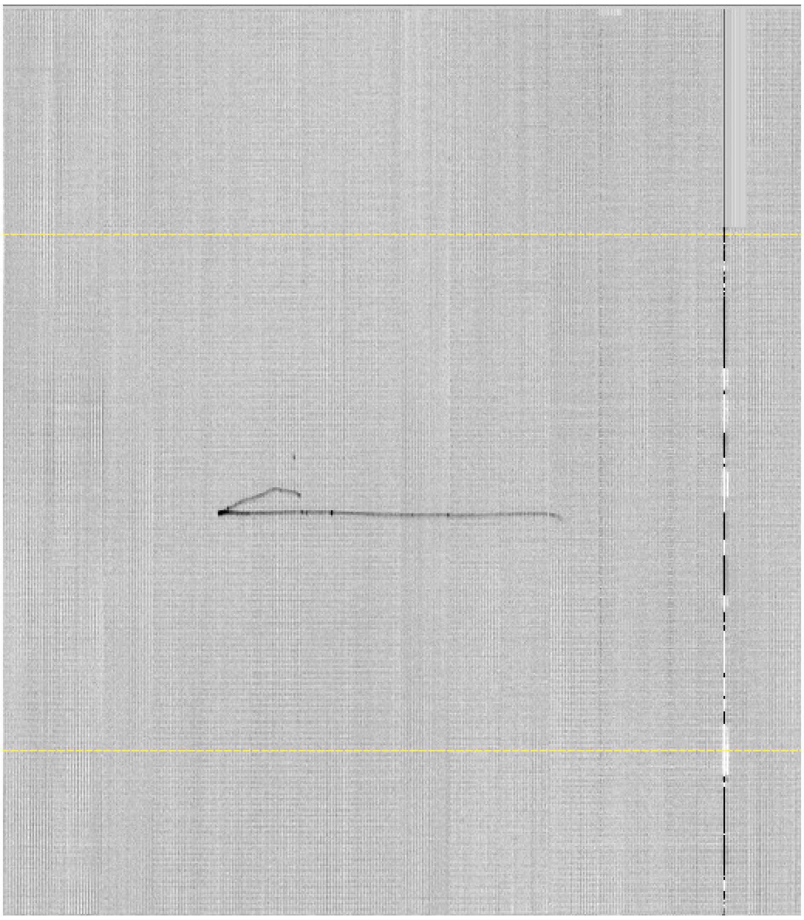

Figure 4.10: Example event acquired with the 2-level trigger and missed by the PMT trigger. For this events it is possible to identify the muon (track entering the detector from the right) which stops and decays into an electron. The energy deposited by this event is 140 MeV, the drift volume is delimited by the yellow lines.

4.2.3 DR-slw for CNGS event selection

Thanks to the good performance shown with the MC simulation and the 2010 dataset, the DR-slw filter has been used to identify the non-empty CNGS interactions candidates, recorded with the PMT+CNGS-gate coincidence. The processing of all 2011 and 2012 CNGS data begins with a “software CNGS gate” to recover any inefficiency linked with the early warning packet loss. In this procedure all the riggers that don’t have the CNGS tag are compared with the database holding the complete information of each extraction. If the time of the trigger falls within an interval of width 60 μs, centered at the time of extraction corrected by the neutrino time of flight, an off-line CNGS tag is raised, and the event is treated as a CNGS candidate. After the CNGS tag recovery all the candidates are filtered with the DR-slw algorithm, with the same parameters used for the on-line 2-level trigger, but without any reduction on the active volume, searching for at least 5 GTO signals in the same Collection view, corresponding to 40 cm along the wires direction. Out of more than 20000 CNGS candidates, the DR-slw selected a subsample of 6812 events. After the visual scan of these events a total of 942 neutrinos have been identified, 3088 muons from external interactions, 1340 residuals of external interactions and 1442 empty events. The remaining events of the 2011 and 2012 runs have already been filtered with the DR-slw and are undergoing the process of visual scanning.

4.3 Hardware implementation of DR-slw: the Super Daedalus chip

One of the most important applications of the DR-slw algorithm is its implementation on a hardware device, which continuously monitors the flow of data and generates a local trigger as soon as an ionizing event is recognized. Such a local trigger signal can be included in three different trigger scenarios:

- Region of Interest (RoI) selection: in this case a global signal of trigger, based on PMT activity, is given to the whole detector, and the local trigger coming from the Super Daedalus chip is used as a “trigger enable”. This solution permits the acquisition of the only part of the detector, which are interested by the ionization, avoiding the acquisition of unnecessary data (fig. 4.11). With the reduction of the event's size, the maximum PMT trigger rate sustainable by the DAQ increase, being the acquisition bandwidth constant. The reduction factor achievable with this setup ranges from $\sim 25\%$ for an horizontal crossing muon to a minimum of $\leq 4\%$ in case of a vertical crossing muon.

- Trigger on Super Daedalus: in this case a secondary trigger, parallel to the PMT trigger, is given to the whole detector as soon as one, or more, GTO signal is fired. In this situation the Super Daedalus trigger can recover any failure of the PMT setup, avoiding any bias on the primary trigger generation, at the expenses of an increased total trigger rate.
- Free running: this running condition is also defined as trigger-less. When a local trigger is recognized, only a small part of event is acquired, without any correlation with other boards. This running mode generates a continuous flow of "tails" of event, which must be correlated offline (fig 4.11).

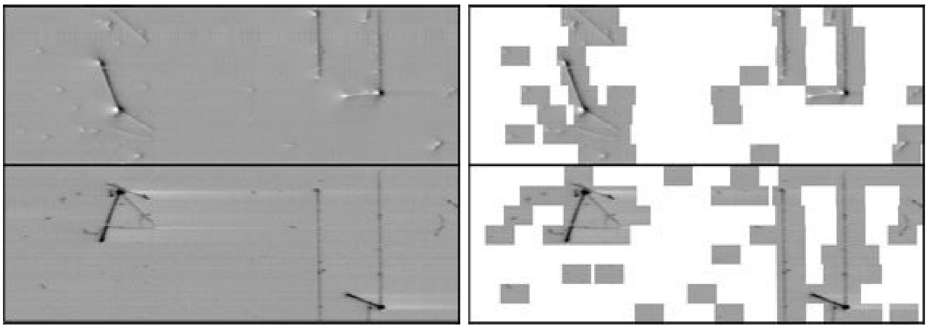

Figure 4.11: A wiew of an event before (left) and after (right) the selection of ROIs. The size of a single brick is given by the modularity of the electronic chain and of the size of the MEB.

For the data taking with the ICARUS T-600 detector the second running condition has been privileged, since it isn't affected by any bias related to the PMT spatial inhomogeneity, and can be thus a viable tool to cover its inefficiencies. The trigger-less scenario gives the possibility to optimize the data flow, reaching the maximum limit in terms of event acquired per second without any bias from the PMT setup. Anyway, the event rate expected at the LNGS site doesn't worth the effort of a more complex offline analysis, which is required to assemble different tails in order to define an event.

For the hardware implementation the most natural choice has been an FPGA device. This chips offers the great advantage of being reconfigurable, thus any modification and improvement that may be needed during the data taking, could be done without changing any hardware components. Moreover, thanks to the use of a standard hardware description language, such ad VHDL, it has been possible to migrate the project to a smaller, and cheaper, FPGA model after a first developing phase carried out on a more powerful device.

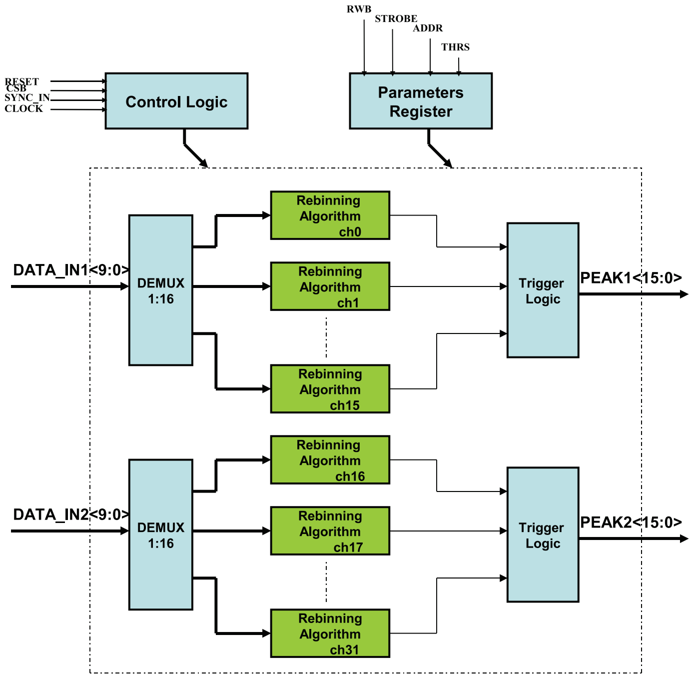

Figure 4.12: Block diagram of the DR-slw implementation on the Xilinx Virtex 5 FPGA.

The architecture of the filtering algorithm is depicted in fig. 4.12: after a first phase of demultiplexing, all the 32 channels are treated in parallel by the same filtering block. For each 2,5Mhz clock cycle, the value of the long (short) average is updated by adding the incoming value T_0 and subtracting the value at sample T_{0-128} (T_{0-8}) stored in a dedicated shift register. When the difference between the short and the long average is above threshold for at least 3 consecutive samples a peak signal is output. The device chosen for the prototypal implementation has been a Xilinx XC5VLX50 Virtex 5, which has been installed in a dedicated piggyback to fit the existing digital board (fig. 4.13).

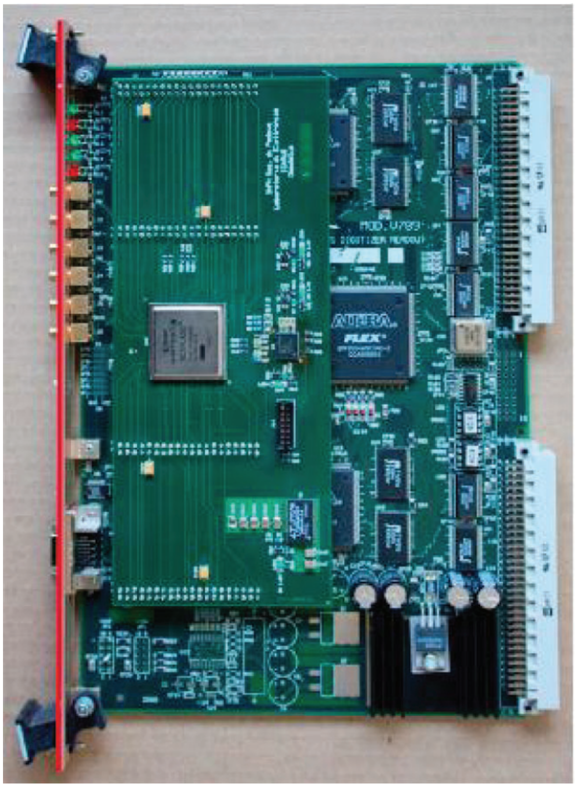

Figure 4.13: Digital read-out board equipped with the Super Daedalus chip.

4.3.1 Design validation with the Icarino test facility

After a complete simulation on the 2001 dataset, the complete algorithm has been tested on a dedicated run in 2009 with the Icarino test facility[34].

The experimental set-up, described in detail in [35], consists of two vertical electrode planes, 32.6×32.6 cm^2, acting as anode and cathode, laterally delimited by 4 vetronite 29.4×29.4 cm^2 boards supporting the field-shaping electrodes (30 strips of gold-plated copper) resulting in a 38 kg LAr active mass (Fig. 4.15). In order to facilitate the LAr re-circulation in the TPC active volume, the cathode at the front of the chamber has been realized with a thin etched stainless steel grid.

The chamber is contained in a stainless steel cylindrical vessel, whose upper face is an ultra high vacuum flange hosting the feed-throughs for vacuum, LAr filling and re-circulation, high voltage cables and read-out electronics. The whole detector vessel is contained in an open-air stainless steel dewar, which is initially filled with commercial LAr acting as cryogenic bath for the ultra-pure LAr injected in the detector vessel.

The read-out anode's electrodes facing the drift volume are two parallel 96 stain-

Figure 4.14: The ICARINO test-facility set-up at LNL.

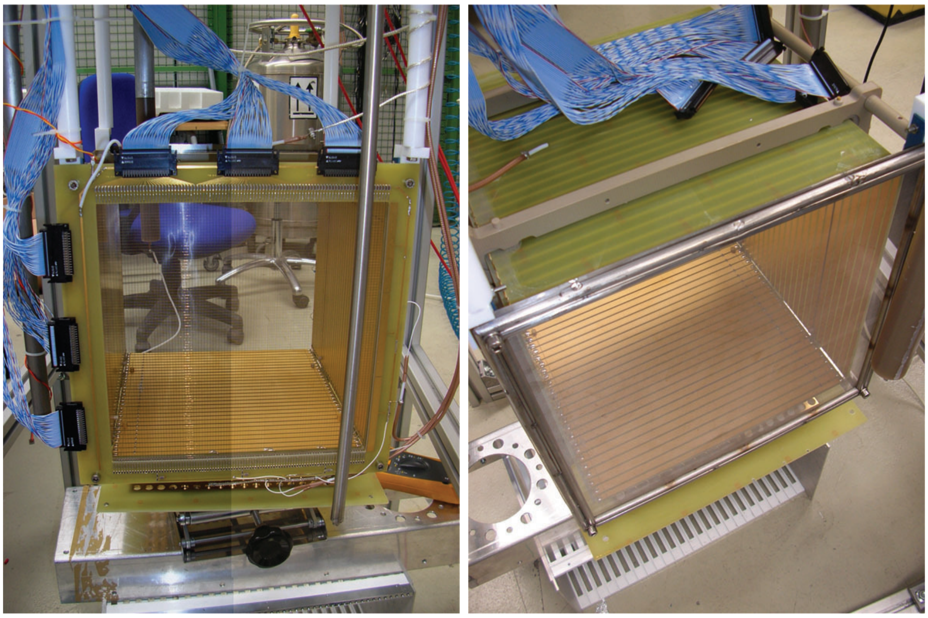

Figure 4.15: Images of LAr-TPC at LNL: anode (left) and cathode (right) structure of the TPC.

less steel wire planes spaced by 3 mm and with 3 mm pitch: the first one works in Induction mode and is made of vertical wires while the second one collects the drifting electrons and is made of horizontal wires. A third wire plane electrically biased, called grid, is inserted 3.5 mm in front of the Induction wires. It acts as an electromagnetic shield improving the Induction signal sharpness and reducing the noise due to the HV biasing. Finally, another thin stainless steel grid has been inserted behind the Collection wire plane and put to ground to confine the electric field around the wires.

The main purpose of the test run has been to verify the layout and implementation of the chip implementing the algorithm, and to check the efficiency during the data taking, in both Induction and Collection views. Two sets of crossing muons have been analyzed, vertical and with a with a zenith angle of 45° both triggered with an external setup of scintillating slab. The results obtained with this run have confirmed the validity of the algorithm showing an efficiency exceeding 95% on single hit detection in both the dataset with for a threshold $Q_{thr} \leq 7$ and a fake frequency decreasing down to 10^{-3} for $Q_{thr} \geq 6$ (fig. 4.16).

The setup gave also the opportunity of testing the limits of the algorithm on low energy events detection. By triggering on the central collection board, in anti-coincidence with the two lateral boards, it has been possible to select a sample of data with a small deposited energy, mainly neutrons and photons(fig. 4.17).

The spectrum of the events taken with two sets of parameters, threshold Qthre= 5 ADC counts majority M=3 out of 16 and Qthre=6 ADC counts M=4, reported in fig. 4.18, shows the great capability of such a trigger in triggering low energy events. It's worth noting that this outstanding result was made possible by the high level of purity of the liquid argon, $\tau_{ele} = 21 \pm 5ms$[ref purezza], which permits a low signal attenuation, enhancing the signal to noise ratio.

4.4 First Super Daedalus test on the T-600 detector

After the first verification phase, the architecture has been revisited, in order to fit a smaller, and cheaper device. The first modification introduced has been the use of a FIFO, implemented with the dedicated block ram of the device, instead of the previous shift registers implemented with the distributed ram. A second modification has been the inversion of the demultiplexing and the filtering block. In the new architecture, the data-flow is firstly input in the “Rebinning Algorithm” block, where the algorithm is applied channel by channel by two parallel identical blocks, running each at a fre-

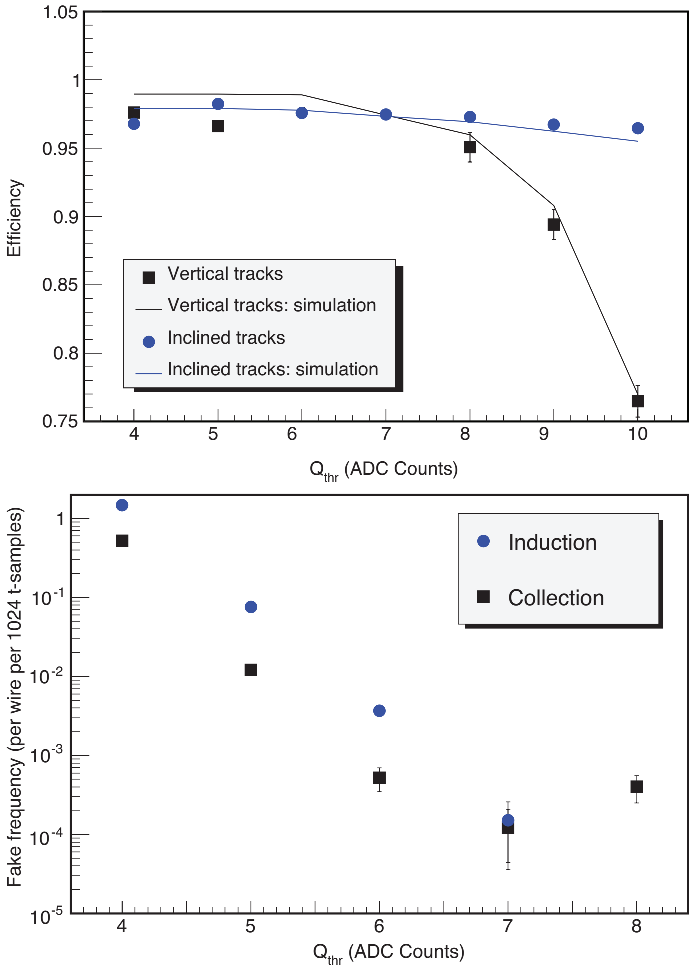

Figure 4.16: Super Daedalus efficiency (top) for horizontal and inclined track in Collection view, and frequency of fake triggers (bottom) in both Collection and Induction view as a function of the peak detecting threshold for the Icarino 2009 run

quency of 40 Mhz; subsequently the output of the algorithm block is demultiplexed, in order to give two parallel streams of 16 channels at a frequency of 2,5 MHz. This new architecture permits to use only two “Rebinning Algorithm” block, one per each set of 16 consecutive channels instead of the previous usage of 32.

After the optimization, the design could fit on the smallest FPGAs of the Spartan family (tab. 4.4); the choice of the Xilinx Spartan 6 XC6SLX16 device has been done in order to have enough space to fit any other modification that might be needed, and to provide a longer support, being the Spartan 6 the latest product family supplied by Xilinx at the time of the electronic development.

One of the first additions made to the original code has been the introduction of

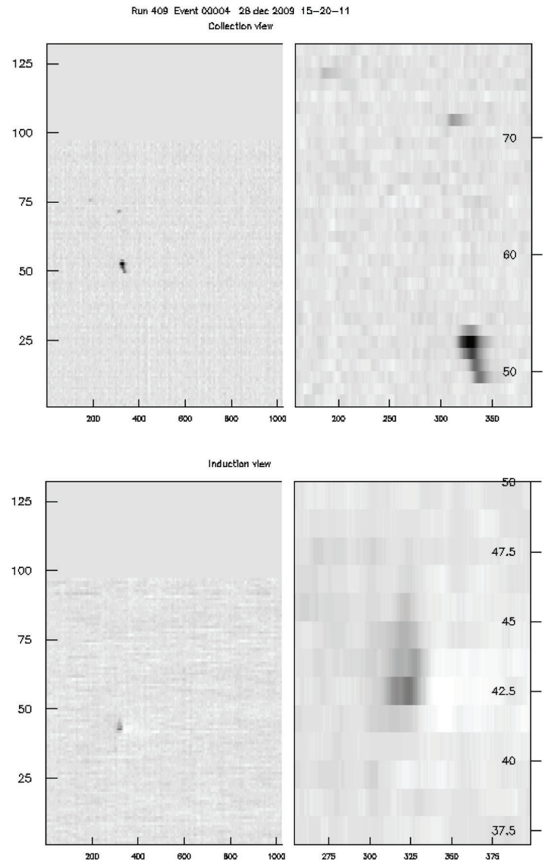

Figure 4.17: Example of an event acquired with the "low energy trigger" during the Icarino data taking, both for Collection (top) and Induction(bottom) view. The deposited energy of the event is $\leq 5MeV$

FPGA Model	Occupied Cells	Occupancy [%]	Package
XC3S200A	1754	97%	FT256 BGA
XC3S400A	1792	50%	FT256 BGA
XC3S200	1762	91%	PQ208 QFP
XC3S400	1762	49%	PQ208 QFP
XC3S250E	1749	71%	PQ208 QFP
XC6SLX16	1749	33%	FTG256 BGA

Table 4.4: DR-slw occupancy on several models of the Xilinx Spartan family

a watchdog on the PEAKs activity. This decision follows the consideration that any bit-flip that might be happen during the writing or reading procedure onto the FPGA would produce an offset on one of the two averages which wouldn't be recovered until a global reset of the system. To avoid this situation, a watchdog stage has been implemented after the "Trigger Logic" block, where the PEAK signals are generated

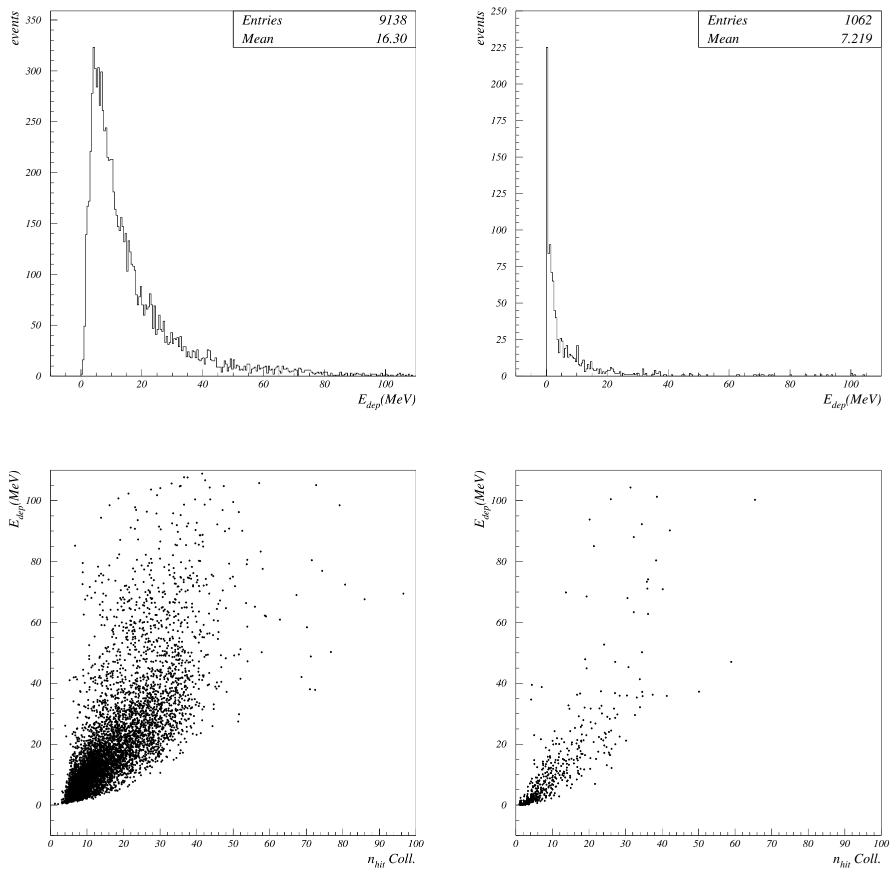

Figure 4.18: Energy spectrum of the events recorded in the Icarino 2009 run with the low energy trigger for threshold 6 and majority 4 (top left) and for threshold 5 and majority 3 (top right). For the same run is shown also the number of hit reconstructed by the analysis software as a function of the deposited energy (bottom left and right, for the two sets of parameters

and stretched. If the number of peaks contemporarly active exceeds the value of majority fixed for the run, a reset signal is given to the whole procedure, and the FIFOs are cleared. This process doesn't affect the global trigger logic, since the reset procedure is much shorter than the time needed for a complete drift, meaning that the filtering algorithm returns completely operational well before the global trigger is rearmed.

At the beginning of November 2010 a first set of 9 Super Daedalus Virtex5 boards have been installed on the digital boards of the crate with CPU icab34, in the middle of the I-L chamber, which houses 9 board of Induction2 view and 9 boards of Collection view. 5 boards have been installed in Collection view, boards from 13 to 17, and 4 in

Induction2 view, boards from 4 to 7. A first check of the functionality of the board has been done by monitoring the trigger frequencies of each GTO output as a function of the majority level, being the threshold fixed to 6 ADC counts and the stretching fixed in the range 25 to 50 μs. The response of the devices installed has shown a good homogeneity, showing no relevant differences between the behaviors of the boards installed in Collection and Induction2 view (fig.4.19). The rate of triggers achievable with the requirement of 5 peaks signals over 16 consecutive wires, corresponding to a track length of 1,5cm along the wires direction, is completely sustainable by the DAQ bandwidth, even when scaled up to the whole detector.

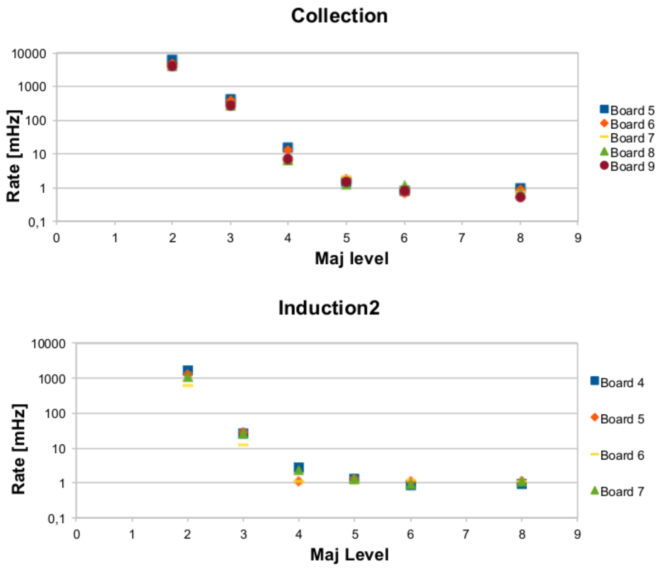

Figure 4.19: Trigger frequencies of the GTO signals during the first test on Icarus T600, both for Collection (top) and Induction2 (bottom) view and for the different boards.

A second test has been done in January 2011, adding 8 Super Daedalus Spartan6 boards, thus equipping the whole digital crate, with the exception of the first Induction2 board. The 3rd board of Induction2 and the 1st and 9th board of Collection were not functional, due to a failure of the firmware installed and to a problem on the connection between the boards and the trigger manager FPGA, which has been used to monitor the GTO activity. The test was thus made on 7 boards of Induction2 and 7 boards of Collection. The check on the trigger frequencies of each GTO output as a function of the majority level has been repeated, being the threshold fixed to 6 and 7 ADC counts. The response of the devices has shown a big difference w.r.t. the one reported on the previous test(fig. 4.20).

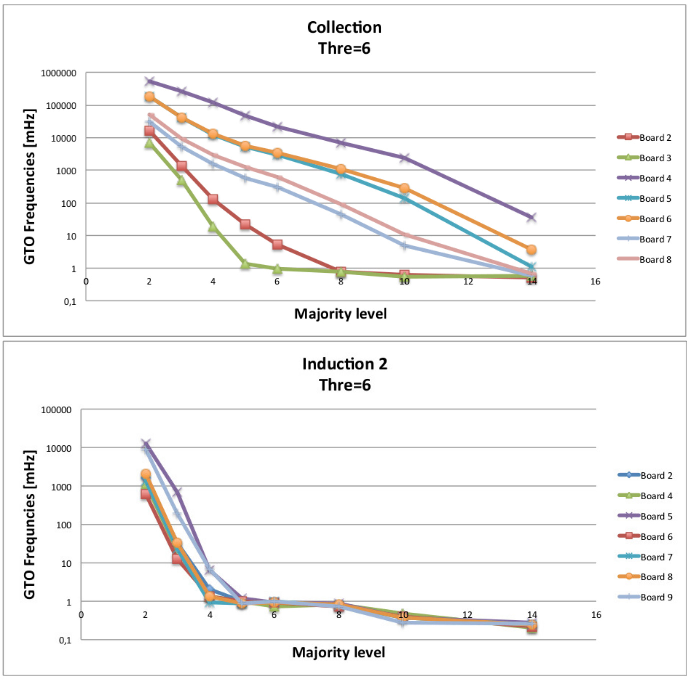

Figure 4.20: Trigger frequencies of the GTO signals during the second test on Icarus T600, for Collection (top)view.

To understand this phenomenon two dedicated runs with periodic trigger, made just before the first test and after the second test, have been analyzed. For all the events of these runs, the average r.m.s. of the signal of each channel has been calculated, as well as the mean r.m.s. of the channels from the same board. Since the trigger was not correlated with any activity inside the detector, the value of r.m.s. is influenced only by the electronic noise level. As shown in fig.4.21 the noise level in November, in blue, appears to be much lower and more uniform than the level recorded in January, in red. This difference is particularly evident in Collection view, and is probably related to an intervention made on the PMT setup during December 2011.

To reduce the noise level, which would saturate the DAQ bandwidth, a campaign of electronic upgrade has been made in February and March 2011, before the CNGS beam operation. To reduce the electronic noise, several boards have been changed, the grounding layout has been revisited, as well as the shielding of the path of the analog signal.

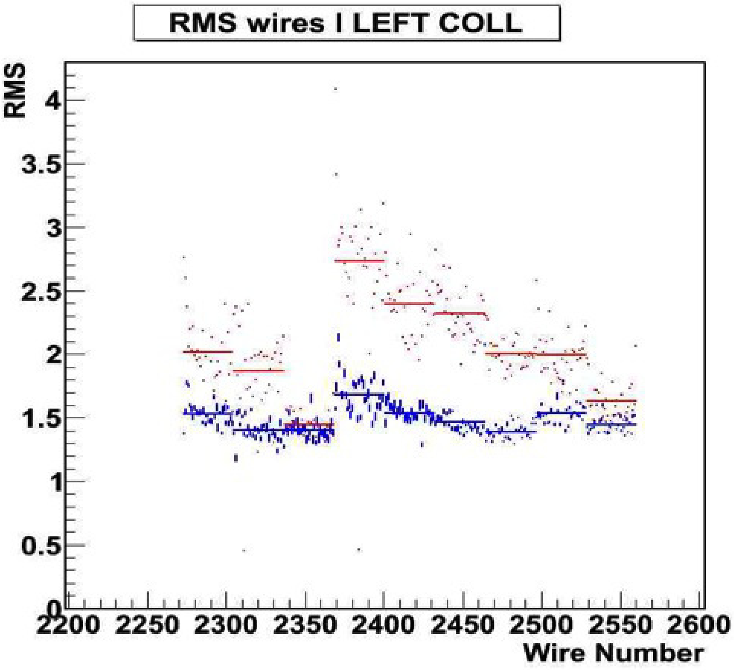

Figure 4.21: Noise comparison in the period of the first test (in blue) and second test (in red). The points represent the mean noise value for each wire, while the bars represent the averages over the boards

After the intervention the noise level has returned to the standard value, allowing the GTO signal to be included in the trigger system. The first test of data taking with the GTO signal included in the trigger has been done at the beginning of April, when the GTO trigger has been enabled, in parallel to the PMT trigger. The parameters chosen for the trigger have been threshold Q_{thr}=6 and majority M=6. The stretching was fixed to its maximum value, ranging from 100 to 125 μs. The complete run lasted almost 15 hours, recording a total of 35 events triggered only by the Super Daedalus trigger, without any PMT activity. The energy distribution of the events triggered only by the Super Daedalus trigger (fig.4.22) shows that the trigger on charge can recover the PMT inefficiency in two distinct regions of the spectrum: the low energy tail of the atmospheric muon spectrum, and the very low energy spectrum (< 15 MeV) which is of particular interest for the detection of solar and Supernovae neutrinos (fig.4.23).

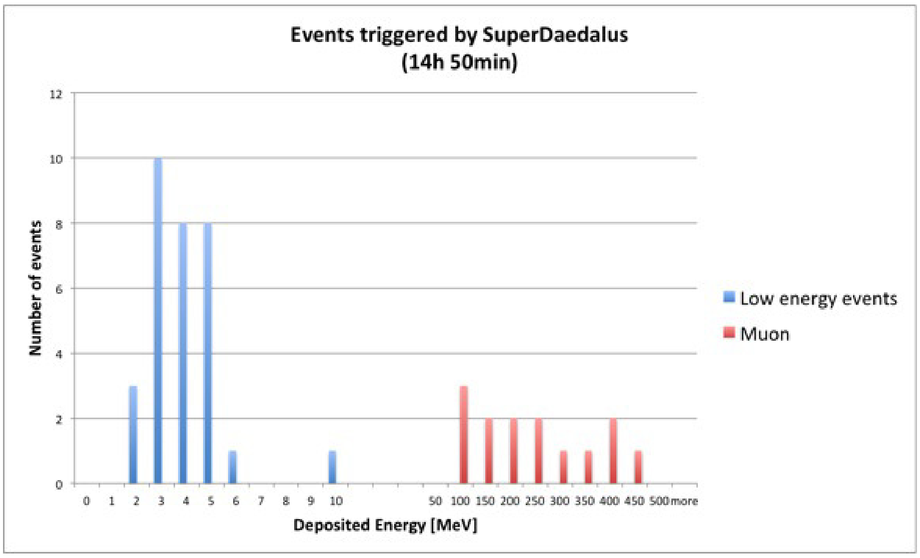

Figure 4.22: Energy spectrum of the events acquired during the first test of trigger on Super Daedalus

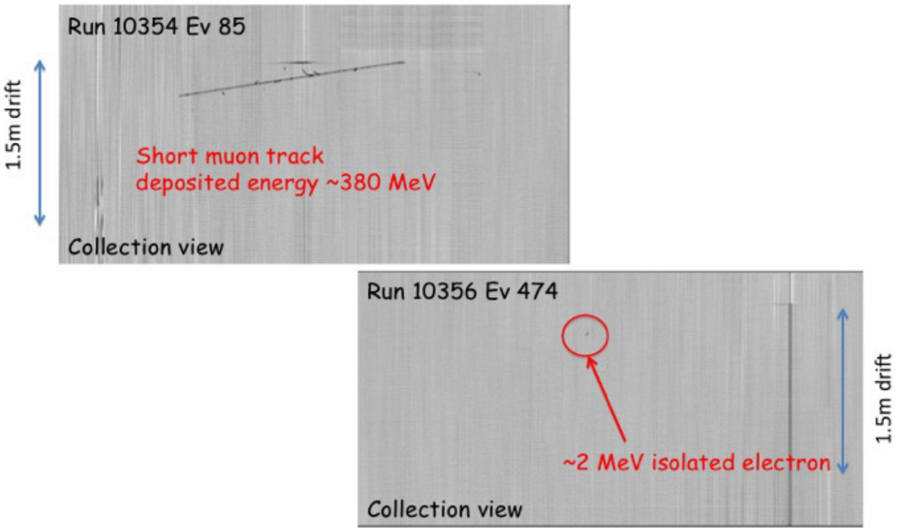

Figure 4.23: Examples of two events acquired with the Super Daedalus trigger during the first test run

CPU	GTO rate [mHz]	CPU	GTO rate [mHz]
icab 28	2	icab 37	248
icab 29	2	icab 38	1
icab 30	0	icab 39	2211
icab 31	484	icab 40	0
icab 32	1	icab 41	647
icab 33	1283	icab 42	1
icab 34	2	icab 43	731
icab 35	19	icab 44	0
icab 36	3	icab 45	1

Table 4.5: The Super Daedalus average trigger rates of the first 2011 test run show a high trigger frequency on the crates that are in the proximity of a PMT

4.5 PMT T0 filter

During 2011 a second batch of 60 Super Daedalus have been delivered and installed in the detector. To monitor the behavior of different crates they have been installed every third board in the whole Collection view of the I-L chamber. A first study of the frequencies of the trigger rate has shown an anomalous behavior of the rate of the boards installed in the CPU with an odd number, from icab31 to icab43 (tab. 4.5). The high frequency of the GTO signal doesn't seems to be correlated with the noise level of these boards, and is too high to be introduced in the trigger system. To study the reason for such a high rate of trigger a set of run has been done including in the trigger rate the noisy crate one by one. The visual scan of the events acquired with this trigger has shown that the problem of the high trigger rate is linked with the activity of the PMT tubes, which induce a correlated signal on adjacent wires (fig.4.24). The pattern of the problematic crates reflects the spatial distribution of the PMT tubes.

A detailed analysis of the signal induced by PMT has been carried on the events acquired with the Super Daedalus trigger. The signal has a bipolar shape, with an initial negative pulse of mean height of -35 ADC counts, followed by a positive pulse with mean height of 15 ADC counts. The length of the positive edge ranges from 20 to 40 samples. To avoid the Super Daedalus to trigger on the PMT induced signal, another filtering stage has been added to the algorithm. In parallel to the DR-slw filtering, the new algorithm searches for a negative pulse on the signal obtained by subtracting to the ADC samples the baseline calculated on the previous 128 samples (i.e. the long bin). If the number of wires that goes below a certain value of negative

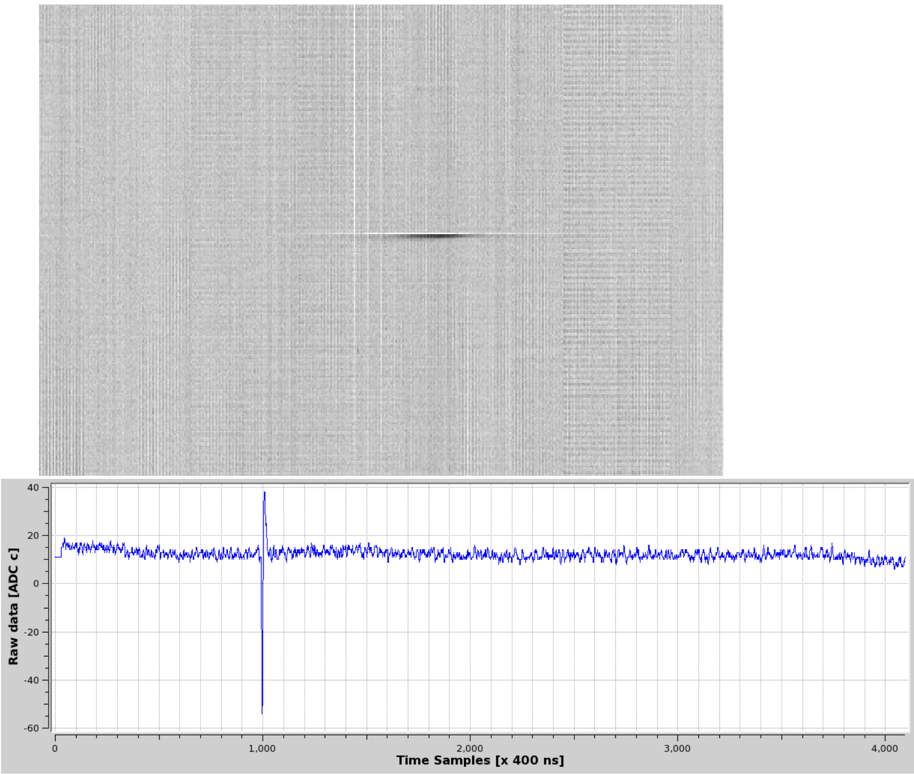

Figure 4.24: Event view of the signal induced on the TPC wire planes by the PMT activity (top). The signal recorded by a single wire is also shown (bottom).

threshold exceeds a definite value a veto is set to the generation of PEAK signals for the next 200 samples. Both the value of the negative threshold and the value of majority for the inhibit signal are programmable run by run, via a dedicated register stored in the FPGA, but after some dedicated signal analysis the best set resulted to be -10ADC count for the negative threshold and 5 wires over 16 for the majority level.

After the verification phase of the new implementation, a campaign of firmware upgrade has been done to the whole chip already installed in the detector, while a second batch of SuperDaedalus chip has been produced. The verification and installation of the new batch of chips ended in December 2011, and the commissioning phase of the new trigger started in January 2012. A detailed description of the running phase with the SuperDaedalus trigger will be given in the next chapter.

Chapter 5

Data taking with the Super Daedalus

After the production of the first batch of 716 SuperDaedalus chips, needed to equip the whole Collection views, a huge effort has been addressed to the installation, testing and integration of the new chip into the trigger. The Super Daedalus commissioning started in January 2012, and soon after the beginning of the 2012 CNGS run, the Super Daedalus chip have been enabled to trigger in coincidence with the CNGS-gate, as a replacement of the 2-level trigger described in the previous chapter. After few months of tests, needed to enable the Super Daedalus for atmospheric events without perturbing the data taking for CNGS events, the Super Daedalus have been included into the trigger also for non beam-related events. Finally, after the installation of a second batch of 980 chips, occurred in November 2012, the Super Daedalus has been active in both the Collection and Induction2 view.

In this chapter the hardware layout will be described in detail, together with the results of 2012-2013 data taking based on the Super Daedalus, as well as the perspectives for the remaining 2013 acquisition. The trigger capabilities of the Super Daedalus for the expected exposure will be also given.

5.1 Hardware layout

Due to the high granularity of the Super Daedalus chip, which is capable of generating a trigger over a set of 32 wires, the total number of GTO signals to be handled by the trigger logic results in 716 independent signals for both Collection and Induction2 views, and 264 signals for Induction1. This huge amount of signals must be grouped before being sent to the main trigger logic, in order to reduce the complexity of the

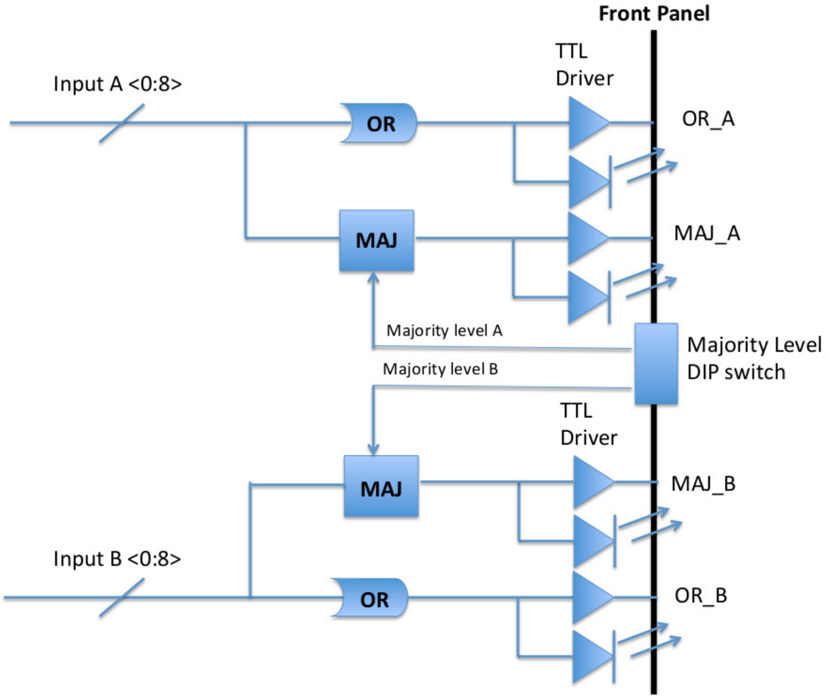

Figure 5.1: Schematics of the GTO OR/MAJ board.

global trigger algorithm and to limit the I/O and cables needed to handle such a high number of lines.

To provide a reduction of the signals received by the main trigger logic, without degrading the efficiency of the Super Daedalus chip, a new VME board has been developed, named “GTO OR/MAJ”. It receives two sets of 9 inputs, and performs the logical OR and the majority on both sets, where the majority level can be set trough a dip switch placed on the front panel. The outputs, constituted by a couple of separate 3,3V TTL channels for each set of 9 wires, are put beside a LED, which is used to visually monitor the behavior of the lines (fig. 5.1).

Each digital rack has been equipped with one “GTO OR/MAJ” board, together with a custom cable connecting all the GTO output coming from the digital boards to the “GTO OR/MAJ”. For the crates containing the read-out of both Collection and Induction2 wires, the GTO signals have been split in two groups according to the corresponding view, while for the crate housing boards of the same view, the splitting has been based upon the wire position, keeping the adjacent boards in the same subset of the “GTO OR/MAJ” board.

To minimize the number of wires required, only the majority signal have been cabled, the OR function being achieved acting on the majority level dip switch. The total number of signals per chamber resulting after this grouping are 20 for both the Collection and Induction2 views, and 8 for the Induction1 views, for a total of 192 signals for the whole detector. To handle all the I/O, a second FPGA board (PXI-7833) has been added to the trigger manager, for a total of 160+96 digital I/O for the complete system, sufficient for the Super Daedalus signals plus the other signals required for the data-taking. The connection between the two devices, necessary to share common signal such as trigger, busy and trigger mask, is provided by few dedicated lines on the PXI backplane.

5.2 Signal handling

The first effort made for including the Super Daedalus output signals into the main trigger logic has been the reduction of the overall GTO trigger rate to a level that can be handle by the DAQ system, not to interfere with the main trigger based on the PMT signals. To monitor the activity of each signal coming from the “GTO OR/MAJ” boards, each input is connected to a process which measures the trigger frequency of the line. For each line, as soon as a positive edge is recognized by the FPGA, a dedicated counter is incremented by one unit and a veto of 1 ms is set to the line, to prevent multiple counts for events with multiple tracks. Every second, the PXI controller read and reset the counter, and keep track of the mean trigger rate by averaging over 100 or 1000 sec, as selected from the main interface(fig. 5.2). The trigger rate resulting from this measurement are displayed by a dedicated indicator on the main interface, for all the acquired channels. Since different crates exhibit different trigger rates, related to the inhomogeneity of the noise level, a selective veto can be applied to the trigger coming from each crate, which excludes a particular line from the trigger, while leaving the the other lines active.

After the first test made with this new setup, it resulted clear that a manual procedure for excluding the problematic lines was not adequate to follow the random behavior of the different trigger rates, which reflect the noise condition of the detector. In fact, the sum of several uncorrelated noise source, such as the cryogenic pumps, the PMT HV distribution and the electronics power supply, result in a unpredictable noise condition, which may vary several times a day. To overcome this instability, an

	Daedalus I-L [mHz]	Daedalus Enable 1	Daedalus I-R [mHz]	Daedalus Enable 2	Daedalus II-L [mHz]	Daedalus Enable 3	Daedalus II-R [mHz]	Daedalus Enable 4
	0	0	0	0	0	0	0	0
	1	🟢	2	🟢	0	🟢	612160	⚫
	56106	⚫	5	🟢	0	🟢	4	🟢
	4	🟢	5308	⚫	4	🟢	6	🟢
	0	🟢	6336	⚫	2	🟢	4	🟢
	2	🟢	1	🟢	0	🟢	2	🟢
	0	🟢	0	🟢	0	🟢	5684	⚫
	0	🟢	0	🟢	13	🟢	5	🟢
8	4	🟢	0	🟢	2	🟢	3	🟢
	387	⚫	1901	⚫	50	⚫	5	🟢
	3	🟢	9	🟢	5	🟢	7	🟢
	4	🟢	3	🟢	5	🟢	4	🟢
	2	🟢	3	🟢	0	🟢	7	🟢
	2	🟢	6	🟢	6	🟢	89913	⚫
	2	🟢	3562	⚫	4	🟢	1	🟢
	2	🟢	12	🟢	3	🟢	8	🟢
16	1	🟢	1250	⚫	6	🟢	8	🟢
	1000680	⚫	3	🟢	437273	⚫	44813	⚫
	24	🟢	7	🟢	3	🟢	22085	⚫
	2	🟢	1860	⚫	2	🟢	2	🟢
	3	🟢	60962	⚫	0	🟢	119	⚫

Daedalus Veto Threshold 30

Figure 5.2: View of the main trigger interface. All the trigger rates for SD in collection views are displayed in mHz, while the veto is represented by the array of LED. The control for setting the threshold of the automatic veto is also shown.

automatic process has been developed, which automatically disable the lines which exhibits a problematic behavior. The process is based on the trigger rate of the different lines: each time the frequency of a line exceeds a frequency threshold the line is disabled, while if afterward it drops below the fixed value it is re-enabled. Two sets of threshold frequencies were chosen for CNGS and atmospheric events, 300mHz and 30mHz respectively. Whenever the trigger frequency of one line is above 300mHz, the corresponding crate is excluded for all triggers, if it is between 30 mHz and 300 mHz it is enable only in the millisecond following a CNGS extraction, while if it is below 30 mHz it is always active.

To keep track of the detector volume in which the Super Daedalus trigger is active, which continuously changes, every time a line is enabled or disabled the information of all the disabled crate is sent from the RT controller to a PC running in control room, which logs the time and the pattern of disabled crates. On the basis of this information it is possible to reconstruct the detector volume in which the Super Daedalus trigger is active, bot for CNGS and atmospheric events.

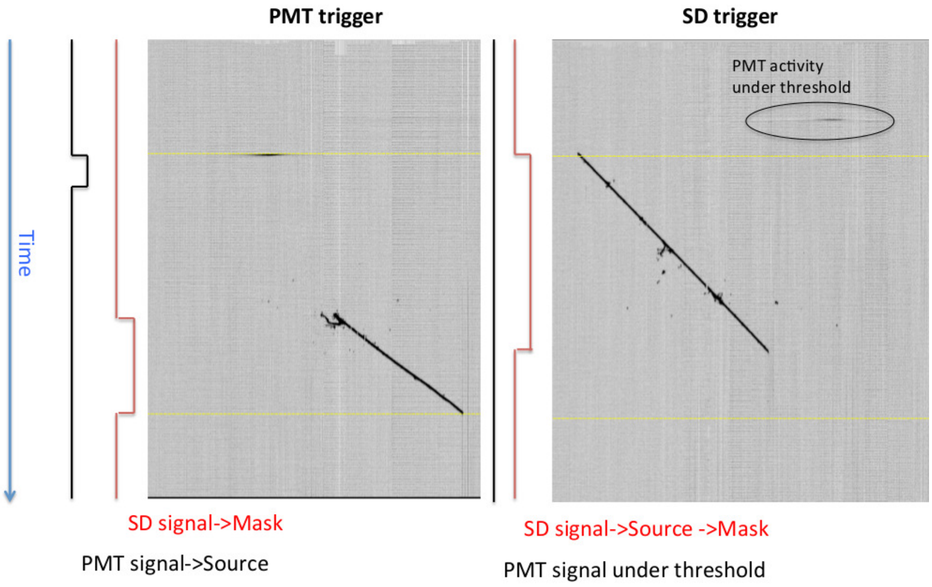

Figure 5.3: Examples of events triggered by PMT (left) and SD(right).

5.3 The new trigger logic

Since March 2012 the Super Daedalus trigger has been included for a preliminary commissioning phase into the trigger logic in parallel to the PMT signals, which remained the main trigger source as they provide a prompt signal giving a precise information of the time of interaction. When an event occurs in the T600 detector, if the PMT signals is above threshold, the chambers firing the trigger are recorded as trigger source, while the pattern of the Super Daedalus which follows the primary trigger are recorded as trigger mask. In case the PMT activity is below threshold, the first Super Daedalus signal is recorded as source, while any other signal occurring in the following millisecond is recorded as trigger mask(fig.5.3).

The distinction of the data is based on the trigger source, so that any event which received a trigger from the PMT is defined as PMT-trigger, independently from the Super Daedalus activity. On the other hand, all the event that exhibits a Super Daedalus pattern as trigger source , and which would have been lost by the PMT setup, are defined as SD-triggers, and follows a different analysis. This distinction has the advantage that all the PMT-triggers have a well defined interaction time, and thus don't need any further correction for what concerns the definition of the fiducial volume and on the reference time needed to estimate properly the signal attenuation due to the argon impurities. The SD-trigger instead need the analysis of the PMT waveform, to extract the precise time of interaction.

5.4 2012 CNGS run with Super Daedalus

From June 12^{th} to the end of the 2012 CNGS run, in November the 5^{th}, the Super Daedalus have been included into the trigger replacing the two level trigger described in the previous chapter. The new setup, thanks to the automatic veto which disabled the noisy region, have permitted to reduced the number of GTO firing per chamber from 5 to 1 inside the active volume. This reduction in the event size required for triggering has permitted to check the efficiency of the PMT system also for the low energy tail of the NC spectrum, for which the requirement of 5 GTO signals produces some inefficiencies (fig. 4.6).

For this purpose the majority level of the “GTO OR/MAJ” boards have been set to zero, thus performing the OR of all the inputs. The trigger procedure starts with the CNGS-gate, which initializes a state machine inside the trigger FPGA that handles the Super Daedalus signals. Only if a SD-trigger occurs in the first millisecond following the expected interaction, a trigger is given to the whole detector and the event is acquired. After the acquisition of one event, an automatic process analyzes it searching for a minimum of GTO in the same chamber. The number of GTO required has changed during the run, with a value of 5 GTO from June 12^{th} to July 3^{rd}, 2 GTO from July 3^{rd} to October 12^{th} and then no further requirement have been made from the off-line filter until the end of the CNGS run. These requirements greatly reduce the residual rate of empty triggers, while maintaining a good efficiency on small tracks. The number of p.o.t. weighted by the trigger active volume has been 1.0×10^{18}, 8.9×10^{18} and 4.1×10^{18} respectively, for a total of 1.4×10^{19} p.o.t. analyzed.

The same 3-level veto structure used for the 2011 run has been adopted also for the 2012 run, resulting in a dead time for CNGS+Super Daedalus trigger of less than 0.1%.

To further reduce the number of fakes, all the CNGS+Super Daedalus events have been filtered with the CEF, resulting in 19 candidates out of 758 primary triggers.

First run	Last run	#GTO	Integrated p.o.t.	Interactions
11534	11615	5	1.0×10^{18}	3
11616	11945	2	8.9×10^{18}	6
11946	12084	1	4.1×10^{18}	3

Table 5.1: Summary of the results of the CNGS+ Super Daedalus trigger for the three different periods.

The visual scanning of the filtered events resulted in 8 tracks of muon from external interaction, 3 atmospheric muons and one interaction of a neutral particle inside the detector (tab. 5.1).

The analysis on the 2012 data is in well agreement with what emerged for the 2011 run, confirming a full efficiency of the PMT setup for the CNGS neutrino interaction and a <1% inefficiency for muon coming from external rock. The neutral interaction (fig. 5.4) is most likely a neutron coming from an external interaction. The distance from the closest wall is $\sim$ 40 cm, well compatible with the neutron mean free path in LAr, $\sim$ 80 cm, while the particle direction suggests that the event is related to some CNGS external interaction.

5.5 2012 Atmospheric run with Super Daedalus in Collection view

Super Daedalus have been enabled for triggering atmospheric events few months later than their introduction into the CNGS trigger. The distinction of the events by trigger source have been maintained, as well as the setting on the “GTO OR/MAJ” boards. The cosmic data taking can be divided into four different periods, according to the number of GTO required by the off-line filter, as well as on the parameters set on the Super Daedalus chips (tab.5.2). A second distinction must be considered for the forth period in which, only for the western Module, the SD trigger has been enabled in Induction2 instead of Collection.

As a preliminary analysis, the wire occupancy of the events triggered both by PMT (with and without a following SD activity) and by SD (with no PMT activity over threshold) has been studied. The distribution obtained, shown in fig.5.5, reflects several aspects related to the data-taking condition. The first wires of the I-L chamber showed a noise level too high to be included into the SD trigger, therefore they have

Figure 5.4: Neutral event triggered by CNGS gate + Super Daedalus. The there views, Induction1 (top left), Induction2 (top right), Collection (bottom), are shown: the yellow lines represents the detector volume.

Period	Exposure [days]	# GTO	Threshold	Majority
1	5.2	2	7	12
2	16.8	2	8	10
3	37.8	1	8	10
4*	7.8	1	8	10

Period	Dead time [%]	Vol. I-L [%]	Vol. I-R [%]	Vol. II-L [%]	Vol. II-R [%]
1	2.5	80	74	91	96
2	5.9	84	75	85	96
3	6.9	86	78	85	93
4*	1.3	72	75	85	76

Table 5.2: Summary of the parameters set in the Super Daedalus(top) and of the acquisition dead time and percentage of volume active in the Super Daedalus trigger(bottom). For the last period (*) the Super Daedalus of the west Module have been enable in Induction2 instead of Collection.

been permanently excluded from the trigger. The first wires of the II-L crate instead weren't equipped for most of the time considered in this analysis, thus explaining the evident deficit of events. Both of the regions just mentioned are the so called "corner" crates, i.e. the angular crates which are sensitive to a smaller argon volume, due to geometrical reason. A second effect clearly visible is a gap of the last wires of the II-R chamber. reflecting an inversion of the wire sequence in the decoding algorithm. The effect of this inverted mapping is minimal on the event selection efficiency and on the measurement of the energy deposition.

Some other anomalous regions emerge from each chamber, for the events triggered with SD, and on the II-L chamber, for those triggered by PMT.

To understand this anomalies, the events depositing energy completely inside the anomalous region have been visually scanned, showing that the problem is linked to peculiar noise patterns, which affect both the SD trigger and the CEF, faking a genuine deposit of energy (fig.5.6). A similar situation has been found for the peak detected in the II-L chamber for the events triggered by PMTs, for which a peculiar noise pattern, likely related to the PMT activity, has been identified.

To overcome this problem, all the events that are completely contained into the noisy region of tab.5.3 have been excluded from this analysis. If for the I-L, I-R and II-R chambers, the noisy region is not bigger than an acquisition board, in the II-L view the noise extends up to one half of the chamber. This strong cut results in a loss of efficiency in the II-L chamber for this analysis, and a dedicated filtering algorithm is

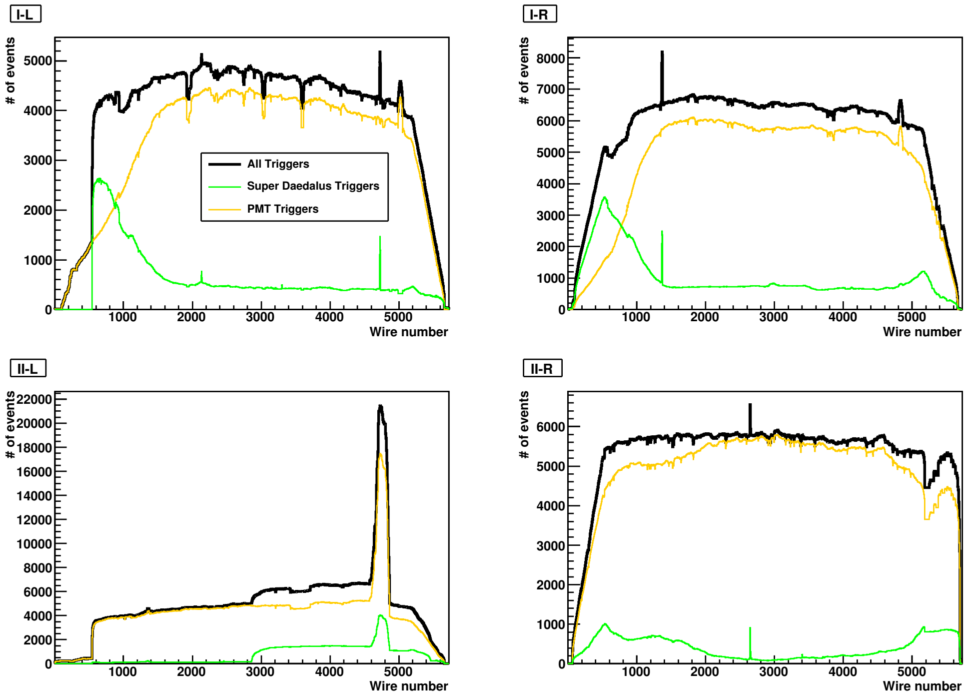

Figure 5.5: Wire occupancy of the events triggered by PMT (yellow) and SD(green) for 67 days of data taking.

Region	Trigger Source	Chamber	First Wire	Last Wire
1	SD	I-L	4715	4740
2	SD	I-R	1355	1380
3	SD	II-L	2860	5480
4	SD	II-R	2635	2660
5	PMT	II-L	4580	4870

Table 5.3: Noisy regions for the two trigger sources in all the chambers.

under study to reduce the impact of this problem.

After the application of the cut reported in tab.5.3, the spatial distribution of the events resulted much smoother in all the views(fig.5.7). It is worth noting that the events recovered by the SD trigger are concentrated on the southern corner of the western module, where one of the PMT of the I-R module has been turned off for noise problem.

A second comparison has been made on the deposited energy distribution of the events with different trigger sources, both chamber by chamber (fig.5.8) and summing the deposited energy on the two chambers of the same module (fig.5.9).

The chamber by chamber spectra show that the SD trigger recovers the PMT in-

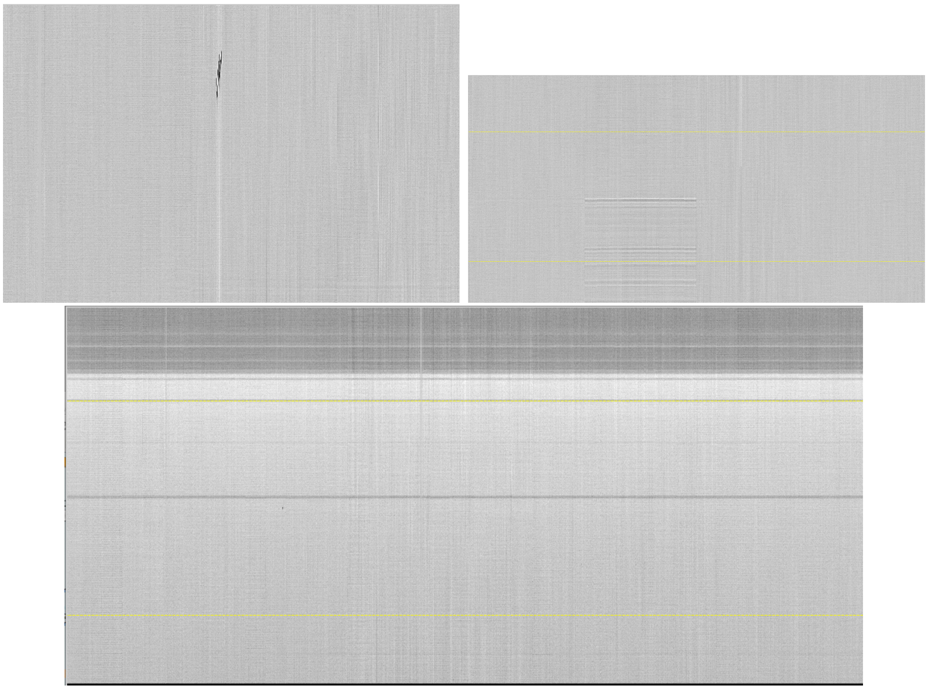

Figure 5.6: Examples of the behavior of the noise in region 4(top left), 5 (top right) and 3(bottom).

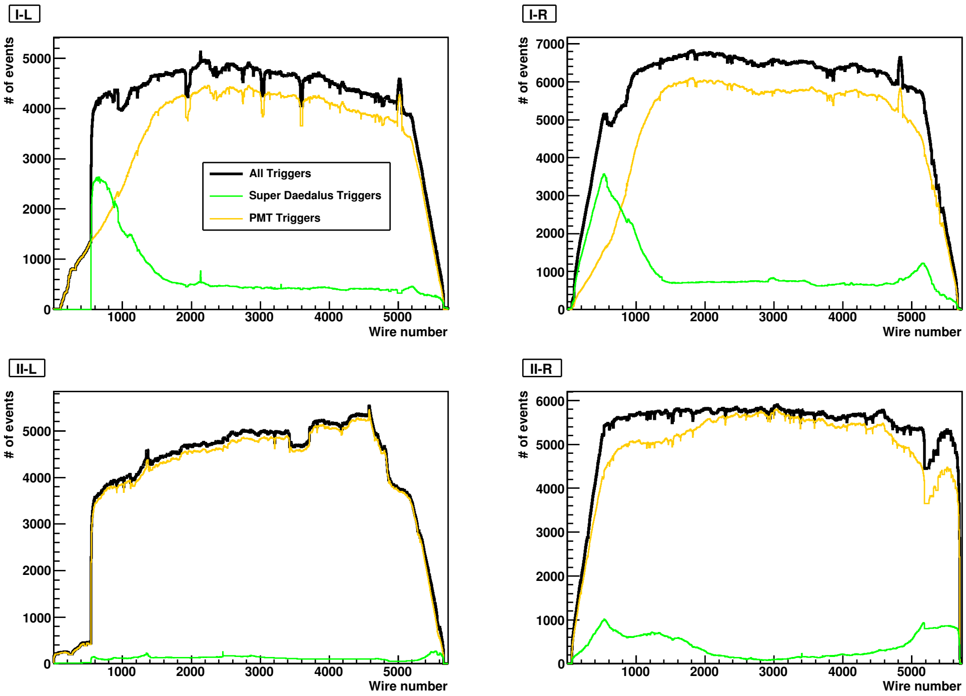

Figure 5.7: Wire occupancy of the events triggered by PMT (yellow) and SD(green) after the application of the cut for noisy regions.

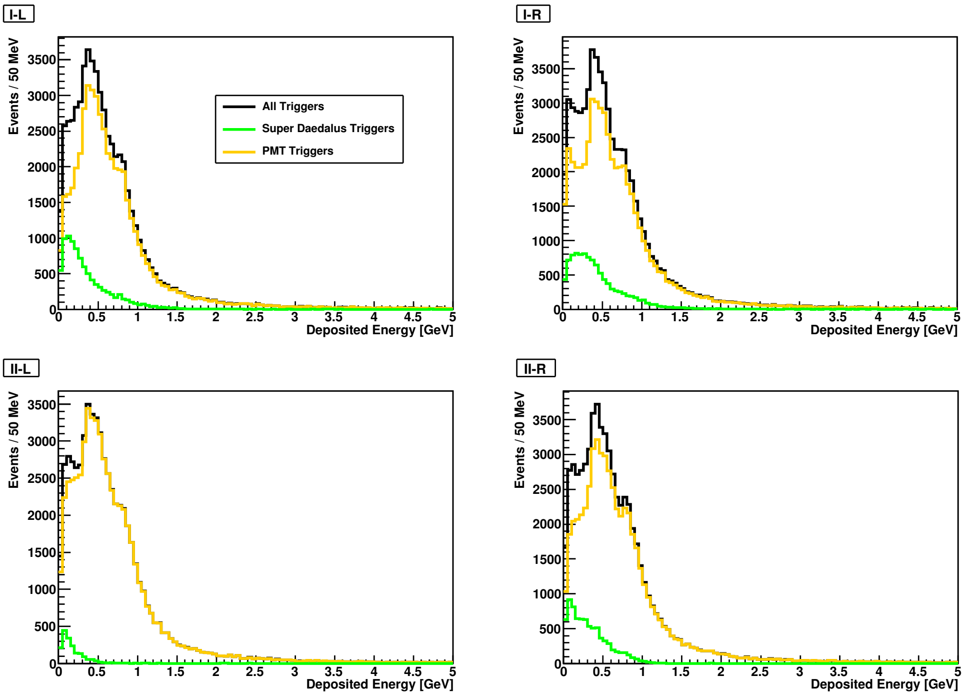

Figure 5.8: Energy distribution of the events triggered by PMT (yellow) and SD(green) for each chamber.

efficiency up to $\sim$ 1 GeV, with an evident increase on the region below 500 MeV, in particular for the two chambers of the western Module, which has less PMT. The energy distribution resulting from the sum of the different trigger sources results similar on all the chambers, with the exception of the low energy tail on the I-L chamber which exhibits a deficit when compared to the others. This can be explained by the fact that the southern region of the I-L chamber has a very high noise level, and the automatic veto is set for more than 90% of the time. In the same area, but in the opposite chamber, a PMT is turned off, so it is more likely for a low energy track on the I-L southern region not to fire the PMT of the I-R chamber. Such a track would not be recovered by the SD trigger, since it falls in a region that is often disabled for noisy region, and will therefore be lost. This explanation if reinforced by the spatial distribution of the I-L chamber, which shows a clear drop for the first wires (corresponding to the southern region).

The two spectra of the deposited energy per Module (fig.5.9) are in good agreement with each other, down to $\sim$ 150 MeV. At this energy the effect above mentioned on the distribution of the I-L module produce a drop on the event rate when compared

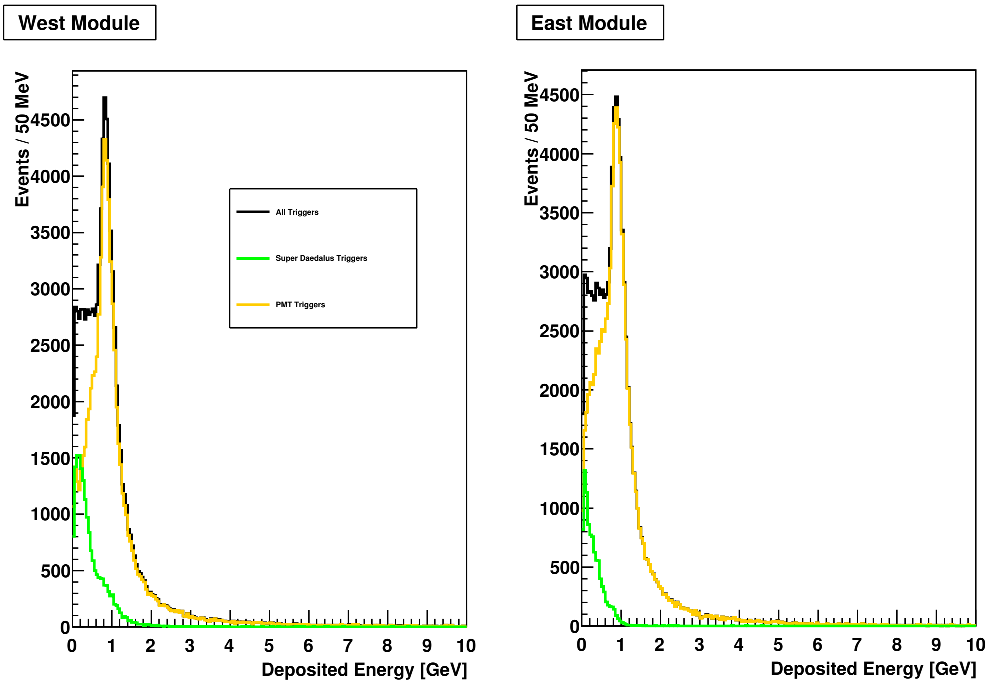

Figure 5.9: Energy distribution of the events triggered by PMT (yellow) and SD(green) for each Module.

to the eastern Module.

5.6 Comparison with MC expectations

To check the results obtained during this first phase of data-taking, 8991 cosmic rays events, reproducing the expected spectrum at LNGS for an exposition of almost two days, have been fully simulated with the FLUKA package. To have an homogeneous data set, only the third period of tab. 5.2 was studied.

The efficiency of the DR-slw algorithm has been evaluated on the MC data-sample, firstly with the assumption of a full SD coverage of the Collection views and then including the cuts related to the automatic veto. To better simulate the effect of the noisy crates, which were temporarily excluded from the trigger, the mean dead time for each crate during the running phase was measured. When analyzing a MC event, for every crate a random number, with a uniform distribution from 0 to 1, was generated; if the random number resulted higher than the mean fraction of veto for that crate, the corresponding region where analyzed, otherwise that portion of the event

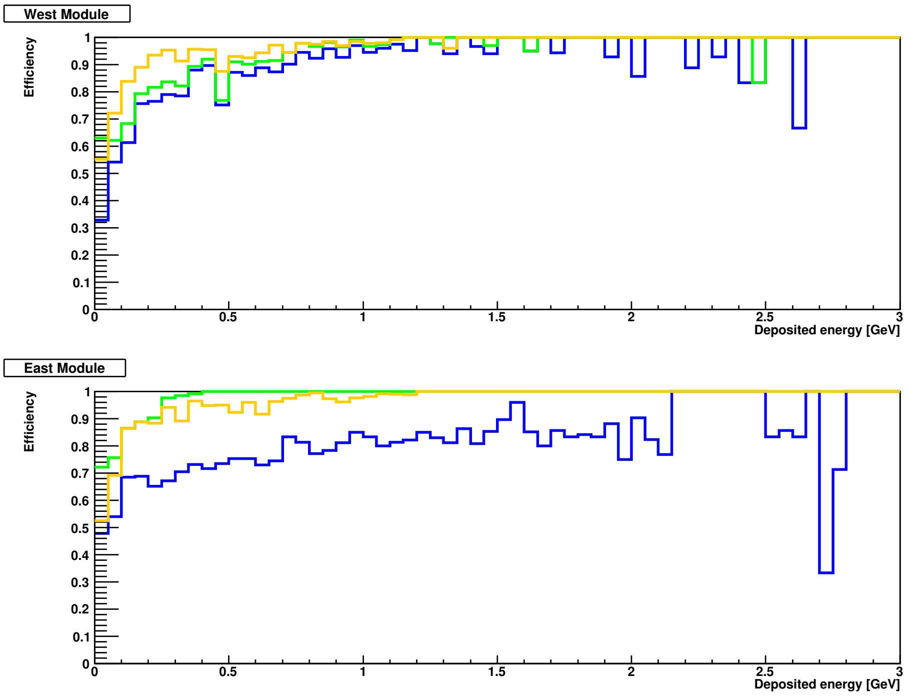

Figure 5.10: Cosmic ray trigger efficiency for SD without cuts (yellow) with cuts for automatic veto (blue) and for the OR of PMT + SD with cuts (green).

where ignored. Finally a third efficiency estimate has been done gathering the SD and PMT systems, requiring for each MC event at leas one of the two triggers. The results as a function of the deposited energy are reported in fig.5.10 for both he chambers. The efficiency over the whole spectrum has been estimated in 91.2% for SD without cuts, 78.9% for SD with cuts, and 91.8% for SD with cuts plus PMT. These numbers raise to 94.1%, 81.4% and 93.7% respectively when only the spectrum above 30 MeV is considered.

To compare the measured cosmic flux with the expectation from MC simulation, both the spectra have been normalized to the same exposure. For the MC data sample, the normalization factor is given by an exposure of 19.75 s for each MC event, while for the real data the exposure has been measured on the basis of the running time, defined as the time elapsed from the first to the last event acquired run by run, corrected by the acquisition dead time. In this analysis the event selection is based on the trigger mask, so that an event which was triggered with a PMT and subsequently recorded a SD pattern in the trigger mask, is now treated ad a SD trigger.

The first comparison has been made studying separately the behavior of the SD trigger in each chambers, by requiring the correspondence of the SD trigger mask with the deposited energy of each chamber. The same requirement has been applied for the MC events, which have been analyzed with the DR-slw filter, requiring at leas 1 GTO signal for each chamber with deposited energy above 30 MeV. The same constraints on the noisy region described in the previous section have been applied both to real data and to the MC simulations. The results, reported in fig.5.11, show a deficit on the measured spectrum with respect to the expected one, of $\sim$ 10% for each chamber. The same deficit reflects to the energy distributions of the events in the two modules, reported in fig.5.12. The evident reduction of the peak at $\sim$ 1 GeV observed in the eastern module is a consequence of the fact that almost one half of the II-L chamber is excluded from the acquisition for noise reasons. As a consequence, for all the events that are partially contained in the northern region of the II-L chamber only a part of the deposited energy will be detected, resulting thus in a spectrum distortion. The discrepancy observed at the $\sim$ 1 GeV peak, which were present also for the PMT triggers, is still not completely understood, and further investigations are required.

The Super Daedalus trigger is now taking data in steady condition, with a trigger active volume exceeding 90% and with a mean acquisition dead time below 1%. In this conditions the data taking will provide precious informations, which will allow the ICARUS collaboration to study the nucleon decay, with the perspective of extending the present limit for the $n \rightarrow e^- k^+$ and $p \rightarrow \pi^+ \overline{\nu}$. The additional trigger efficiency will also help to qualify the previously active PMT setup.

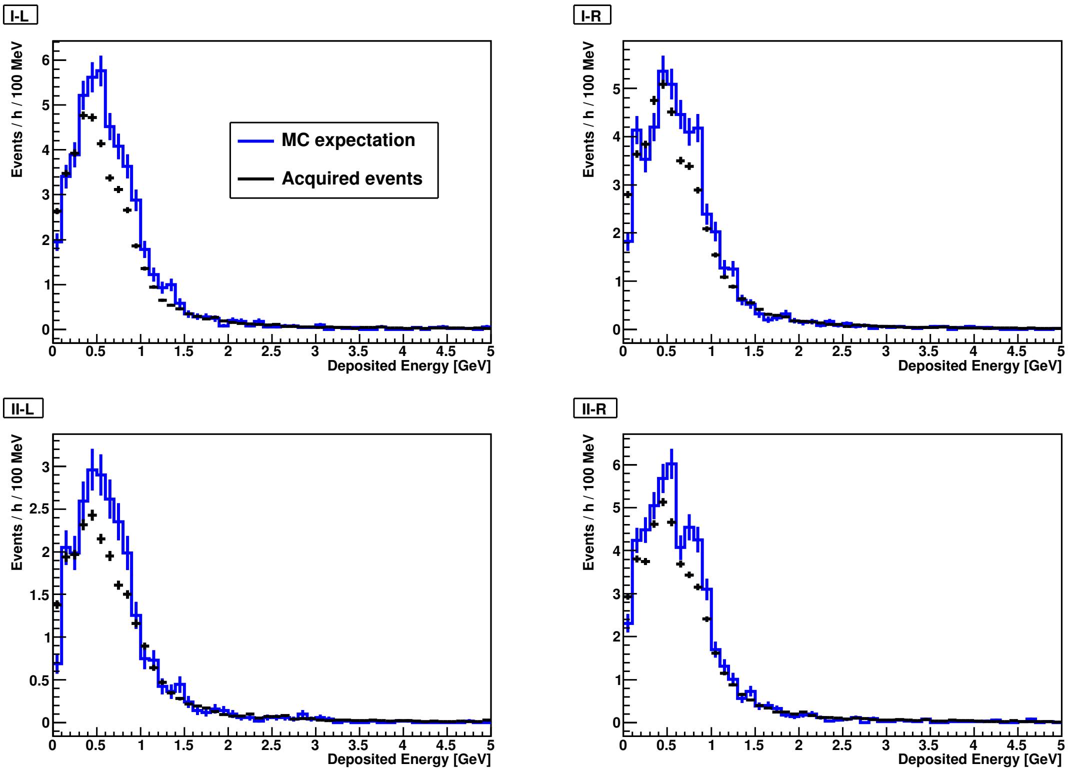

Figure 5.11: Comparison of the events triggered with SD with respect to the expectations on a chamber by chamber basis. A fraction of the events is missing in all the chambers.

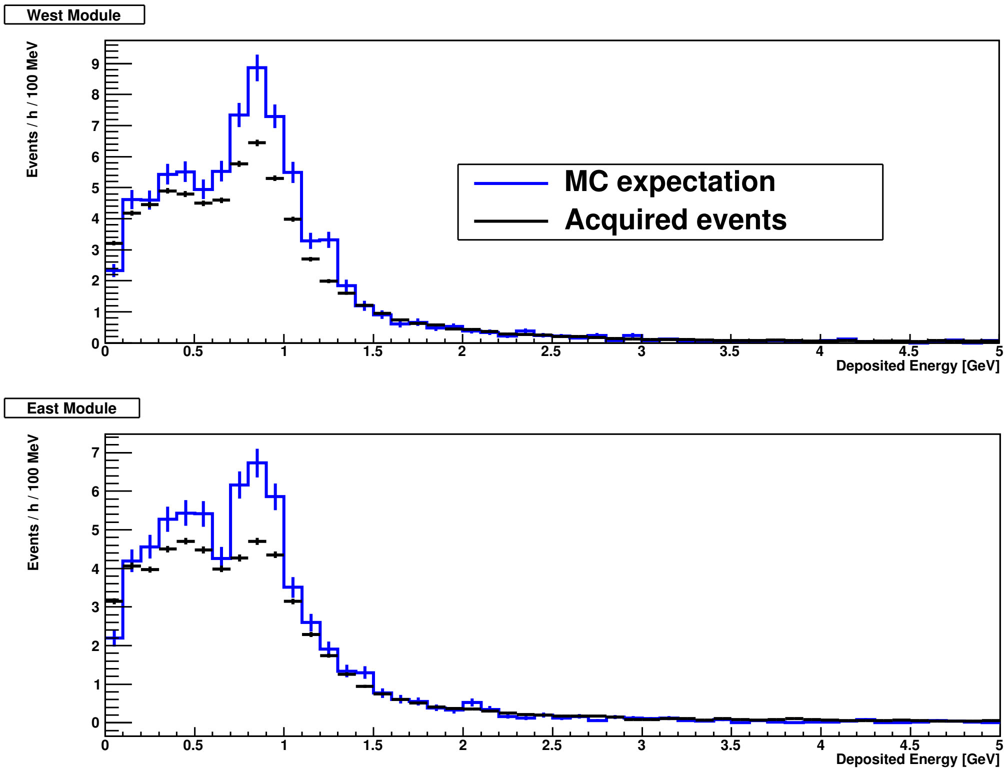

Figure 5.12: Comparison of the energy distributions of the events triggered with SD with respect to the expectations.

Chapter 6

Neutrino time of flight measurement on the CNGS beam

Neutrino time of flight measurements were triggered by the OPERA Collaboration announcement [36] of the surprising result indicating a superluminal propagation speed of CNGS neutrinos from CERN to LNGS.

Cohen and Glashow [37] argued that such superluminal neutrinos should lose energy by producing photons and e^+e^- pairs, through Z_0 mediated processes, analogous to Cherenkov radiation. The ICARUS Collaboration reported a negative result in the search for superluminal Cherenkov-like pairs inside its large LAr-TPC detector [38] exposed to the CNGS beam. No candidate event was found, setting a tight negative limit on $(v_\nu - c)/c$ of 2.5×10^{-8} at 90 % C.L. Moreover the ICARUS Collaboration performed a first time of flight measurement of neutrinos from CERN to LNGS with a 3 ns wide bunched beam shortly operated at the end of 2011 CNGS run. The result, $\delta t = tof_c - tof_\nu = 0.3 \pm 4.9_{stat.} \pm 9.0_{syst.}$ ns [39] was compatible with the simultaneous arrival of all events with speed equal to that of light, in a striking difference with the reported initial result of OPERA.

At the end of the 2011 CNGS bunched beam campaign, CERN and the LNGS experiments (Borexino, ICARUS, LVD, OPERA) agreed to perform a new dedicated campaign with the aim of improving the neutrino time of flight measurement significance. This new measurement was performed from May 10^{th} to May 24^{th} 2012 with the CERN-SPS accelerator operated in a dedicated bunched mode with $\sim 10^{12}$ p.o.t (protons on target) per spill [40]. The neutrino time of flight measurement consists in recording any neutrino induced interaction time at LNGS and relating it to the transit time of a proton bunch at a BCT monitor along the CNGS TT40 transfer tunnel at CERN, occurring ∼ 2.44 ms earlier. Precise geodetic estimation of the CERN-LNGS distance allows calculating the actual neutrino velocity.

The experimental measurements of the neutrino velocity with the ICARUS detector has been obtained combining the accurate determination of the distance and time of flight with the direct observation of either neutrino events inside the detector or neutrino associated muons from the surrounding rock [41]. The ICARUS results have been also confirmed by the other LNGS experiments [42, 43] in the 2012 CNGS bunched beam campaign.

6.1 The CNGS neutrino bunched beam

The CNGS proton beam structure for the 2012 neutrino time of flight run is shown in Figure 6.1. It was based on LHC-like proton extractions, with a single extraction per SPS super-cycle (13.2 s), 4 batches per extraction separated by 300 ns, and 16 proton bunches per batch separated by 100 ns; each bunch had a narrow width of ∼ 4 ns FWHM (1.8 ns rms). This very tightly bunched beam structure allowed a very accurate neutrino time of flight measurement on an event-by-event basis. A total of $\sim 1.8 \times 10^{17}$ p.o.t. were delivered to CNGS allowing the collection of several tens of neutrino induced events.

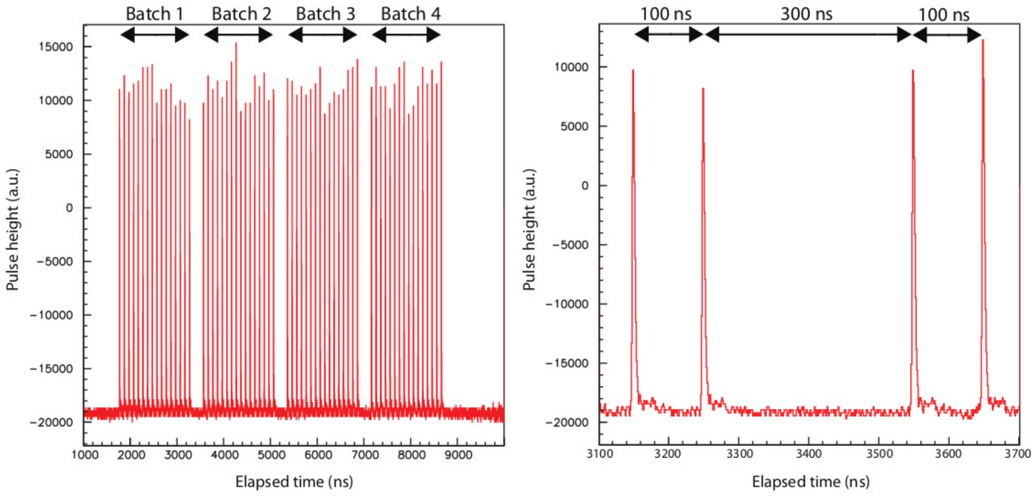

e

Figure 6.1: CNGS proton beam structure dedicated to neutrino time of flight measurement. Typical width of each proton pulse is ∼ 4 ns (FWHM).

6.2 Synchronization between CERN and LNGS

A schematic picture of the timing system layout, including all delays is shown in Figure 6.2. The origin of the neutrino velocity measurement is referred to the Beam Current Transformer (BCT) detector (BFCTI.400344), located 743.391 ± 0.002 m upstream of the CNGS neutrino target.

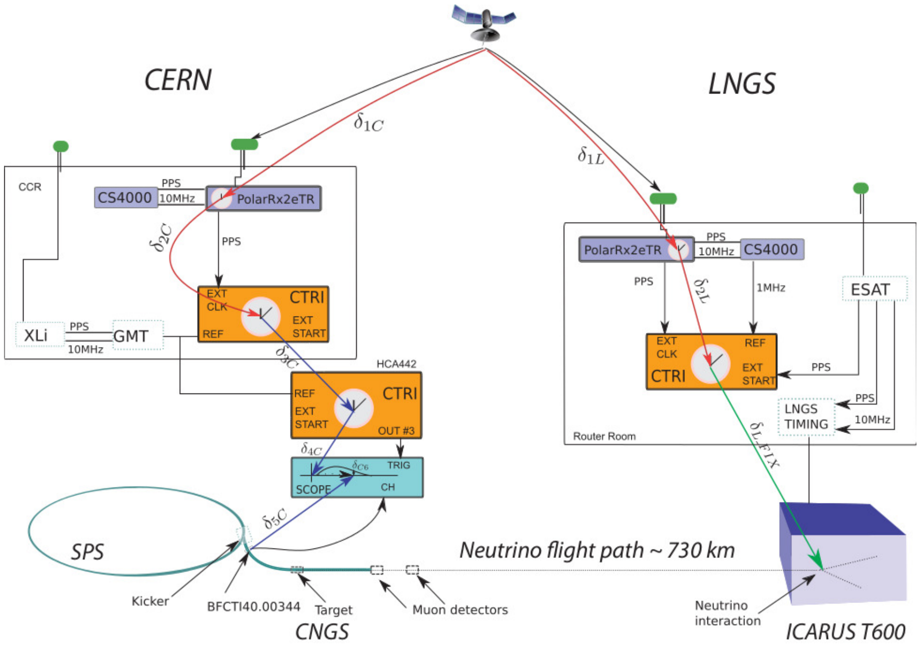

Figure 6.2: Schematics of the CERN-LNGS timing synchronization. The origin of the neutrino time of flight measurement is at BFCTT40. For ICARUS, the arrival reference point is the T600 entry wall.

The proton beam time-structure at the BCT is recorded by a 1 GS/s Wave Form Digitiser (WFD) Acqiris DP110, triggered by the SPS kicker magnet signal. At every extraction, the BCTFI.400344 waveform is stored into the CNGS database. Every acquisition is time-tagged with respect to the SPS timing system, associating each neutrino event at LNGS to a precise proton bunch.

The absolute UTC timing signal at LNGS is provided every second (PPS) by a GPS system ESAT 2000 disciplining a Rubidium oscillator, operating on the surface Laboratory. A copy of this signal is sent underground every ms (PPmS) and used in ICARUS to provide the absolute time-stamp to the recorded events.

In order to improve the ∼ 100 ns time accuracy of the standard GPS at CERN and LNGS, the OPERA collaboration and CERN have installed, both at CERN and LNGS, two new identical systems composed of a GPS receiver for time-transfer applications Septentrio PolarRx2e operating in "common-view" mode and a Cs atomic clock Symmetricom Cs4000. The Cs4000 oscillator provides the reference frequency to the PolarRx2e receiver, and a CTRI device logs every second the difference in time between the 1PPS outputs of the standard GPS receiver, that drives the SPS timing system (XLi in Figure 6.2) and of the more precise PolarRx2e, with 0.1 ns resolution. The two systems were calibrated, resulting in a precision of ±2.0 ns.

The timing signal (PPmS), distributed by the LNGS laboratory, consists of a TTL positive edge (3 ns rise time) sent out every ms and followed, after 200 μs, by the coding of the absolute time related to the leading edge. The delay of this signal, generated in the external laboratory and sent to the underground hall B via $\sim$8 km fibre optics, is periodically calibrated following a double path procedure.

For the 2012 CNGS bunched beam run, additional CERN-LNGS synchronization systems have been set-up.

Two new additional Septentrio PolarRx4 GPS receivers, optimized for time-transfer applications, have been installed at CERN and LNGS. As the PolarRx2e receivers, they operate in "common-view" mode and are connected to the same Cs atomic clocks Symmetricom Cs4000 used to provide the reference frequency to the PolaRx2e receivers. Their inter-calibration is stable within ±2.0 ns.

Both the new PolarRx4 and the old PolarRx2e synchronization paths are connected to the DAQ systems at CERN and LNGS, through the "Classic" 2011 protocol. In addition to it, a new independent system for timing distribution was deployed both at CERN and at LNGS. It is based on a recent, still under development, open source protocol, called "White Rabbit" (WR) [44], whose main purpose is to constantly and accurately monitor the propagation delay of any signal along the optical path, connecting all Nodes (PC's provided with WR hardware interface and running the WR protocol firmware) of the WR system. The WR system is expected to intrinsically correct for any change of the propagation chain delay, thus avoiding the need of periodic calibrations of the optical fibres described in the previous section. Any Node participating in the WR system is thus phase-locked with all the others, with accuracy and stability much better than one ns. The WR protocol allows the distribution of timing signals at various frequencies (e.g. PPS, PPmS) as well as the time-stamping of any pulse generated by the DAQ systems connected to WR Nodes.

In addition to the above set-up, the Borexino collaboration implemented at LNGS a new timing system (High Precision Timing Facility, HPTF) [45], available also to the ICARUS experiment, based on an independent additional PolarRx4 GPS receiver. This installation, located at the LNGS outside laboratory, provides the time stamping of signals propagated from the experiments along the optical fibre-bundle connecting the underground and the external Labs.

6.3 Neutrino time of flight measurement with ICARUS

The layout of the ICARUS T600 readout system specifically designed for the neutrino time of flight measurement is shown in Figure 6.3.

A fraction of the direct PMT signals ($\sim 1/10$) is extracted before the pre-amplification stage; the sum of these signals for each PMT horizontal array is sent to a dedicated DAQ system.

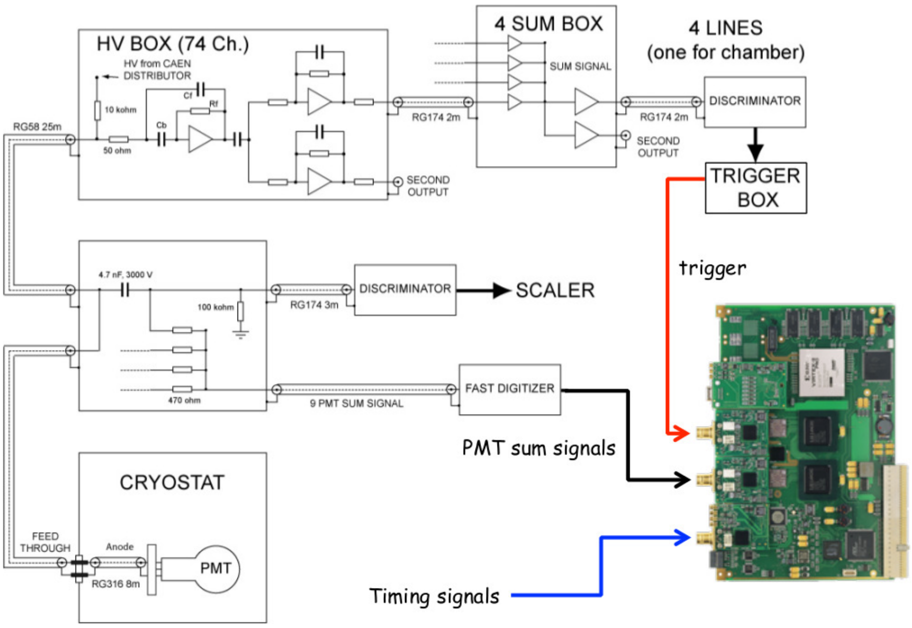

Figure 6.3: Schematics of the 2012 ICARUS PMT-DAQ specifically designed for neutrino time of flight measurement. The latter is replicated through a dedicated fan-out setup and in order to be sent to the HPTF and to WR facilities for time stamping. The jitter between replicas has been certified to be of the order of 0.1 ns.

This additional PMT-DAQ system, derived from the DAQ developed for the WArP [46] experiment, is based on six 2-channel, 8-bit, 1-GHz AGILENT AC240 digitizer boards. The eight PMT-Sum signals are continuously read out and stored in a circular memory buffer of a depth of 8 kB/channel, sampled at 1 GHz. The full dynamic range of the digitizers can be set as low as 50 mV, allowing to get a sensitivity of about 2 phe/ADC count. The digitizer boards are organized in two crates, connected to the event building computers and to data storage via optical link. All digitizers within the same crate are synchronized with each other at a 10 ps level.

At each CNGS trigger, the content of the circular buffer is frozen and additional data are read out for a total memory depth equivalent to 1.4 ms (slightly more than a full LAr-TPC drift time to include all possible scintillation signals produced along with the drifting ionization charge) and stored in a second local memory buffer. The content of all buffers is then transferred to the ICARUS data storage. Internal time stamping available in the digitizers is also stored allowing synchronization with the associated event imaging.

Several TTL timing signals are also recorded: the ESAT PPmS, a 2 kHz synchronization pulse from the WR system in phase with the related PPS, a pulse generated in the ICARUS trigger box at trigger level. The latter is replicated through a dedicated fan-out setup and in order to be sent to the HPTF and to WR facilities for time stamping. The jitter between replicas have been certified to be of the order of 0.1 ns. All these signals allow defining an absolute time for the PMT-DAQ digitizers in the time bases related to the four different timing systems. Moreover, the 2 kHz WR signal allows monitoring the stability of the digitizer frequency (at a level better than 1 ppm). A comparison of the WR time stamp and the 2 kHz signal allows also monitoring the stability of the WR protocol.

The synchronisation between the two PMT-DAQ crates is ensured by the ESAT PPmS signal which is send simultaneously to both crates. The jitter between the two copies of the ESAT PPmS signal has also been certified to be of the order of 0.1 ns.

The position of the timing signals along the recorded waveforms is taken, by interpolation, at the signal leading edge with the same threshold as that used in the related timing systems for time stamping and in any calibration procedure. The time of the PMT-Sum is taken at the onset of the related signal, thus providing the arrival time of the earliest scintillation photons. An example of these signals is shown in Figure 6.4.

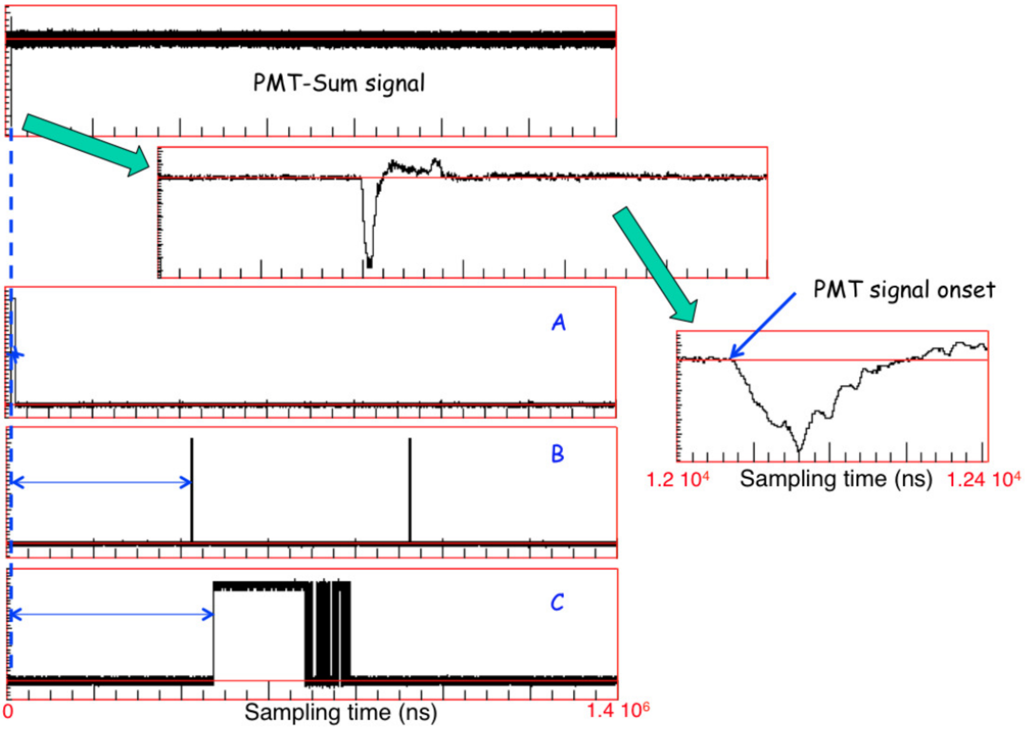

Figure 6.4: Example of signals recorded on the ICARUS PMT-DAQ: (A) TTL signal generated in the ICARUS trigger box (5 ns front edge, 10 μs wide): also sent to HPTF and WR-DAQ for time stamp; (B) 2 kHz signal from WR fine-delay (1 μs wide, 3 ns front edge): defines absolute time in WR time bases and monitors Acqiris time stability; (C) 1 kHz (PPmS) ESAT timing signal (200 μs wide, 3 ns front edge, followed by time encoding): defines absolute time in LNGS time base.

6.3.1 Calibration of the ICARUS PMT signal propagation

In order to measure the neutrino arrival time in the ICARUS detector, the propagation time of the scintillation light signals from the PMTs to the AC240 boards, including the transit time within the PMTs, the overall cabling ($\sim$ 44 m) and the delay through the signal adders, have been calibrated.

The propagation along the cabling has been measured with an accuracy of $\sim$ 0.5 ns by means of standard reflection techniques on sharp signals (few ns rise-time) with a 1 GHz bandwidth oscilloscope. Being the PMT transit time a purely geometrical and electrostatic effect, its measurement was carried out in laboratory tests at room temperature on an ETL 9357FLA spare PMT, covered with TPB wavelength shifter. The resulting estimated error of 1 ns is mainly related to the oscilloscope sampling frequency of 1 GHz.

The additional delay in the PMT transit time, introduced by the wavelength shifting process in the T600 detector, is negligible since the TPB excitation time has been measured to be less that 35 ps. Moreover, the TPB 1.7 ns exponential dis-excitation time only affects the photon arrival spread and not the PMT signal onset measurement.

6.3.2 Calibration of timing signals

For the classic 2011 timing system and the HPTF facility, the propagation delays of the signals along the $\sim$ 8 km optical fibres connecting the external laboratory and the underground halls have to be determined. The method consists in measuring the time difference Δt and time sum Σt of the signal propagation along the usual path and an alternative one consisting a spare fibre. For the ESAT signal:

- in the first configuration the 1PPS output of the ESAT-2000 GPS receiver was converted into an optical signal, sent underground via the spare fibre and converted back into electrical. The difference in the propagation delays, between this signal and the 1PPmS output of the ESAT-2000 GPS propagated over the standard path, was measured underground taking as a reference the middle height of the rising edge;

- in the second configuration the 1PPmS output of the ESAT-2000 GPS, at the end of the usual path underground is sent back to the external laboratory, where it is compared with the 1 PPS signal, taking as a reference the middle height of the rising edge.

The used optoelectronic chain is kept identical in the two cases by simply swapping the receiver and the transmitter between the two locations. Furthermore the jitter of the phase difference between the 1PPS and the 1PPmS outputs of the ESAT-2000 GPS receiver was checked to be negligible ($\lesssim 0.25$ ns).

This procedure was applied several times before and after the 2012 bunched beam run, obtaining a result of 41905.3 ± 2.0 ns where the error takes into account the jitter in the various measurements and the observed response variation of the receivers electronics and of the signal propagation time along the fibre mainly due to temperature changes. An equivalent method has been used for the optical fibre transferring the ICARUS trigger related pulse to the HPTF (45260.8 ± 1.0 ns); the smaller associated error is mainly due to the improved receivers electronics.

The WR timing system does not need this calibration, which is intrinsically and continually performed by the WR protocol. Laboratory tests in a thermalized chamber have shown that variations in the WR system are smaller than 300 ps peak-peak for the -20°C to 40°C range.

6.4 Geodetic measurement of the CERN-LNGS distance

The distance between the CNGS target focal point and the LNGS experiment has been remeasured under the responsibility of the Politecnico di Milano just before the 2012 bunched beam run, following a dedicated geodesy campaign, resulting in an estimated accuracy of 3.7 cm both at CERN and LNGS in the common geodetic reference frame.

As a result, he baseline considered for the measurement of the neutrino velocity is then 731221.95 ± 0.09 m. Therefore, the expected time of flight for $v = c$ is 2439096.08 ± 0.3 ns, including the 2.2 ns contribution due to earth rotation (Sagnac effect).

6.5 Data analysis

During the 2012 two weeks of data taking with the CNGS in bunched mode, the ICARUS T600 detector collected 25 beam-associated events, consistent with the CNGS delivered neutrino flux of 1.8×10^{17} p.o.t.

The events consist of 8 neutrino interactions (six CC and two NC) with vertex contained within the ICARUS fiducial volume and 17 through going muons (one of which stops within the LAr active volume) generated by CNGS neutrino interactions in the upstream rock. Events in the standard ICARUS DAQ and the PMT-DAQ have been associated through their common absolute time-stamp (Figure 6.5).

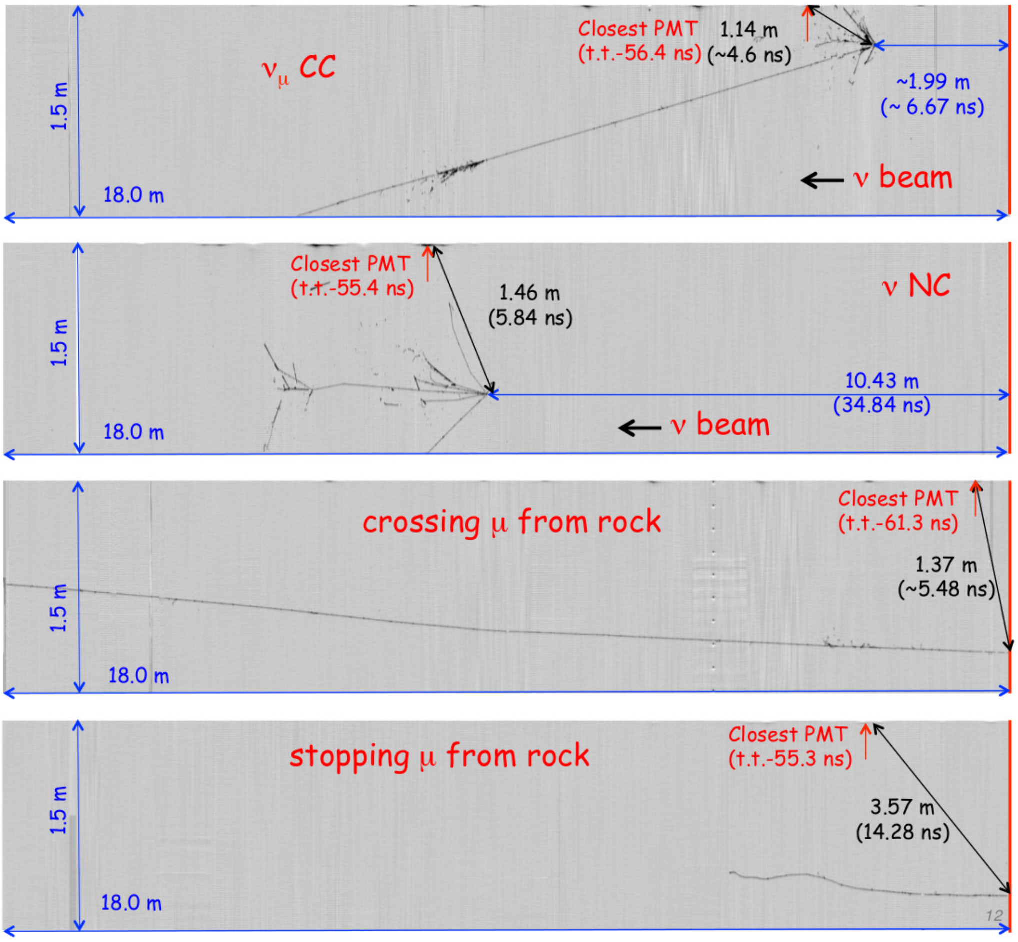

Figure 6.5: Examples of different event topologies in the ICARUS LAr-TPC from the 2012 CNGS bunched beam run. A 2D view ("Collection" wire plane) is shown. For each event the distance from the "ICARUS reference entry point" (red line on the right of the image) is reported as well as the photon path the nearest PMT and the associated transit time (t.t.) in the PMT itself.

For all the collected events, the visual scanning and 3D reconstruction are exploited to determine the distance of the interaction vertex from the ICARUS "reference entry point" and to quantify the shortest path of the scintillation light to the nearest PMT. Given the "millimeter" space resolution of the ICARUS LAr-TPC, both the above corrections are measured with sub-ns accuracy.

The actual neutrino time of flight is measured on an event-by-event basis: (1) the transit time of the proton beam bunch at the BCT in the CERN time-base is used as starting time; (2) the neutrino arrival time is taken at the ICARUS "reference entry point" in the LNGS time base; (3) the alignment of the LNGS and CERN time bases is calculated following the different synchronization paths available for the 2012 run.

The final neutrino time of flight measurement is obtained as weighted average over all possible timing paths where the weights are proportional to the related systematic uncertainties. The overall systematic error derived within the averaging procedure is ~ 2.39 ns.

The difference between neutrino time of flight (tof$_\nu$) from the BCT to the ICARUS "reference entry point" and the expected time of flight based on the speed of light (tof$_c$ = 2439096.1 ns) is shown in Figure 6.6. The resulting value $\delta t = tof_c - tof_\nu = 0.10 \pm 0.67_{stat.} \pm 2.39_{syst.}$ ns, is fully compatible with the neutrino propagation at the speed of light. The corresponding deviation of the neutrino velocity from the speed of light is $\delta(v/c) = (v_\nu - c)/c = (0.4 \pm 2.8_{stat.} \pm 9.8_{syst.}) \times 10^{-7}$, excluding neutrino velocities larger than the speed of light by more than $1.35 \times 10^{-6}c$ at 90% C.L..

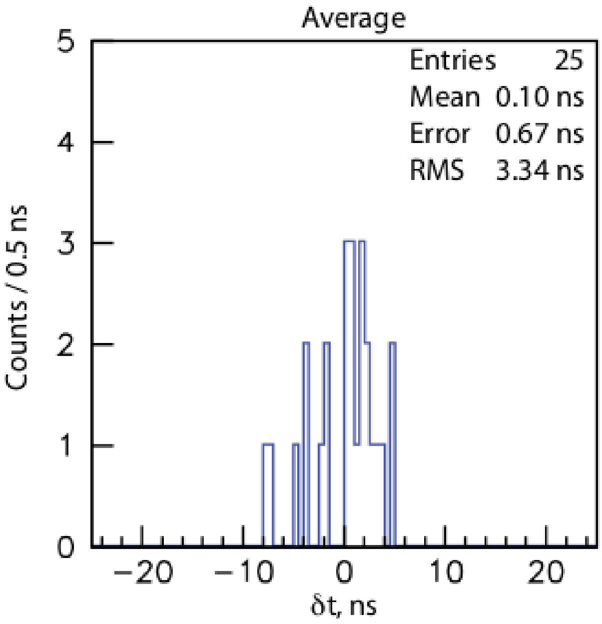

Figure 6.6: Event distribution in ICARUS T600 for δt = tof$_c$ - tof$_\nu$, according to the averaging procedure of all synchronisation paths described in the text.

Chapter 7

LAr TPC for sterile neutrino searches

As already observed in chapter 2, a series of results arose from several experiments that appear anomalous in the standard 3 neutrino framework , but which may be interpreted in a unique framework as the consequence of the presence of a forth sterile neutrino family.

The first anomaly, and up to date the most significant, is represented by the result of the LSND experiment, which has observed a $\overline{\nu}_e$ CC interaction appearance in a $\overline{\nu}_\mu$ neutrino beam [47]. The measurement of this excess could be explained as a $\overline{\nu}_\mu \rightarrow \overline{\nu}_e$ oscillation, ruled by a mass square value of ~ 1 eV. The anomaly of this results appears clear when compared to the other two, much smaller, value of Δm^2 measured by solar and reactor experiments $\Delta m^2_{sol} = 7.50 \pm 0.20 \times 10^{-5} eV^2$ and by the atmospheric and accelerator experiments $\Delta m^2_{atm} = 2.32^{+0.12}_{-0.08} \times 10^{-3} eV^2$[48]. The presence of such an high mass difference could not fit the three neutrino scenario and must call for an additional neutrino family to accommodate.

On the other hand, the results from Large Electron Positron collider (LEP) at CERN on the measurement of the decay width of the Z boson, have set a tight constrain of $N_\nu = 2.92 \pm 0.05$ to the number of active neutrino families with a mass below one half of the mass of the boson [48]. Any eventual additional neutrino in the ~ 1 eV mass range would therefore be decoupled to the Z boson, i.e. it wouldn't interact via weak interaction resulting thus sterile.

A series of results, such as the re-evaluation of all reactor experiment results, revisited after a new calculated neutrino flux, and the calibration campaigns of radiochemical experiments with high intensity neutrino sources , have recently reinforced the hypothesis of the existence of a fourth sterile neutrino family, in a region of mass squared compatible with the one found by LSND $\Delta m^2_{sterile} \sim 1$ eV.

The scenario that emerges from this results appears incomplete and unclear, requiring new and unambiguous experimental results to clarify the existence of any eventual forth neutrino family.

In the following the main experimental indications and constraints on the presence of an additional sterile neutrino will be summarized. Afterward, it will be described a possible experimental setup to investigate the presence of a forth sterile neutrino, based on the LAr TPC technology, proposed at CERN in 2011, and to be held at CERN-SPS starting from 2016. Finally the first electronic R&D held at Padua University will be described together with the next steps foreseen in view of the implementation of a completely new read-out architecture for LAr TPCs.

7.1 ν_e appearance sterile searches: checking the LSND results

The results of all the experiment pointing to the presence of a sterile neutrino can be divided into two groups, according to the measurement performed. The accelerator experiments, such as LSND and MiniBooNE, look for a ν_e ($\overline{\nu}_e$) excess, or its absence, in a ν_μ ($\overline{\nu}_\mu$) beam over the expected background from beam contamination. The electron neutrino appearance is therefore correlated with a $\nu_\mu \rightarrow \nu_e$ ($\overline{\nu}_\mu \rightarrow \overline{\nu}_e$) which, in the 4 neutrino scenario, is ruled by the mass difference $\Delta m^2_{sterile}$ and by two terms of the mixing matrix, namely $U_{4,\mu}$ and $U_{4,e}$.

On the other hand, the results of the experiments on low energy electron neutrinos and anti-neutrinos, such as reactor experiments and Gallium experiments exposed to Mega-Curie sources, are pure disappearance measurement, as they can only provide the electron neutrino survival probability, which in the 4 neutrino scenario is a consequence of the $\nu_e \rightarrow \nu_s$ oscillation and is linked to $\Delta m^2_{sterile}$ and $U_{4,e}$, being the oscillation driven by θ_{13} negligible in this L/E range.

Even if the results of the two groups of experiments may be interpreted in the same scenario of one, or more, additional sterile neutrinos, it is important to distinguish between the two experimental approaches, both because in principle they can be due to different unknown phenomena,and because, they would provide different informations on the elements of the new neutrino mixing matrix.

LSND is a neutrino detector constituted of 167 ton of liquid scintillator, which has been running from 1993 to 1998 on the neutrino beam extracted from the LMPF accelerator. An exhaustive description of the setup can be found e.g. in [**?**] The high intensity, low energy muon neutrino flux were generated mainly by the decay at rest of π^+, produced by an intense proton current of 1mA at 798 MeV hitting a water target. The $\overline{\nu}_e$ contamination, which is kept at the level of 8×10^{-4} of the $\overline{\nu}_\mu$ flux in the $20 < E_\nu < 52.8$ MeV energy range, and is mainly due to the decay of π^- and μ^-, being the production of K or heavier mesons negligible for these proton energies.

The $\overline{\nu}_e$, flux were measured via the inverse β decay, $\overline{\nu}_e p \rightarrow e^+ n$, which produces a clear two-fold signature of a positron with a 52.8 MeV endpoint followed by the detection of a 2.2 MeV γ from neutron capture on free protons.

After an event selection, based on the positron energy, the distance between positron and neutron detection, and the time interval between the positron detection and the γ detection, LSND observed 86 events in an energy window of 20 MeV $< E_e$ $<$ 60 MeV. This number must be compared to the event rate for beam off background, 36.9±0.7, and for the background relate to the $\overline{\nu}_e$ beam contamination (linked to μ^+ and π^+ decay),which gives a contribution of 16.9±2, resulting in an event excess of $32.2 \pm 9.4 \pm 2.3$, the distribution as a function of L/E_ν being given in 7.1.

To check the LSND results, a second experiment, MiniBooNE has been built to detect the neutrino beam produced at FNAL. The experiment run both with neutrino and antineutrino focussing, studying the $\nu_\mu \rightarrow \nu_e$ and the $\overline{\nu}_\mu \rightarrow \overline{\nu}_e$ oscillations. The event excess observed in the two running phases, reported in [49], has shown an incompatibility at 3.8σ of C.L. from the value expected for no-oscillation. The combined result from the two phases is in good agreement with that from LSND (fig.7.2), indicating a new mass square difference in the range $0.01 < \Delta m^2 < 1.0 eV^2$.

If, on one hand, the LSND and MiniBooNE results have proven an evident anomaly in the $\nu_\mu \rightarrow \nu_e$ and $\overline{\nu}_\mu \rightarrow \overline{\nu}_e$ which may be interpreted as a consequence of an additional mass square of the order of $\Delta m^2 \sim 1.0 eV^2$, on the other several other experiments gave a null result, strongly constraining the allowed region in the parameter space.

The strongest constrain set by an experiment at the accelerator is given by KARMEN, a segmented liquid scintillator detector, of 56 ton of total mass, exposed to the ISIS ν_μ beam. The event signature is the same as for LSND, a double fold coincidence

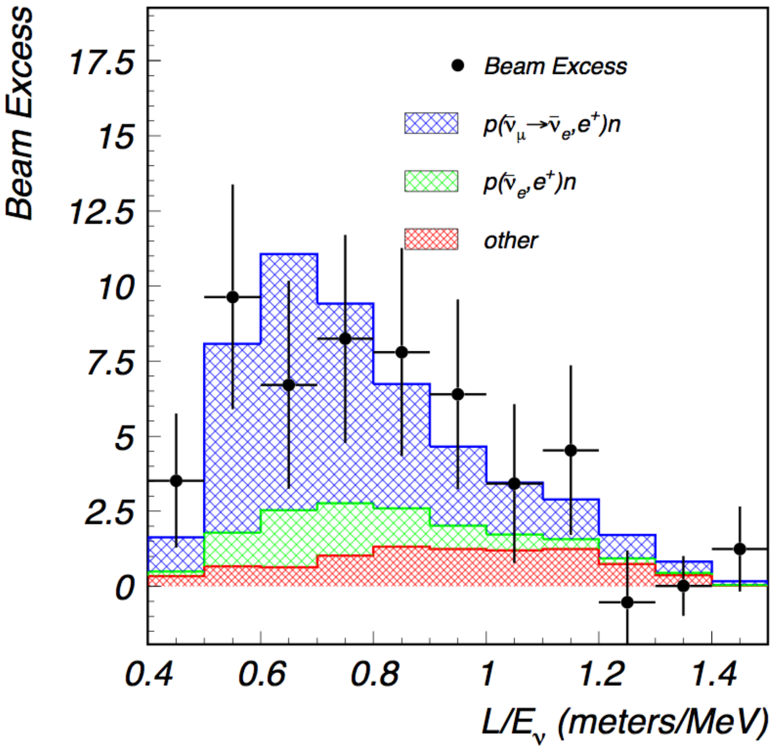

Figure 7.1: Distribution of the events recorded by LSND for R > 10 and 20 MeV < E_e 60 MeV.

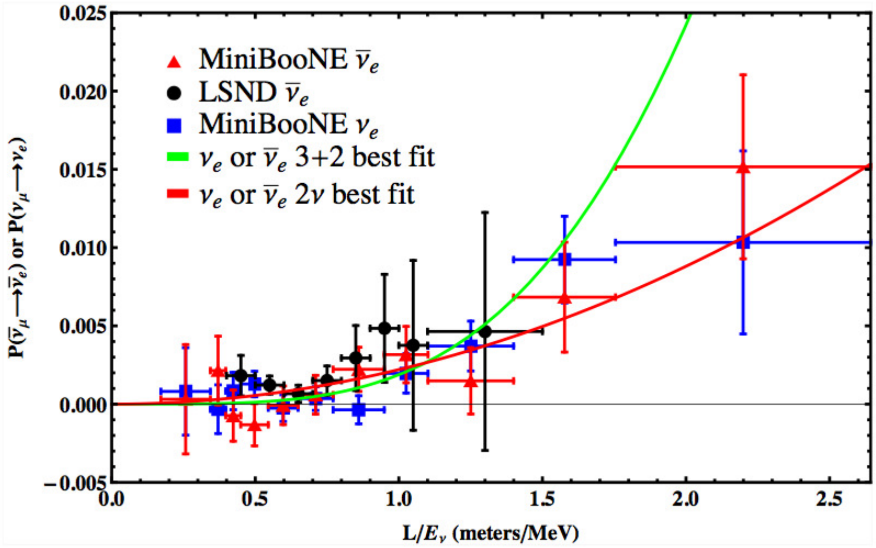

Figure 7.2: Trend of the oscillation probability as a function of L/E for the two phases of MiniBooNE and for LSND. The best fit for a 2 neutrinos simplified scenario, as well as for the 3 active + 2 sterile hypothesis is also shown.

of a prompt positron signal followed by the γ signal from neutron capture. A total of 15 events have been collected by KARMEN, in perfect agreement with the background expectation of 15.8±0.5 events. The non observation of any $\nu_\mu \rightarrow \nu_e$ transition, exclude all the LSND region $\Delta m^2 > 10eV^2$, but remains compatible with the region $\Delta m^2 < 2eV^2$ (fig. 7.3).

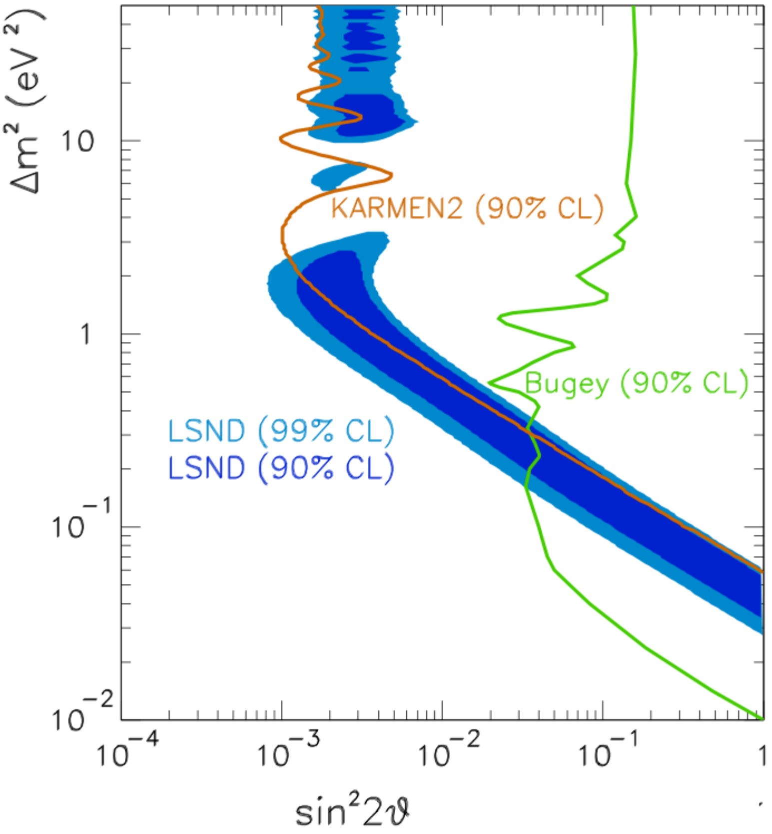

Figure 7.3: $sin^2 2\theta, \Delta m^2$ oscillation parameters fit from LSND compared with the area excluded by KARMEN and Bugey reactor experiment.

7.2 ν_e disappearance sterile searches: Reactor and Gallium anomaly

The nuclear reactors have played an important role in the study of neutrino physics, from the neutrino discovery to the latest results on θ_{13}, as they constitute a powerful source of an intense and pure $\overline{\nu}_e$ flux. Being the neutrino energy below the threshold required for the production of any charged lepton other than electron, the reactor based experiments are always disappearance measurements, described by:

$$P_{ee} = 1 - \sin^2 2\theta \sin^2 \left(\frac{\Delta m^2 L}{2E} \right) \tag{7.1}$$

In the attempt for a precise prediction of neutrino flux in view of the first phase of the Double Chooz experiment, the Saclay neutrino group has performed a re-evaluation of the neutrino reference spectrum, with the aim to reach an accuracy of few percent on the prediction of the $\overline{\nu}_e$ flux. The resulting spectrum has revealed some systematic biases on the neutrino flux prediction of the former reference model. The net effect of this re-evaluation results in a $\simeq 3\%$ increase of the predicted emitted spectrum[50].

A second effect that tends to increase the predicted $\overline{\nu}_e$ interaction rate, is the recent update of the value of the mean neutron lifetime τ_n. The shorter value of the τ_n reported in [23] has the effect of increasing the interaction rate expected for reactors experiments, being the cross section for inverse beta decay $\overline{\nu}_e p \rightarrow e^+ n$ inversely proportional to the neutron mean lifetime.

Both the above mentioned processes affect all the reactor neutrinos experiments in the same way, with a net effect of increasing the expected interaction rate. A comprehensive review of the results obtained by the main reactor experiments with a baseline < 100, i.e. in a L/E region where the oscillation related to θ_{13} is negligible, has been done in [51]. By taking into account the correlations of the systematics of the different experiments, the mean ratio of the rate observed to the rate predicted has been averaged both for the old antineutrino spectrum, resulting in $R_{old} = 0.980 \pm 0.024$, and for the new value of the antineutrino spectrum, resulting in $R_{new} = 0.927 \pm 0.023$ (fig. 7.4).

The deficit seen by the reactors experiment, shown as a function of L/E in fig.7.5, may be interpreted as the effect of a forth sterile neutrino, with parameters at best combined fit of $\Delta m^2 = 2.4 eV^2$ and $\sin^2 2\theta = 0.14$, rejecting the non-oscillation hypothesis at 2.9σ of confidence level.

Another “anomaly” which may be explained by the presence of a fourth neutrino, is represented by the results obtained during the calibration phases of the radio-chemical experiments based on gallium. Both the GALLEX and SAGE experiments have been exposed to monochromatic electron neutrino flux, provided by intense ^{51}Cr and ^{37}Ar

radioactive sources placed inside the detectors.

The interaction rate measured by the two detectors have been compared to the

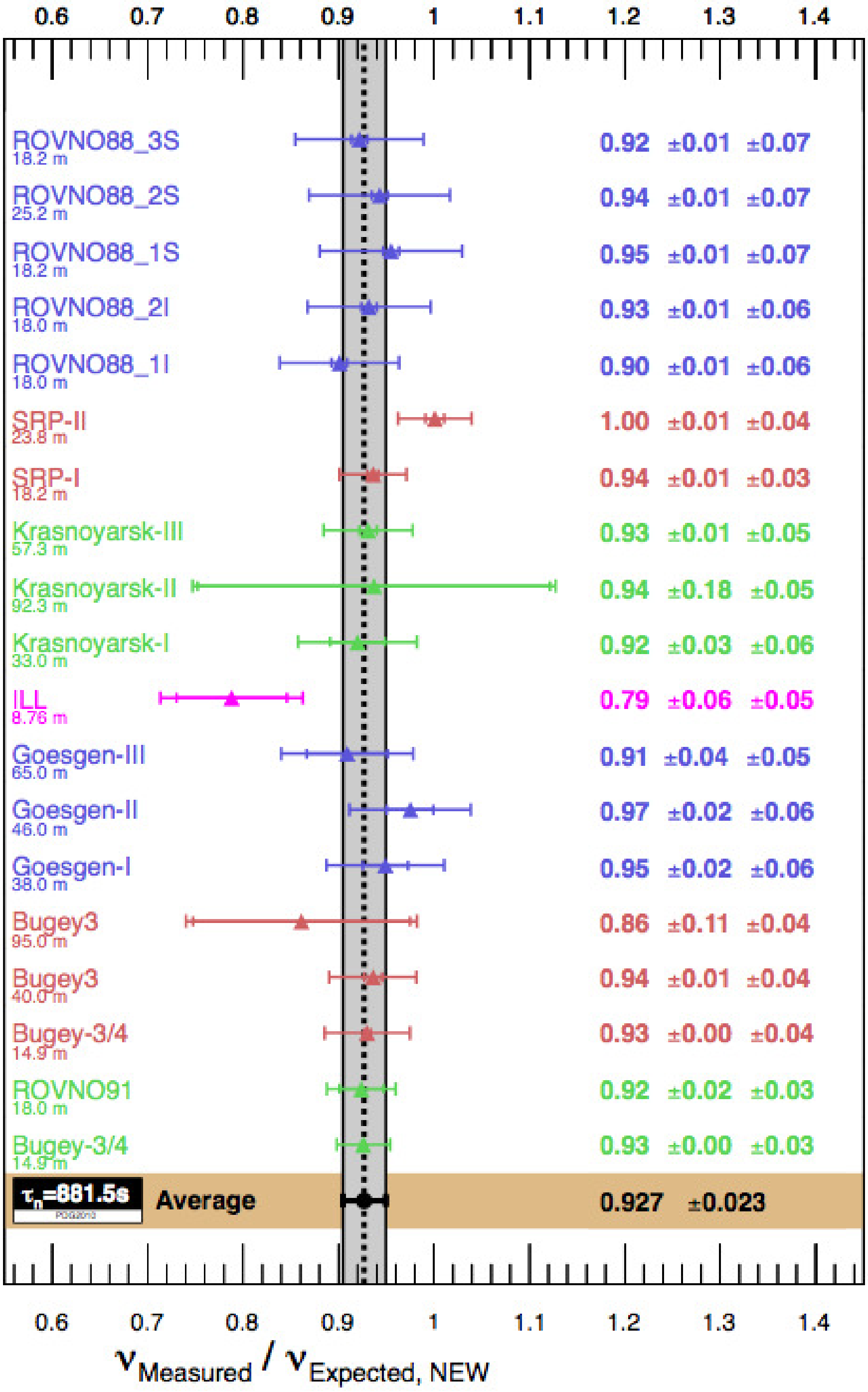

Figure 7.4: Ratio of observed rate over predicted rate for reactor neutrino experiments at a baseline < 100 m. The weighted average, comprehensive of systematics correlations, is also shown.

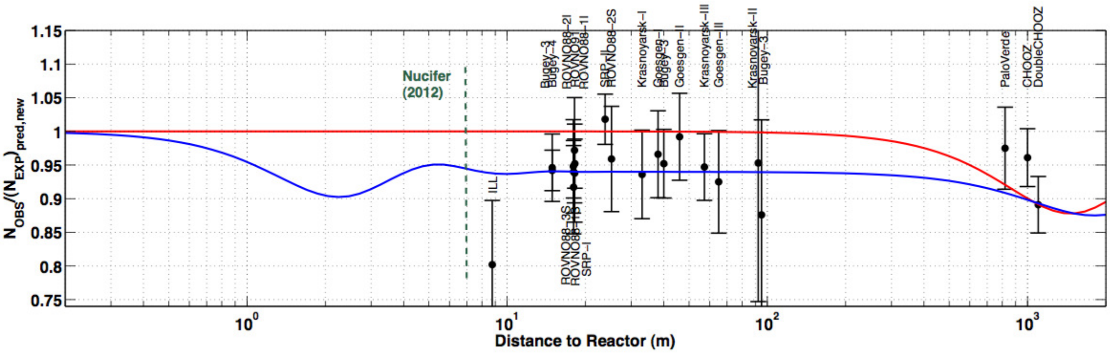

Figure 7.5: Ratio of observed over predicted rate for reactor experiments as a function of the L/E parameter. The red line represents the 3-flavors oscillation, while the blue line represents the oscillation pattern in a 4-flavor description.

number predicted according to the Bahcall ([52]) and Haxton ([53]) models for the detector cross sections. In both cases a deficit has been found, resulting in an average value of:

$$R_H^{Ga} = 0.76^{+0.09}_{0.08} \tag{7.2}$$

$$R_B^{Ga} = 0.86 \pm 0.05 \tag{7.3}$$

where R_H^{Ga} and R_B^{Ga} are the ratio of the observed interaction rate to the predicted rate by the Haxton and Bahcall models respectively.

As for the others above mentioned “anomalies”, also in this case the deficit may be explained as a short baseline oscillation, involving a forth neutrino family. Taking both the models into account, the results exclude the non-oscillation hypothesis at about 2.7σ of C.L. with a best fit for the oscillation parameters of $\Delta m^2 = 2.24 eV^2$ and $\sin^2 2\theta = 0.5$.

7.3 ICARUS T600 results on sterile searches

In the context of the searches for an additional sterile neutrino, with a mass squared of the order of ~ 1 eV, the ICARUS collaboration is about to publish a result on the ν_e appearance on the ν_μ CNGS neutrino beam. The results, presented in [54], are based on almost one half of the 2010-2011 exposure.

As the beam baseline is 730 km and the ν_μ energy spectrum is peaked in the range $10 \leq E_\nu \leq 30$ GeV, the L/E resulting parameter is much larger than the one reported by the above mentioned experiments. In this situation, an hypothetical $\nu_\mu \rightarrow \nu_e$ oscillation driven by the LSND parameters, could be described by $< P_{\nu_\mu \rightarrow \nu_e} >= 1/2 \sin^2(2\theta_{new})$ since the $1.27 \Delta m^2_{new} L/E$ would average to $\simeq 1/2$.

A total of 1091 neutrino events have been considered in this analysis, resulting from a total exposure of 3.3×10^{19} p.o.t., in a 6% agreement with the Montecarlo expectations. The selection criteria for ν_e CC detection, are based on four requirements:

(a) The neutrino vertex must fall inside a minimum fiducial volume, defined as a cut of 5 cm from each side of the active volume and 50 cm from its downstream wall;

(b) The total visible energy must be smaller than 30 GeV, to reduce the intrinsic ν_e beam induced background;

(c) One track, fully consistent with a m.i.p. for at least 8 consecutive wires, and subsequently building up into a shower, must be detected in the interaction vertex;

(d) All the other particles emitted in the interaction, with the exception of short proton like recoils, must be separated in al least one of the two transverse views (Induction2 and Collection).

To determine the efficiency of these cuts, a set of 171 $\nu_\mu \rightarrow \nu_e$ MC events have been analyzed, resulting 122 fulfilling (a) and (b), out of which 90 have been correctly identified as ν_e CC, resulting in an efficiency of $\eta = 0.74 \pm 0.05$. A similar analysis, made on MC neutral current events, reported no $\nu_\mu \rightarrow \nu_e$ events, setting an upper limit of 0.3 events for the analyzed data sample.

The expected signal coming from conventional sources, in the limits defined in (a) and (b), are as follows:

- 3.0 ± 0.2 events due to the intrinsic ν_e beam associated contamination
- 1.3 ± 0.3 ν_e events from θ_{13} oscillation
- 0.7 ± 0.05 ν_τ events, with $\tau \rightarrow e$

The total number of events expected, 5.0 ± 0.4, turns into an estimate of 3.7 ± 0.4 once the selection efficiency is applied. In the analyzed data sample, two events have been identified with the ν_e signature, to be compared with the 3.7 expectation.

The result reported is compatible with the absence of LSND anomaly, within the range observed. The exclusion area of the ICARUS experiment, shown in fig.7.6, strongly limits the window from the MiniBooNE experiment, still remaining compatible with a narrow region centered at $\Delta m^2 = 0.5 eV^2$ and $\sin^2(2\theta) = 0.005$ in which there is a 90% C.L. agreement with the LSND and MiniBooNE results and the limits form KARMEN and ICARUS.

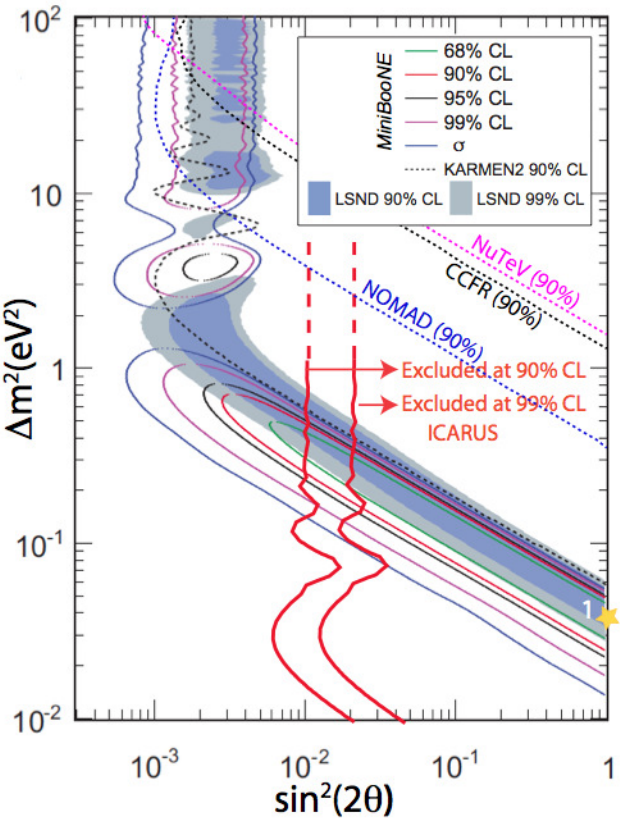

Figure 7.6: The exclusion area reported by ICARUS (red line) is compared with the results obtained by previous experiments.

7.4 The SPS proposal for sterile searches

In 2012 the ICARUS and NESSiE collaborations have proposed to the SPSC scientific committee an experiment which would definitely clarify the sterile neutrino accumulated anomalies, by either confirming or disproving once for all the presence of a fourth, sterile, neutrino family.

The proposed experiments, described in detail in [2] is based on two identical LAr-TPC detector, followed by a muon spectrometer, placed at “Near” and “Far” position, at a distance of 330 m and 1600 m respectively from the proton target, both exposed to a ν_μ ($\overline{\nu}_\mu$) neutrino beam form the SPS proton accelerator (fig.7.7).

Figure 7.7: Layout of the experiment proposed for the CERN SPS.

The energy and radial spectra of the ν_e and $\overline{\nu}_e$ are expected to be identical, except for second order effects, which can be reliably taken into account (fig. 7.8). In absence of any oscillation, the ν_e and $\overline{\nu}_e$ spectra measured at the two position must therefore be identical, since all cross sections and systematic biases related to the detecting technique cancel out. Any difference of the neutrino spectrum between the two positions would be attributed to the presence of an oscillation occurring between the two detector sites.

The core of the experiment is represented by the ICARUS T600 detector, whose characteristic and running performances has been described in the previous chapters, which will be placed in the “Far” position, and will be followed by a muon spectrometer, which will be placed downstream. A second LAr TPC (T150), identical to the T600 detector, except for the mass which will be ~ 150 t, will be placed in the “Near”

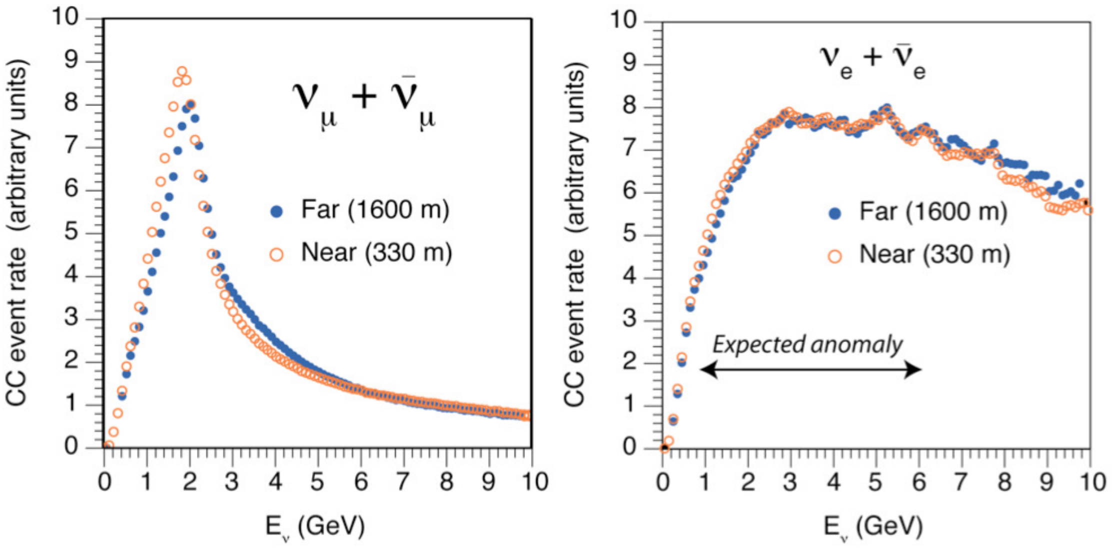

Figure 7.8: Event rates at near (red) and far (blue) position for muon (left) and electron (right) neutrino CC interactions in absence of sterile driven oscillaiton.

position, followed too by a muon spectrometer dedicated to the muon charge discrimination, in order to disentangle the $\overline{\nu}_\mu$ from ν_μ interactions.

The bubble chamber-like spatial resolution of the LAr detectors and their unique e^-/pi^0 separation, will permit to produce a clean, unbiased, sample of ν_e interactions at both sites. The muon spectrometers, on the other hand, will complete the physic potential of the experiment, by means of a precise measurement of the muon momentum from sub-GeV to several GeV, an its charge identification, leading to a precise measurement of the ν_μ CC spectra. The detection of NC interaction will finally provide a normalization sample at both sites, and will give an additional sterile neutrino oscillation signal through the measurement of NC/CC ratios.

The experiment plans to operate both with neutrino beam focussing, with an exposure of 4.5 10^{19} p.o.t., and in anti-neutrino focussing, with an exposure of 9.0 10^{19} p.o.t.. In both cases the analysis of the electron neutrino (and anti-neutrino) CC energy distribution will produce conclusive results both in the appearance and disappearance searches, thanks to the homogeneity of the ν_e ($\overline{\nu}_e$) neutrino spectra, for which a systematic error of 3% is expected.

For what concerns the appearance signal, the sensitivity foreseen for the new experiment with the above mentioned exposure in neutrino mode, will extend up to

$\sin^2 2\theta_{new} > 3\times10^{-4}$ (for $\Delta m^2 > 1eV^2$) and Δm^2 down to $0.01\ eV^2$ (for $\sin^2 2\theta_{new} = 1$) and will cover the whole the region allowed by LSND (fig. 7.9 left).

In the antineutrino mode, with a two year exposure, it would be possible to cover both the solution favored by MiniBooNE, and the whole LSND allowed region (fig. 7.9 right).

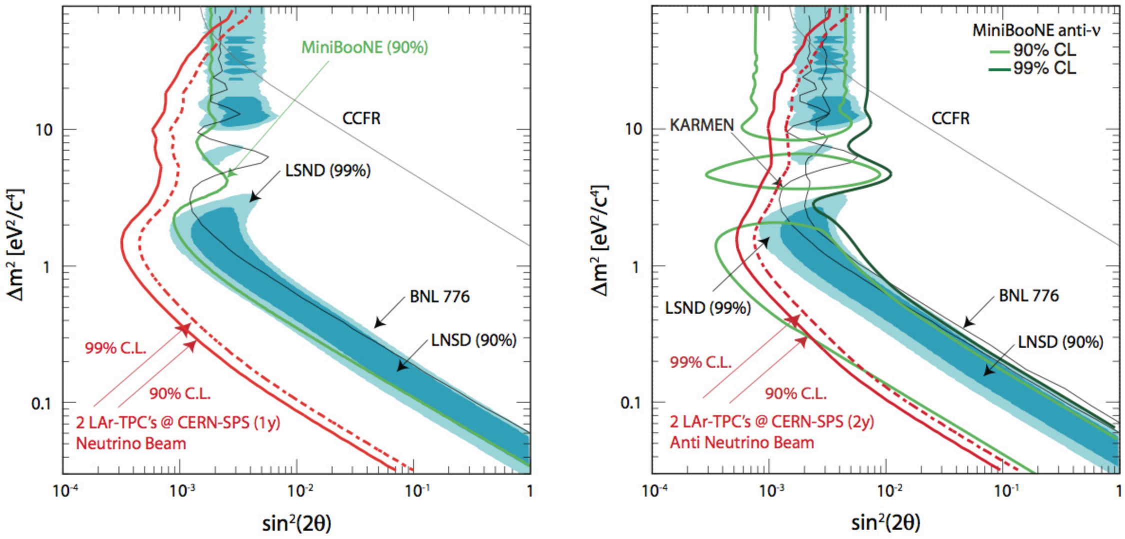

Figure 7.9: Sensitivities for one year of exposure on neutrino beam (left) and two years exposure on antineutrino beam (right) in the appearance searches. In both cases the whole LSND allowed region is completely covered.

The sensitivity for the ν_e disappearance signal for one year exposure to the ν_μ beam is enough to explore the whole region resulting from a combined analysis of the reactors and gallium anomalies (fig. 7.10).

It is worth noticing that the experiment would not only conclusively clarify the presence of any forth sterile neutrino, but in case of a positive result it will be able to measure the main mixing parameters related to the new neutrino family.

7.5 Electronic upgrade for the T150 detector

As shown in the previous chapters, the successful operation of ICARUS T-600 at the LNGS has proven the excellent functionality of the whole read-out chain. The front-end electronics have been performing within the specifications since the very beginning of the data taking, in May 2010, producing events with excellent signal to noise

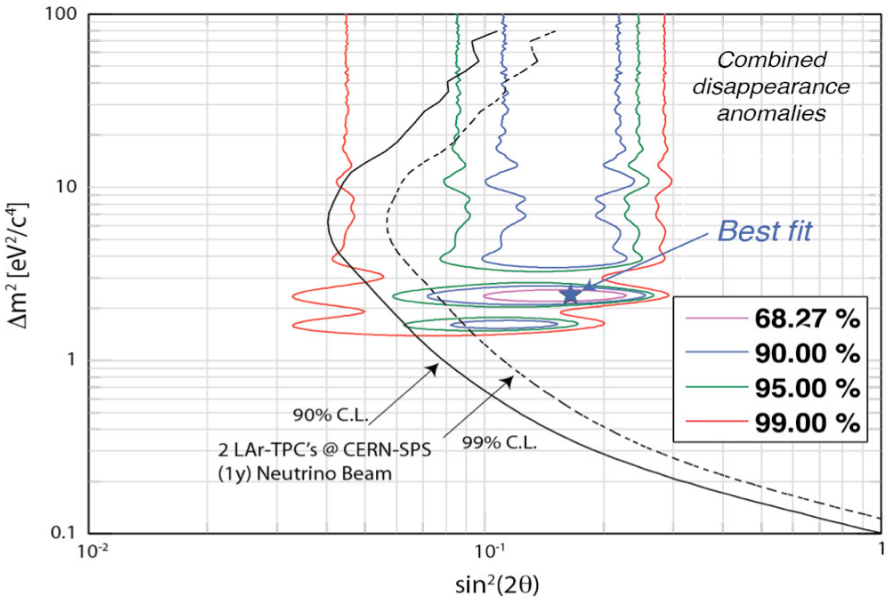

Figure 7.10: Sensitivities for one year of exposure on neutrino beam in disappearance mode, compared with the region emerging from a join analysis of reactors and gallium experiments.

ratio, where the topology of the tracks and the calorimetric measurement results can be precisely determined. The data acquisition has shown a good performance as well, with a detector live-time above 90% and with acquisition dead time reduced to few percent.

Even though the proposed architecture is well suited for other future Liquid Argon Time Projection Chambers (LAr-TPCs) the present read-out scheme could not be replied for the T150 detector at the SPS experiment, mainly because several electronics components have been dismissed. The need to upgrade the read-out gives a good chance to review the architecture, using up to date components and avoiding the main limitations arisen during the data taking.

The two main limitations addressed by the electronics R&D held at Padua University have been the reduction of the size occupied by the electronic racks and the implementation of a modern data link to the central DAQ system. The front-end amplifiers have been revisited as well, both in view of a smaller package implementation and of a better signal shaping.

7.5.1 New front-end implementation

The layout of the new front-end amplifiers for the T150 detector, depicted in fig.7.11, is composed by two stage. In the first stage a Radeka folded cascode is implemented using three JFET discrete transistors as an input stage. The advantage of this solution, similar to that adopted for the T600, is given by the low parallel noise ($\simeq 0.0001 pA/\sqrt{Hz}$) and the high transconductance ($\simeq 40mS$ for $I_d \simeq 10mA$) of the JFET stage which increases the signal to noise ratio.

The second stage is a zero-pole cancellation stage, needed to avoid the pile up of signals in case of consecutive hits. A fixed reference voltage can be connected to the positive input of the last amplifier (set at 2.5V in fig. 7.11) to give a fixed offset to the output signal, to better match the input range of the following ADC stage, for the different signal shapes of the Collection and Induction views.

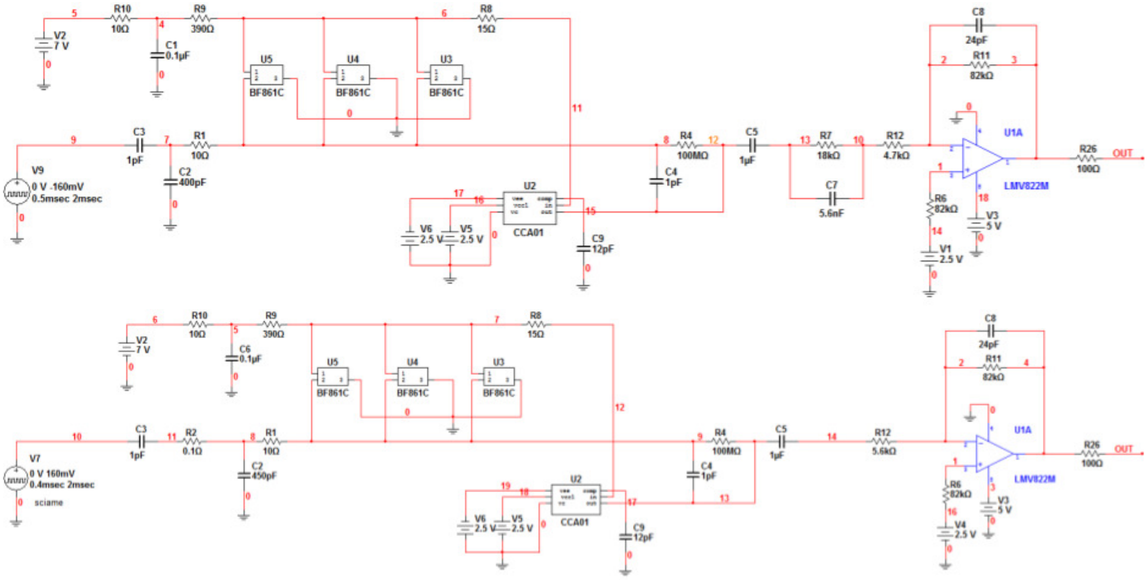

Figure 7.11: Schematics of the front-end amplifier in the two configuration tested.

Several tests of gain and noise level have been done, varying the feedback components and thus the shaping time, to check the effects of different signal shaping on amplifier performances in terms of S/N. For each set of parameters, the amplification has been measured as a function of the input voltage, to check the linearity. An additional capacitance has been included in parallel to the input stage to simulate the effect of the detector capacitance. To better understand the effects of the detector capacitance, a set of values ranging from 50 to 450 pF has been tested.

The results of these test are given for the two sets of parameters reported in in fig. 7.11 and are compared to the noise condition for the different values of the input capacitance. In fig. 7.12 it is possible to appreciate the linearity of the amplifier from ∼ 100 mV to ∼ 2.5 V of output voltage.

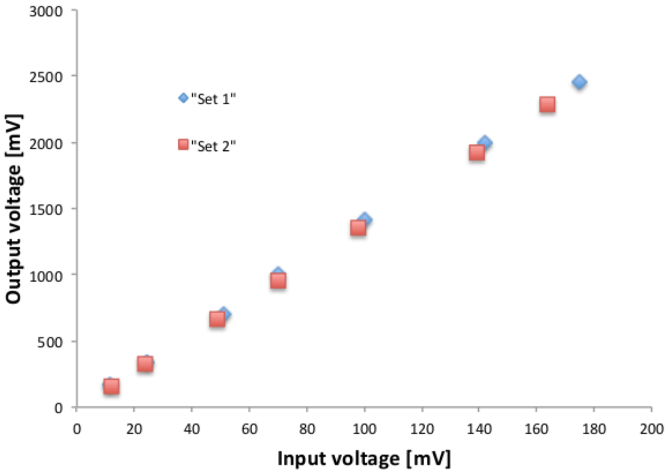

Figure 7.12: Response of the front end-amplifier. The linearity is well controlled over the whole voltage range.

To study the dependence of the amplification from the input capacitance, a step function has been input to the amplifier and a linear fit has been applied to the output signal. The noise level has been measured with a HP 3400 B RMS-voltmeter. The results for the two sets, fig.7.13, shows how the gain is unchanged, while the noise degrades on the second set.

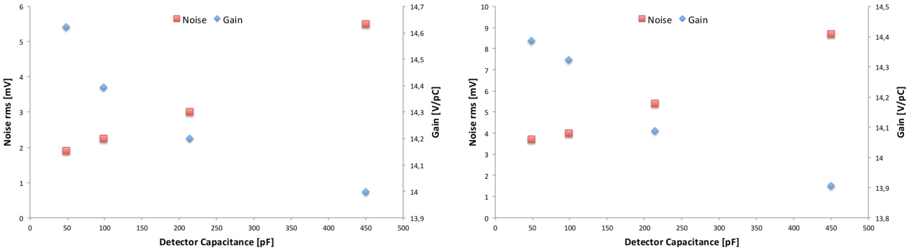

Figure 7.13: Gain and noise trend for the first (left) and second (right) set of parameters.

7.5.2 Compact electronics housing

To reduce the space needed for hosting the front-end and read out electronics, which in the present detector occupies a whole rack for each set of 576 channels, a new compact housing has been designed and prototyped. The new system, depicted in fig.7.14, exploits the UHV flange already in use in the T600 detector, both as a feed-through for the wires signals and as a backplane for the acquisition boards, which are housed in a compact box of ~ 12 liters of volume. A common rail is used to distribute the power supply needed for the electronics, while the wire biasing is provided through a set of connectors placed on the flange.

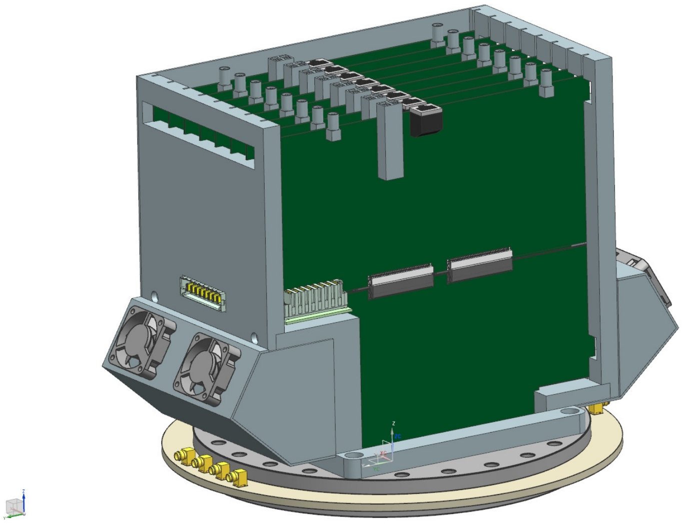

Figure 7.14: Drawing of a vertical section of the new read-out crate.

The read out boards will be divided in two sub-boards, the first performing signal amplification, while the second digitalizing the signals and handling the trigger and the data stream to the DAQ. Each board is inserted into two connector placed on the flange, carrying each 32 signals, resulting in 64 channel per read-out board. In a single flange up to 8 boards can be housed, for a total of 512 channels per crate.

One of the main issue to be addressed when reducing the size of the electronic housing, is the estimate of power consumption of the whole system, which produces an important source of heat inside the housing box. A sufficient air-flow circulation has to be foreseen to keep the operating temperature low and to prevent any damage to the electronic components.

Vin [V]	Current per board [A]	Power pr board [W]	Power per crate [W]
9	1.7	15.03	120.24
3.3	1	3.3	26.4
-9	0.1	0.45	3.6

Table 7.1: Values of power consumption used as a reference for the dissipation analysis. In this configuration all the voltage needed for the analog and digital components are derived from the three main power supply rails.

The whole consumption has been estimate by analyzing the current drain for each power supply line, for both the digital and the analog boards, and is reported in tab.7.1. The overall power consumption in this configuration is 150W, but two more reference values (100W and 210W) have been also considered, to study the possible impact on the heat flow of a modification of the analog layout.

To reproduce the heat distribution of the read-out board, a set of 10 resistor of 10Ω have been distributed over a custom breadboard, connected in a way to produce an $R_{eq} = 4\Omega$. To monitor the temperature of each board a LM35 temperature sensor has been mounted in the middle of each board, while for the central board two more sensors have been put on the corner, to monitor the temperature homogeneity.

Three sets of measurement have been done, with different layout of the housing box. For the first measurement, four fans (Sunon KDE1204PKVX) have been directly mounted on the top of four dedicated holes placed on the two opposite side of the box. This setup has shown a strong inhomogeneity on the temperature of the different boards, as they were not exposed to the same air-flow (fig.7.16, 1 Setup). To prevent this situation, two carters have been included in the design, for distributing the air-flow homogeneously over all the boards. The 4 round holes dedicated to the fans have been replaced with a rectangular opening along all the lateral side of the box (fig.7.15).

This setup has reduced the temperature difference between boards, but the higher values remains close to the maximum temperature allowed (fig.7.16, 2 Setup). To increase the cooling, a new set of fans (Sunon PSD1204PQBX-A), with an air-flow more than doubled, has been tested. An advantage given by the use of this new fan models is the possibility to modulate the air-flow acting on the power supply, which can range from $\sim$ 4V to 12V. The tests made with a relative low value of power supply voltage, 5V, has show a reduction of the temperature below the limit value, with

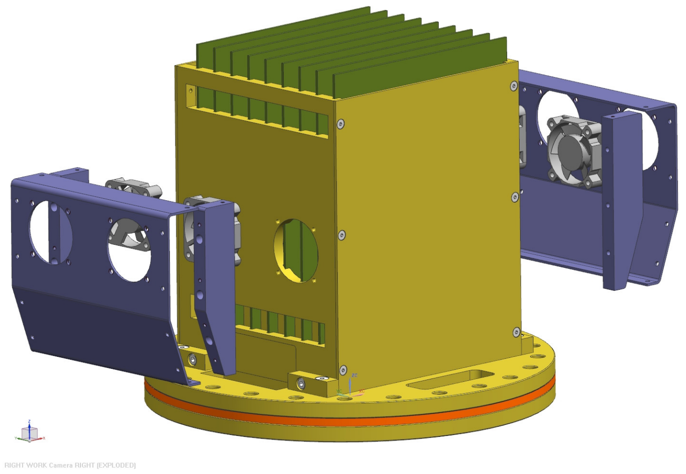

Figure 7.15: Drawing of the housing box used for dissipation measurement, with and without carters.

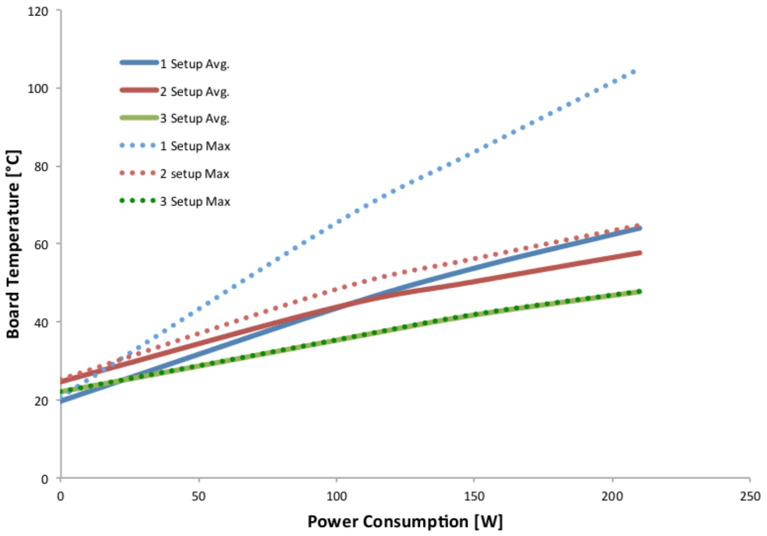

Figure 7.16: Trend of the average (solid) and maximum (dotted) temperature recorded during the three test with different setup.

an increase of the homogeneity of the boards temperature(fig.7.16, 3 Setup). The possibility to increase the air-flow, further reducing the boards temperature, makes this setup safe to use in warm environment, and easy to control by simple electronic devices.

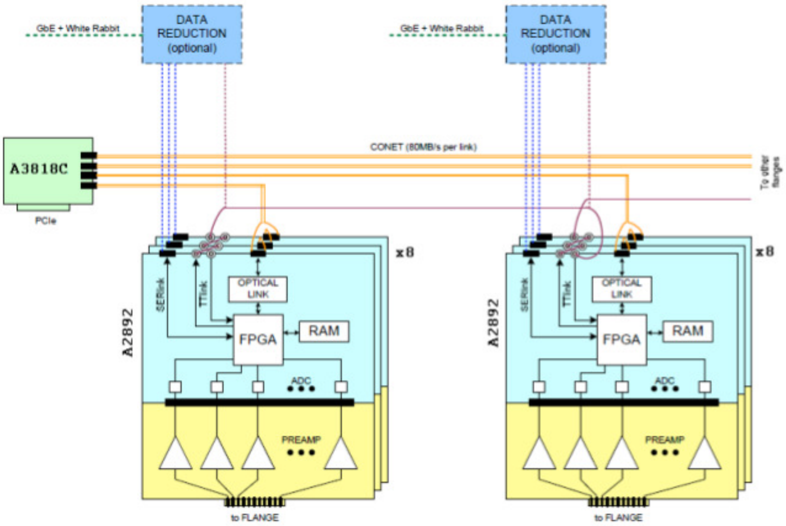

Figure 7.17: Block diagram of the proposed architecture, exemplified for two read-out crates. Both the CONET2 and the Ethernet read-out schemes are shown.

7.5.3 Read-out architecture architectures for the new system

After the amplification, occurring in the first sub board, the signals are digitized by 64 serial 12 bit ADC sampling at 2.5MS/s, which are read and controlled by a unique FPGA placed on the second sub-board. A bank of external RAM is also foreseen in order to implement a MEB logic, similar to that used for the T600 detector. Beside reading the 64 inputs, the FPGA will provide a x4 data compression, with the same algorithm that has been widely proved during the current T600 data taking, and will handle external control signals, such as reset, global clock and trigger. Finally high speed serial I/O, such as the Rocket I/O feature of the modern FPGA families, will provide a ∼Gb/s data communication to the DAQ (fig.7.17).

The data communication structure that will replace the VME standard, which has shown a strong limitation on the data transfer, must provide a bandwidth adequate to register a full drift, non compressed event at every spill extraction ($\sim 100MB/s$). Two architecture have been considered, the use of the CONET2 link, patented by CAEN, and the use of a standard Fast Ethernet link from each read-out board.

The CONET2 link is a commercial solution developed by CAEN, which provides a 100MB/s serial read-out over a optical transmission line that can be daisy chained over 8 end-point. A A3818C 4x CONET2 to PCIe bridge is foreseen for each set of four read out crate, to control the transmission lines. A second daisy chained electric signal (TT-Link) is used to distribute a common sampling clock for all the ADCs, as well as other common signals such as trigger, reset, start/stop acquisition etc.

As an alternative solution to the CONET2 link, also a Fast Ethernet connection has been considered as a suitable option for the read-out architecture. The main advantage of this architecture is given by the use of a switched I/O, which avoids the problematic related to the daisy chain architecture. A second advantage is the possibility to transmit both the data and the control signals over the same cable, thanks to the implementation of the packet priority defined in the Ethernet standard. All the packets that are time critical, such as those for synchronization, trigger and the packets which alerts for a forthcoming extraction, may be privileged over the packets used for data transfer and control. Moreover, the White Rabbit synchronization protocol [ref], successfully operated during the 2012 time of flight measurement[ref], may provide a $\sim$ns time synchronization to all the end-points over the Ethernet connection, with a minimum payload on the data communication. This perspective results very appealing since it would provide time synchronization, trigger, and data transfer over the same standard Ethernet line, reducing the complexity of the whole architecture.

A prototypal system is under production in collaboration with CAEN, foreseeing a first test of the whole new architecture in the next future. For the read-out it has been decided to leave all the options available, integrating all the I/O needed both for CONET2 and Fast Ethernet connection. The possibility of switching between the two architecture is given by the fact that a single FPGA will host the whole code needed for communication, thus permitting to study the performances of both the setups with a firmware update.

Chapter 8

Conclusion

The successful operation of the T600 detector at the LNGS represents a milestone in the development of the LAr TPC technology. The steady running condition proved during the 2010-2013 data taking have shown that the technology is mature, and is ready to be up-scaled to higher masses. In determining the feature of this new detector a critical aspect is related to the development of a high efficiency trigger for interesting events, as well as its qualification. For the 2010-2012 CNGS run a flexible trigger setup, which handled all the trigger information available have been developed, qualified and put in production.

The trigger main setup, which exploits the PMT signals as well as the time synchronization with the SPS proton extraction, have been running in its definitive configuration since few months from the first event acquired by the T-600 detector. To check its efficiency, an independent minimum bias trigger has been developed on the basis of the charge signal recorded by the TPC wires, which has proven an almost full efficiency on the Montecarlo simulated events. This second trigger has been introduced in parallel to the main PMT trigger during the 2011 run. A set of 1.7×10^{19} proton on target (p.o.t.) has been completely analyzed, showing a full efficiency of the PMT setup on neutrino interaction, and an efficiency exceeding 99% on muons from external neutrino interactions.

In 2012 the same filtering algorithm used for the 2011 backup trigger has been implemented in a hardware device, which has been installed in all the read-out boards of the detector. This additional trigger has been running in a first phase only for CNGS events, while after few months of commissioning it has been enabled to trigger also atmospheric and non-beam related events. The analysis of the CNGS data sample, based on a statistics of 1.4×10^{19} p.o.t. has confirmed the result reported in 2011 on the full PMT efficiency for CNGS neutrino interactions.First results on the atmospheric data taking have instead shown a consistent recovery of the PMT trigger inefficiency in the sub-GeV events. This energy region is of particular interest in view of nucleon decay searches, which are a fundamental part of the T-600 physics program. The additional trigger greatly enhances the T-600 sensitivity to nucleon decay, opening the way for a improvement of the currently reported limits for two decay channels.

The time synchronization with the SPS proton extraction, which has been firstly developed for triggering purpose, has been the starting point for two separate high precision measurement of the neutrino time of flight on the CNGS beam. The results obtained by ICARUS, which have been triggered by the claim reported by the OPERA collaboration about a superluminar neutrino speed, are fully consistent with the speed of light, within the experimental uncertainties.

Finally the electronic setup has been completely revisited in view of a future short baseline experiment to be held at CERN on a new neutrino beam-line from the SPS proton accelerator, to clarify the present anomalies hinting at the presence of an additional sterile neutrino. The LAr-TPC technique is well suited for this search, thanks to its calorimetric and topological reconstruction capability. In the context of the R&D activity held at Padua University, three housing crates have been prototyped, while the architecture of the new digital read-out boards is about to be defined.

Ringraziamenti

Alla fine di questi tre anni di dottorato sono molte le persone che mi sento di dover ringraziare, per il contributo che hanno dato alla mia crescita sia sul piano professionale che personale. Il primo ringraziamento lo vorrei fare al Prof. Sandro Centro, che mi ha seguito in tutti questi anni di ricerca dandomi sempre ottimi consigli. Ringrazio inoltre il Dott. Alberto Guglielmi, il Prof. Daniele Gibin e il Dott. Francesco Pietropaolo, i quali mi hanno dato un inestimabile aiuto, in particolar modo durante la stesura di questa tesi. Ringrazio la Dott.ssa Meng per la sua costante disponibilità e il Dott. Sandro Ventura per tutto ciò che da lui ho imparato. Ringrazio inoltre il Dott. Baibussinov e Daniele Filippi, per il supporto datomi. Un ringraziamento sentito a tutta l'officina elettronica, in modo particolare a Marino Nicoletto. Un caloroso ringraziamento a tutti i giovani del gruppo padovano di Icarus: Pippo, Angela e Christian. Un ringraziamento non può mancare anche ad Antonio, Sabine e Rosanna, per aver reso la paura tè un momento così piacevole.

Molte altre persone mi sono state vicine in questi anni, dandomi il loro sostegno e la loro amicizia, non me ne vorranno se non riuscirò ad elencare tutti i loro nomi. Senza dubbio ringrazio di cuore la mia famiglia, ed in particolare i miei genitori e mia sorella, la loro vicinanza è sempre stata un valido sostegno nell'affrontare le difficoltà. Ringrazio Anna, per avermi supportato (e sopportato), in particolare durante l'intenso periodo di scrittura tesi. Tra i molti amici che vorrei ringraziare non possono mancare Giovanni, Stefano (le cui scelte di software specializzato sono state cruciali per il conseguimento del mio dottorato), Francesca, Gabriele, Enrico (in particolare per le sue attività di PR), Fabrizio, Serenella e Alessandra. Infine, ma non per importanza, ringrazio di cuore Elide a cui penso con grande affetto.

Bibliografia

[1] Rubbia, C. *The liquid-argon time projection chamber: a new concept for neutrino detectors*. Tech. Rep. CERN-EP-INT-77-8, CERN, Geneva (1977).

[2] Antonello, A. et al. *Search for anomalies in the neutrino sector with muon spectrometers and large lartpc imaging detectors at cern* (2012). arXiv/1208.0862. arXiv/1208.0862.

[3] Baibussinov, B. et al. *A New, very massive modular Liquid Argon Imaging Chamber to detect low energy off-axis neutrinos from the CNGS beam: Project MODULAr*. *Astropart.Phys.*, **29**:174–187 (2008). 0704.1422. 0704.1422, doi:10.1016/j.astropartphys.2008.01.001.

[4] Bueno, A. et al. *Nucleon decay searches with large liquid argon TPC detectors at shallow depths: Atmospheric neutrinos and cosmogenic backgrounds*. *JHEP*, **0704**:041 (2007). hep-ph/0701101. hep-ph/0701101, doi:10.1088/1126-6708/2007/04/041.

[5] Pauli, W. *Dear radioactive ladies and gentlemen*. *Phys.Today*, **31N9**:27 (1978).

[6] Lobashev, V. *The search for the neutrino mass by direct method in the tritium beta-decay and perspectives of study it in the project katrin*. *Nuclear Physics A*, **719**, 0:C153 – C160 (2003). URL: http://www.sciencedirect.com/science/article/pii/S0375947403009850, doi:10.1016/S0375-9474(03)00985-0.

[7] Reines, F. and Cowan, C.L. *Detection of the free neutrino*. *Phys. Rev.*, **92**:830–831 (1953). URL: http://link.aps.org/doi/10.1103/PhysRev.92.830, doi:10.1103/PhysRev.92.830.

[8] Ahmad, Q.R. et al. *Direct evidence for neutrino flavor transformation from neutral-current interactions in the sudbury neutrino observatory*. *Phys. Rev. Lett.*,

89:011301 (2002). URL: http://link.aps.org/doi/10.1103/PhysRevLett.89.011301, doi:10.1103/PhysRevLett.89.011301.

[9] Wendell, R. et al. *Atmospheric neutrino oscillation analysis with subleading effects in super-kamiokande i, ii, and iii*. *Phys. Rev. D*, **81**:092004 (2010). URL: http://link.aps.org/doi/10.1103/PhysRevD.81.092004, doi:10.1103/PhysRevD.81.092004.

[10] Ospanov, R. *A measurement of muon neutrino disappearance with the MINOS detectors and NuMI beam* (2008).

[11] Adamson, P. et al. *Improved measurement of muon antineutrino disappearance in minos*. *Phys. Rev. Lett.*, **108**:191801 (2012). URL: http://link.aps.org/doi/10.1103/PhysRevLett.108.191801, doi:10.1103/PhysRevLett.108.191801.

[12] Schwetz, T., Tortola, M. and Valle, J. *Global neutrino data and recent reactor fluxes: status of three-flavour oscillation parameters*. *New J.Phys.*, **13**:063004 (2011). 1103.0734. 1103.0734, doi:10.1088/1367-2630/13/6/063004.

[13] Abe, K. et al. *Indication of Electron Neutrino Appearance from an Accelerator-produced Off-axis Muon Neutrino Beam*. *Phys.Rev.Lett.*, **107**:041801 (2011). 1106.2822. 1106.2822, doi:10.1103/PhysRevLett.107.041801.

[14] An, F. et al. *Observation of electron-antineutrino disappearance at Daya Bay*. *Phys.Rev.Lett.*, **108**:171803 (2012). 1203.1669. 1203.1669, doi:10.1103/PhysRevLett.108.171803.

[15] Ahn, J. et al. *Observation of Reactor Electron Antineutrino Disappearance in the RENO Experiment*. *Phys.Rev.Lett.*, **108**:191802 (2012). 1204.0626. 1204.0626, doi:10.1103/PhysRevLett.108.191802.

[16] Fogli, G.L. et al. *Global analysis of neutrino masses, mixings, and phases: Entering the era of leptonic cp violation searches*. *Phys. Rev. D*, **86**:013012 (2012). URL: http://link.aps.org/doi/10.1103/PhysRevD.86.013012, doi:10.1103/PhysRevD.86.013012.

[17] Abe, K. et al. *A Measurement of the Appearance of Atmospheric Tau Neutrinos by Super-Kamiokande* (2012). 1206.0328. 1206.0328.

[18] Y. Ge, P. Sala, A.R. *e/π^0 separation in icarus liquid argon tpc* (2005). ICARUS-TM/03-05.

[19] Nishino, H. et al. *Search for proton decay via $p \rightarrow e^+\pi^0$ and $p \rightarrow \mu^+\pi^0$ in a large water cherenkov detector*. *Phys. Rev. Lett.*, **102**:141801 (2009). URL: http://link.aps.org/doi/10.1103/PhysRevLett.102.141801, doi:10.1103/PhysRevLett.102.141801.

[20] Kobayashi, K. et al. *Search for nucleon decay via modes favored by supersymmetric grand unification models in super-kamiokande-i*. *Phys. Rev. D*, **72**:052007 (2005). URL: http://link.aps.org/doi/10.1103/PhysRevD.72.052007, doi:10.1103/PhysRevD.72.052007.

[21] Regis, C. et al. *Search for proton decay via $p \rightarrow \mu^+K^0$ in super-kamiokande i, ii, and iii*. *Phys. Rev. D*, **86**:012006 (2012). URL: http://link.aps.org/doi/10.1103/PhysRevD.86.012006, doi:10.1103/PhysRevD.86.012006.

[22] et al., A.B. *nucleon decay searches: study of nuclear effects and background* (2004). ICARUS-TM/01-04,.

[23] Nakamura, K. and Group, P.D. *Review of particle physics*. *Journal of Physics G: Nuclear and Particle Physics*, **37**, 7A:075021 (2010). URL: http://stacks.iop.org/0954-3899/37/i=7A/a=075021.

[24] Peres, O. and Smirnov, A.Y. *Atmospheric neutrinos: LMA oscillations, U(e3) induced interference and CP violation*. *Nucl.Phys.*, **B680**:479–509 (2004). hep-ph/0309312. hep-ph/0309312, doi:10.1016/j.nuclphysb.2003.12.017.

[25] G. Battistoni, e.a. *the icarus detector at the gran sasso: an upgraded analysis* (2005). ICARUS-TM/05-05.

[26] Hirata, K. et al. *Observation in the Kamiokande-II Detector of the Neutrino Burst from Supernova SN 1987a*. *Phys.Rev.*, **D38**:448–458 (1988). doi:10.1103/PhysRevD.38.448.

[27] Bionta, R.M. et al. *Observation of a neutrino burst in coincidence with supernova 1987a in the large magellanic cloud*. *Phys. Rev. Lett.*,

58:1494–1496 (1987). URL: http://link.aps.org/doi/10.1103/PhysRevLett.58.1494, doi:10.1103/PhysRevLett.58.1494.

[28] Amerio, S. et al. *Design, construction and tests of the icarus t600 detector*. *Nuclear Instruments and Methods in Physics Research Section A: Accelerators, Spectrometers, Detectors and Associated Equipment*, **527**, 3:329 – 410 (2004). URL: http://www.sciencedirect.com/science/article/pii/S0168900204004966, doi:10.1016/j.nima.2004.02.044.

[29] Doke, T. *A Historical view on the R&D for liquid rare gas detectors*. *Nucl.Instrum.Meth.*, **A327**:113–118 (1993). doi:10.1016/0168-9002(93)91423-K.

[30] et al., M.A. *measurement of the optical fiber transit time for the icarus experiment* (2012). ICARUS-TM/12-01.

[31] D. Gibin, e.a. *a study of wire signal discrimination* (2004). ICARUS-TM/04-10.

[32] et al., D.G. *an improved study of wire signal discrimination* (2005). ICARUS-TM/05-04.

[33] URL: http://www.fluka.org/.

[34] Baibussinov, B. et al. *A hardware implementation of region-of-interest selection in lar-tpc for data reduction and triggering*. *Journal of Instrumentation*, **5**, 12:P12006 (2010). URL: http://stacks.iop.org/1748-0221/5/i=12/a=P12006.

[35] Baibussinov, B. et al. *Free electron lifetime achievements in liquid argon imaging tpc*. *Journal of Instrumentation*, **5**, 03:P03005 (2010). URL: http://stacks.iop.org/1748-0221/5/i=03/a=P03005.

[36] T. Adam et al., arXiv:1109.4897v4.

[37] A.G. Cohen, and S.L. Glashow, Phys. Rev. Lett., 107, 181803 (2011).

[38] M. Antonello et al., Phys. Lett B 711 (2012) 270.

[39] M. Antonello et al., Phys. Lett. B 713 (2012) 17.

[40] S. Bertolucci, Talk given at the NEUTRINO2012 Conference, Kyoto, Japan (3-9 June 2012) .

[41] M. Antonello et al., JHEP11 (2012) 049.

[42] P. Alvarez Sanchez et al., Measurement of CNGS muon neutrino speed with Borexino, ArXiV:1207.6860;

[43] N.Y. Agafonova et al., Measurement of the velocity of neutrinos from the CNGS beam with the Large Volume Detector, ArXiV:1208.1392.

[44] M Lipinski et al, Performance results of the first White Rabbit installation for CNGS time transfer, private communication, submitted to IEEE Transactions (2012).

[45] B. Caccianiga et al, GPS-based CERN-LNGS time link for Borexino, arXiv:1207.0591v2, and references therein.

[46] R. Acciarri et al., Journal of Phys. Conf. Series 308 (2011) 012005, and references therein.

[47] Athanassopoulos, C. et al. *Candidate events in a search for* $\overline{\nu}_\mu \rightarrow \overline{\nu}_e$ *oscillations*. *Phys. Rev. Lett.*, **75**:2650–2653 (1995). URL: http://link.aps.org/doi/10.1103/PhysRevLett.75.2650, doi:10.1103/PhysRevLett.75.2650.

[48] Beringer, J. et al. *Review of particle physics*. *Phys. Rev. D*, **86**:010001 (2012). URL: http://link.aps.org/doi/10.1103/PhysRevD.86.010001, doi:10.1103/PhysRevD.86.010001.

[49] Aguilar-Arevalo, A. et al. *A Combined* $\nu_\mu \rightarrow \nu_e$ *and* $\bar{\nu}_\mu \rightarrow \bar{\nu}_e$ *Oscillation Analysis of the MiniBooNE Excesses* (2012). 1207.4809. 1207.4809.

[50] Mueller, T.A. et al. *Improved predictions of reactor antineutrino spectra*. *Phys. Rev. C*, **83**:054615 (2011). URL: http://link.aps.org/doi/10.1103/PhysRevC.83.054615, doi:10.1103/PhysRevC.83.054615.

[51] Mention, G. et al. *Reactor antineutrino anomaly*. *Phys. Rev. D*, **83**:073006 (2011). URL: http://link.aps.org/doi/10.1103/PhysRevD.83.073006, doi:10.1103/PhysRevD.83.073006.

[52] Bahcall, J.N. *Gallium solar neutrino experiments: Absorption cross sections, neutrino spectra, and predicted event rates*. *Phys. Rev. C*,

56:3391–3409 (1997). URL: http://link.aps.org/doi/10.1103/PhysRevC.56.3391, doi:10.1103/PhysRevC.56.3391.

[53] Haxton, W. *Cross section uncertainties in the gallium neutrino source experiments*. *Physics Letters B*, **431**, 1,Äì2:110 – 118 (1998). URL: http://www.sciencedirect.com/science/article/pii/S0370269398005814, doi:10.1016/S0370-2693(98)00581-4.

[54] A. Donini, M. Maltoni, D. Meloni, P. Migliozzi and F. Terranova, JHEP **0712**, 013 (2007) [arXiv:0704.0388 [hep-ph]].